3-24-2016

Utilization of a Geodesic Sphere and Quadcopter as Two-Way Field Probe for Electro-Magnetic Field Measurements in an Indoor Radar Cross Section Range

Nathan Lett

UTILIZATION OF A GEODESIC SPHERE AND QUADCOPTER AS TWO-WAY FIELD PROBE FOR ELECTRO-MAGNETIC FIELD MEASUREMENTS IN AN INDOOR RADAR CROSS SECTION RANGE

THESIS

Nathan T. Lett, Capt, USAF

AFIT-ENG-MS-16-M-031

DEPARTMENT OF THE AIR FORCE
AIR UNIVERSITY

AIR FORCE INSTITUTE OF TECHNOLOGY

Wright-Patterson Air Force Base, Ohio

AFIT-ENG-MS-16-M-031

UTILIZATION OF A GEODESIC SPHERE AND QUADCOPTER AS TWO-WAY FIELD PROBE FOR ELECTRO-MAGNETIC FIELD MEASUREMENTS IN AN INDOOR RADAR CROSS SECTION RANGE

THESIS

Presented to the Faculty

Department of Electrical and Computer Engineering

Graduate School of Engineering and Management

Air Force Institute of Technology

Air University

Air Education and Training Command

in Partial Fulfillment of the Requirements for the

Degree of Master of Science in Electrical Engineering

Nathan T. Lett, B.S.E.E

Capt, USAF

24 March, 2016

AFIT-ENG-MS-16-M-031

UTILIZATION OF A GEODESIC SPHERE AND QUADCOPTER AS TWO-WAY FIELD PROBE FOR ELECTRO-MAGNETIC FIELD MEASUREMENTS IN AN INDOOR RADAR CROSS SECTION RANGE

THESIS

Nathan T. Lett, B.S.E.E
Capt, USAF

Committee Membership:

Dr. P. Collins
Chair

Maj Brian Woolley, PhD
Member

Dr. A. Terzuoli
Member

Abstract

Radar Cross Section (RCS) measurements rely heavily on multiple assumptions. Uncertainty in the final measurement is determined based on these assumptions. One source in particular is the non-homogeneous nature of the transmission path between radar test equipment and a target under test. The following research extends prior research. This thesis intends to provide a unique two-way field probe solution for measuring Electro-magnetic (EM) fluctuations in a test volume.

In this thesis, the design, development, and demonstration of a geodesic sphere encased quadcopter two-way probe is explained. The Parrot® Bebop Drone quadcopter was used with a 2ν frequency divided geodesic sphere design. Position and pose data was accomplished with a Vicon™ motion capture system. And a Lintek 4000 radar instrumentation system provided RCS measurements.

Many major system design considerations were discovered. The geodesic sphere to quadcopter interface should not interfere with flight characteristics. RCS measurements with position and pose data synchronization is important. And the sample points captured must be sufficient to extract any conclusions.

This research concluded that a geodesic sphere and quadcopter could be used as a two-way probe to measure general field characteristics of an indoor compact RCS range. In a quadcopter only flight test, using a 2 to 5 GHz frequency sweep at 0.1 GHz increments, there were three instances where a direct correlation in phase measurement to flight path was observed. Further research is required to better understand the quality of the field measurements.

Acknowledgements

I would most like to thank God for giving me the endurance required by this thesis, the humility to realize when I was going too far down the wrong rabbit hole, and the immense support of my family.

To my wife, and daughter; thank you for giving me the time and space to do my work. But most of all, thank you for reminding me to take breaks and reboot. I could not have done this without you.

Dr. Collins, thank you for giving me the tool set for this research effort. Also, thank you for showing me where I went wrong, when I was on the right track, and the trust that I would get it to work. Most of all, thank you for building the cage, I have no idea when I would have done it.

Captain Dossett, thank you for the ideas, the constructive criticism, the new hobby, and yes, for showing me the Bebop ROS package.

Nathan T. Lett

Contents

Page

List of Figures

List of Tables

UTILIZATION OF A GEODESIC SPHERE AND QUADCOPTER AS TWO-WAY FIELD PROBE FOR ELECTRO-MAGNETIC FIELD MEASUREMENTS IN AN INDOOR RADAR CROSS SECTION RANGE

I. Introduction

To accurately measure the RCS of an object with zero uncertainty, a uniform plane wave is mathematically required to perfectly illuminate the test article within the test volume or "quiet zone." This requirement assumes an infinite distance between the instrumentation radar and target of interest as well as a perfectly stable medium through which the EM waves can travel [1]. Neither of these assumptions is practicable. Until physicists can find a way to measure from an infinite distance, the only area of improvement is to understand the medium's instabilities.

EM fields within the test volume can be measured and categorized utilizing EM field probe antennas. The measurements can be used to find amplitude distortions and phase deviations as the antenna probe moves through the test volume along some arbitrary path.

There are two primary methods of probing the EM field [2]. A one-way probe (receiving antenna) directly measures the incident field. The two-way probe (reflector with known RCS) reflects the incident wave back to a receiving antenna (usually the same as the transmitting antenna). The recorded measurement indicates the apparent field at the location in space occupied by the two-way probe. Scattering of the apparent field by the two-way probe is proportional to deviations from an ideal plane wave in the incident field. One-way field probes antenna are not ideal

due to their size, interference induced by support structures and electrical connections, and limitations in movement [3].

1.1 Background

When placed in the path of a radar beam, an object will scatter the incident EM energy in all directions. The energy reflected back to the source radar is known as the object's RCS. The RCS of an object is a theoretical area describing the effective electric cross sectional area an object has that will reflect EM waves back to originating radar system [1]. This scattering dispersion is dependent on object size, shape, and material composition as well as the direction of the EM waves angle of incidence to the object [2].

In order to accurately measure the RCS of an object as an estimation in the far-field, the EM waves need to be evenly distributed in magnitude and planer in phase within the test volume, illustrated in Figure 1b provided by Knott‘ [1]. However, the wave propagating the space between the radar antenna and the test volume can become altered due to the non-homogeneous nature of the air within that space. The propagation factor of the air can change as a function of height above the ground based on temperature variations, humidity levels, and wind. Clutter and Radio Frequency Interference (RFI) also cause deviations in field planarity but are not associated with the homogeneity of the propagation medium. The combination of fluctuations will impart unknown errors in the RCS measurement.

Practically speaking, there are always errors in the measurement process when collecting data. However, it is unclear how much error exists. Consequently, the confidence level in the collected data is low. Uncertainty in a measurement is the estimation of any remaining error after correcting for all other errors made while recording the measurement. Uncertainty is best expressed as “a possible value that

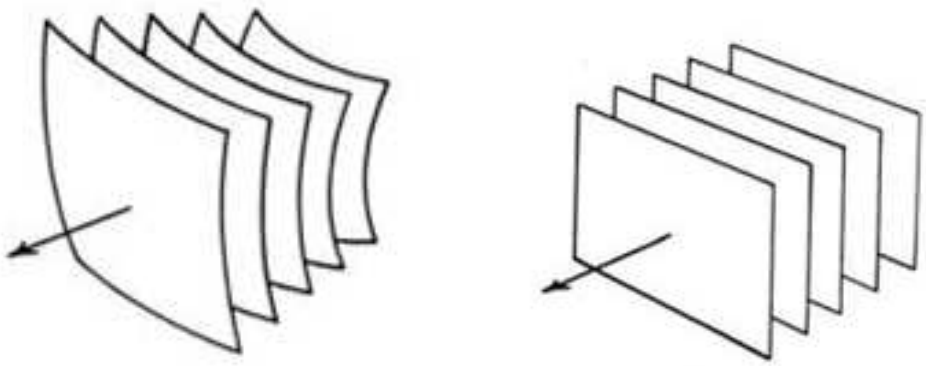

(a) Spherical Wave (b) Plane Wave

Figure 1. Spherical and plane waves: The arrow indicates the direction of propagation [1].

an error may have" [4], or the range the true value lies between as relating to the measurement. The two types of error are bias and precision. *Bias* describes the closeness a measurement is to the true value. *Precision* is the random variation that occurs from taking repeated measurements [4]. Uncertainty analysis collects all the uncertainties found throughout an experiment, quantifying the measurement errors and confidence level in the experimental data.

A critical measurement directly related to the uncertainty in an RCS measurement is planarity of the incident field in the target volume. This is generally accomplished using a one-way field probe [2]. For an outdoor range, the measurement is also performed to ensure the quiet zone (the volume over which the incident field is assumed to be planar) is at the peak of the lobe formed by the interference of the direct path and ground bounce. More critically, the measurement is accomplished to understand fluctuations of the incident field described earlier. The use of a one-way field probe becomes problematic for an outdoor range in terms of the time and effort required to remove and replace a large target from the measurement pedestal. The support structure for the one-way probe can be large and cumbersome, further

increasing installation time and effort. The one-way probe is generally limited to one dimensional translation per measurement configuration. Multiple translational path configurations can be accomplished (horizontal, vertical, angled), but requires a reconfiguration of the support structure and field probe antenna. Also, the translational path and must remain orthogonal to the incident EM wave. Translation paths parallel to the incident EM wave path will capture scattering of the energy indubitably caused by the support structure. Additional complications are added by incorporating the antenna return feed into the support structure.

1.2 Problem Statement

A two-way probe provides flexibility by allowing three dimensional path translation. However, an infrastructure is required to translate the probe through the test volume. An indoor range may have a string system to support the probe, which would be impractical for an outdoor range by sheer size requirements alone. With a string system come additional problems. Although the strings may have a small interference pattern, care must be taken to negate their impact. Additionally, some RCS test facilities may not have the budget to integrate and maintain a string system. The ideal solution is to implement a floating two-way probe with known RCS and position to "map" the entire test volume. Tear down and reset time would be minimized, the probed path could rapidly be altered with minimal time and effort, and interference from any structure would be eliminated.

Previous research [3] was performed in this area determining the potential for a four motored helicopter (quadcopter) as the platform for a geodesic floating sphere to act as a two-way field probe. A geodesic sphere is a spherical cage comprised of a triangular lattice structure specifically sized and shaped to electromagnetically appear as a solid surface of facets. The facets effectively reflect the lower frequency

band. As the size of the facets decrease, the frequency band over which the cage shields the interior increases. The main objective is to have the sphere scatter uniformly as a function of frequency, polarization, orientation, and position, as well as having a relatively large RCS to overcome any underlying clutter or RFI. The geodesic sphere concept begins to approximate an angle independent scatterer. It was determined that a geodesic sphere could potentially act as an effective two-way probe in a previous thesis [3] by concealing angle dependent scatterers at frequencies below the sphere's cutoff.

This thesis will implement a hardware solution by integrating a geodesic sphere and quadcopter with RCS data collection for an indoor RCS test range. By knowing the RCS of the geodesic sphere and quadcopter in combination with knowing the transmitted wave, any deviations from expected results of the reflected wave will indicate the characteristics of the incident wave at the point in space occupied by the two-way probe. Critical to the measurement is accurate knowledge of the geodesic sphere's position and pose in the test volume. Accurate position information is important to properly calculate the expected result as well as pair the actual result to each position in the test volume. The geodesic sphere is not a perfect sphere and therefore does not reflect uniformly in all orientations. An accurate pose measurement will compensate for any RCS measurements collected when the quadcopter was not in a straight and level orientation. Position and pose measurements will be captured using a motion capture system. Furthermore, a flight control system will be developed to control the flight profile of the quadcopter providing customizable probing paths.

For the application of this thesis, a balance must be found between system functionality and sources of uncertainty errors in the field measurement. This thesis will determine that balance, research system capability, and identify potential limita-

tions and improvement considerations to minimize uncertainties in two-way field probe measurements.

1.3 Justification for Research

The sponsoring organization for this research topic is the National RCS Test Facility (NRTF) located at Holloman, Air Force Base (AFB). Members of NRTF are interested in how utilizing the floating sphere concept will improve the quality and efficiency of the field probe operation. To avoid timely tear-down and reset of test articles, the facility implements a retractable one-way field probe located on the centerline of the range, approximately 1000 ft in front of the test volume. Periodically between measurements of targets, the probe extends above the ground to detect and measure distortions in the vertical field profile at one position. The probe does not provide much information about distortions in the field at the actual measurement target location.

Utilizing the floating sphere concept as a two-way field probe could improve our understanding of the uncertainties associated with RCS measurement errors, thereby increasing confidence levels in the data collected. This concept has never been attempted and may identify other possible areas of improvement.

1.4 Investigative Questions

The research focus of this thesis requires answers to the following five questions:

1. Under what circumstances will a commercially available quadcopter operate unrestricted by an integrated geodesic sphere? All airborne vehicles operate under unique flight characteristics given specific weight and balance criteria. Incorporating the geodesic sphere may alter the flight characteristics poten-

tially by interfering with the physical structure and by shifting the center of gravity. Either may cause unrecoverable instability.

2. Is a quadcopter and geodesic sphere capable of acting as an effective two-way field probe? It has yet been determined if a quadcopter and geodesic sphere could effectively act as a two-way. This must be determined before any quantitative evaluation can be made of the accuracy of a quadcopter and geodesic sphere probe measurement.

3. How does the rotation rate of the geodesic sphere affect the quadcopter and geodesic sphere two-way field probe measurement? A sphere uniformly scatters the energy of an incident wave when illuminated from any angle of incidence. The geodesic sphere and quadcopter do not share this ideal characteristic. Rotating the sphere during data collection could statistically "smooth" the measured RCS to equate to the RCS of a sphere.

1.5 Methodology/Approach

The initial effort of this thesis will be to implement flight control capability for the quadcopter. Integrating the motion capture system will provide positional feedback for path planning and aid in the development of customizable flight profiles. Next, the position and pose measurements will be incorporated into the RCS measurement system where each position and pose sample point will be synchronized with each magnitude and phase sample point. Then the geodesic sphere will be integrated with the quadcopter. After fine tuning the flight control system for stable flight characteristics, the system will be ready for data collection.

A systematic process will be used to determine if a geodesic sphere and quadcopter can effectively be used as a two-way field probe. In the first stage, one-way

field probe measurement of the EM fields will be collected. The next step will be to perform field probing measurements using a target known to be an effective two-way probe. Consecutively, two-way field probing will be attempted using a geodesic sphere with pose compensation. The RCS measurements of these initial measurements with any probe will be captured when the probe is stationary. The last stage will be to capture the RCS measurements of a flying quadcopter and geodesic sphere. Position and pose compensation will be applied to the results. This final data will be analyzed and compared to the results from the one-way probe measurements. Success will be determined strictly qualitatively based on general similarities between both probing methods. No quantitative conclusions will be drawn.

1.6 Assumptions

For this research, the following assumptions were made to limit the scope of the project:

1. The Vicon™ Motion Capture system will be utilized to measure and record position and pose data. It is assumed the measurements provided are accurate and will be considered as truth.

2. Effects position and pose uncertainties have on the geodesic sphere two-way probe measurements will be limited and rudimentary. The purpose of this thesis is to demonstrate a proof of concept for system effectiveness. A deeper analysis is provided in another thesis by Captain James Dossett [5].

3. Facilities with high precision RCS measurement equipment were not available. The the Air Force Institute of Technology (AFIT) Advanced Compact Electromagnetic Range (ACER) was available and will be sufficient to provide proof of concept for field probe measurements. The recorded RCS calibration

measurements of the quadcopter and geodesic sphere were acquired at the AFIT ACER facility. It is unknown how deviations in the quiet zone affected the probe measurements and how those errors impact probe compensation.

4. Flight control of the quadcopter is accomplished by communication over Radio Frequency (RF). It is assumed that the communication signal will not interfere with measurements of the field.

1.7 Resources

The quadcopter chosen for this research project is the Parrot® Bebop Drone which can be controlled over a wireless computer connection running Robot Operating System (ROS) commands. The Vicon Motion Capture system providing indoor positional information will interface using National Instruments (NI)™ LabVIEW™ coding software. Radar measurements will be recorded at AFIT's indoor range. The radar measurement system is a Lintek 4000 also controlled by LabVIEW™.

1.8 Overview

In this thesis, *Chapter II* provides the necessary background knowledge and theory to fully understand the concepts used to answer the investigative questions of this research. The implementation of available hardware and chosen software will be covered in *Chapter III*. Additionally, it will illustrate the RCS characterization and flight path development process. The results and analysis will be covered in *Chapter IV*, comparing one-way probe measurements to two-way probe measurements. A summarization of this research effort will be contained in *Chapter V*, along with conclusions and a description of suggested areas offering future work potential.

II. Literature Review

This thesis will utilize a two-way field probe to determine phase deviations of an incident wave within a test volume. To find the EM field deviations, some basic concepts must be understood. This chapter will provide the necessary understanding of the concepts involved in this research.

The first topic discussed will be basic radar principles and systems and the role RCS plays in detection systems. Secondly, RCS will be explained in detail, how RCS is calculated, and how RCS is measured. Further details will be provided explaining the minimum requirements for an outdoor RCS test range where the research will be applied. Additionally, EM wave theory and plane waves will be briefly discussed to illuminate the problem the research is trying to solve. Because a geodesic sphere is being used as the two-way probe, a general overview will describe how the sphere will be designed and the EM theory behind that specific design requirement. Finally, uncertainty analysis will be explained and described how it will serve to improve knowledge of a platform's RCS measurement. Accompanying the development of the key concepts will be discussion of how EM fields are currently being measured to account for RCS measurement uncertainties.

2.1 Geodesic Sphere

The fundamental core of this research effort is in the design characteristics of the geodesic sphere. A Geodesic sphere is assembled by concatenating several triangles of differing sizes together until the final shape is spherical. In creating the sphere, the number of different sized triangles used to build the structure determines the frequency subdivision, 2 ν, 4 ν, 6 ν and so on. This is based on the number of octahedron subdivisions performed to create the final shape of the sphere.

Generally speaking the larger the frequency subdivision the "smoother" the geodesic sphere surface appears [6]. A 2 ν frequency geodesic sphere design was used for the research in this thesis.

Coupling the geodesic sphere's structural design with a fundamental concept of electromagnetics—the waveguide cuttoff frequency. Each one of the triangular openings of the geodesic sphere could be considered as a waveguide. Currently, a closed form solution for triangular waveguides does not exist. However, the closed form solutions for a circular and rectangular waveguide can be used as bookends for understanding what the cutoff frequency may be. The cuttof frequency for a circle and rectangular are found by Equations (1) and (2) respectively [7, 8].

$$f_{c_{circ}} = \frac{\chi'_{mn}}{2\pi r\sqrt{\mu\varepsilon}} \tag{1}$$

$$f_{c_{rect}} = \frac{1}{2\sqrt{\mu\varepsilon}}\sqrt{\left(\frac{m}{a}\right)^2 + \left(\frac{n}{b}\right)^2} \tag{2}$$

where m and n are the modes, χ'_{mn} is the nth zero of the derivative of the Bessel function J_m and provided as a lookup table in [7], r is the radius of the circular waveguide, a and b are the dimensions of the rectangular waveguide, and μ and ε are the permeability and permittivity.

Notionally, by designing the geodesic sphere with cutoff frequencies well below the RCS test equipments operating frequency, the geodesic sphere will appear as if each triangular facet was a solid surface as depicted in Figure 2. By increasing the surface "smoothness" of the geodesic sphere, less uncertainty will be introduced to the field probe measurements

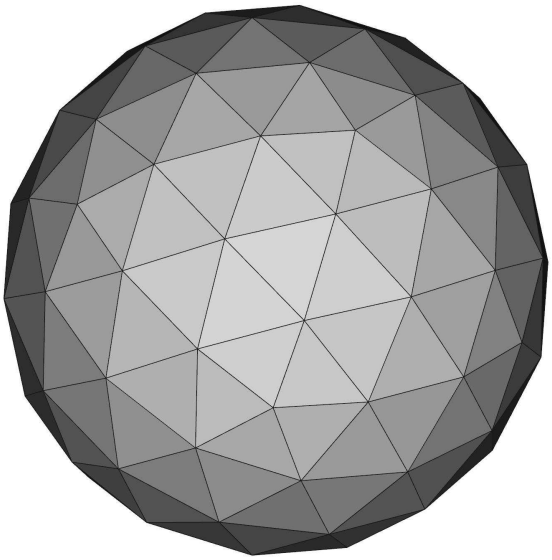

Figure 2. Closed Geodesic Sphere: A $400mm$ radius 3ν geodesic sphere with closed facets.

2.2 Radar

The term radar has become a common word in most vernaculars. However, Radio Detection and Ranging (RADAR) originated as a secretive capability critical to the Allies during World War II. Radar is a system that utilizes the reflections of RF Electro-magnetic (EM) waves to detect objects and accurately calculate the object's distance [9, 10]. The two types of radar systems are monostatic and bistatic. A monostatic system uses the same antenna to transmit the RF as used to receive and detect, while the bistatic system utilizes a second antenna to receive which may or may not be co-located with the transmitting antenna.

The radar transmitting antenna produces an RF EM wave, which propagates through the atmosphere to a target. The incident field induces surface currents on the target which in turn re-radiates or "reflects" EM waves back to the receiving radar antenna. The radar system will then process any signal returns. When power of the reflected EM wave exceeds a specified threshold, a detection is counted by

the radar system. The round trip time measured between transmitting and receiving is used to calculate a range to the target. Figure 3 illustrates a basic block diagram of a monostatic radar system [10].

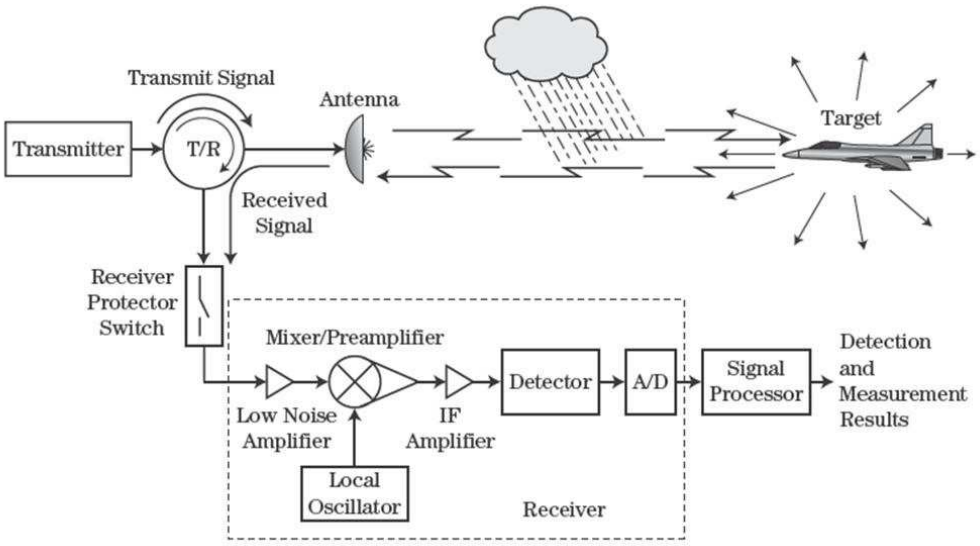

Figure 3. Radar System: Major elements of the radar transmission/reception process [10].

The total distance, R, the EM wave travels is easily calculated by the fact that the waves travel at the speed of light, c (3×10^8 m/s). Multiplying the total time, $\Delta\ T$, from transmit to receive gives the round trip distance. The one-way distance is given by:

$$R = \frac{c\Delta T}{2} \tag{3}$$

Among other considerations, any given radar system is designed to particular specifications balancing the probability of detecting with the probability of indicating a false alarm. As a result, a reflected power threshold is determined. Any power level received above the threshold will be considered a target detection. The power

returned is a function of the power density incident on the target, gain of the systems, antenna efficiency, and the RCS factor of the target being illuminated.

$$P_r = \frac{P_t G^2 \lambda^2 \sigma}{(4\pi)^3 R^4} \tag{4}$$

where:

P_t is the power transmitted

G is the system gain

λ is the wavelength in meters of the RF carrier frequency

R is the range to target in meters

σ is the RCS of the target in square meters.

2.3 Radar Cross Section

The RCS of an object is a theoretical size describing the effective "electric" cross sectional area an object has that will reflect EM waves back to a radar system at some intensity. It can be further described as the projected surface area of an equivalently sized, perfectly conducting sphere that scatters the power observed in a particular direction [1]. The larger the sphere, the higher the echo return to the radar.

Designers of military aircraft are careful in their design to shape the RCS and direct energy in specific directions. Directing radar returns is the fundamental idea behind stealth technology, as illustrated by the example in Figure 4. Careful mission planning determines the ideal flight path where RCS spikes flash radar sites with minimal time to reduce the probability of detection.

Intuitively, when an object is illuminated by an EM wave, the object's physical shape, orientation, and conductive composition determines how much energy re-

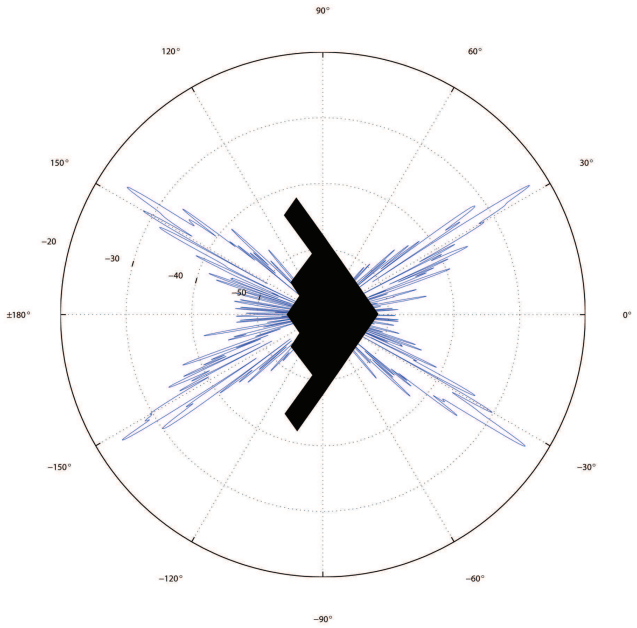

Figure 4. RCS example: B2-like planform flat plate shadow overlaying the theoretical RCS pattern of a flat plate similarly shaped.

flects directly back and how much is scattered in other directions [2]. A perfectly conducting flat plate normal to an incident wave reflects more energy directly back to the EM source than when the plate is 45 ° to the incident wave. Additionally, specular reflections interact constructively and destructively with edge diffractions [11] to build what is known as the RCS profile. The RCS is calculated as the ratio between the incident wave and backscattered wave.

$$\sigma = \lim_{R \to \infty} 4\pi R^2 \frac{|E_r|^2}{|E_i|^2} \tag{5}$$

Taking the limit of R to infinity effectively eliminates the range dependence from the RCS definition. However, doing so requires the incident wave to be planer.

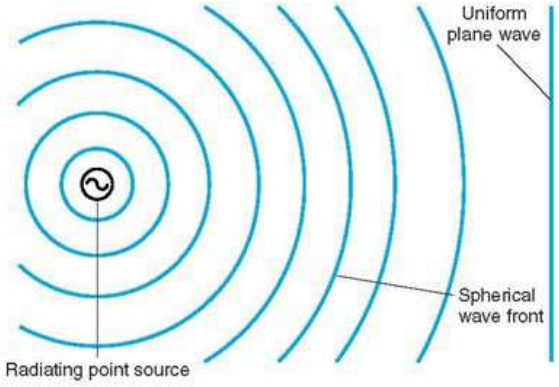

Figure 5. Uniform Plane Wave: Electromagnetic waves radiating spherically from a point source appear uniform and planer at some finite distance from the source [8].

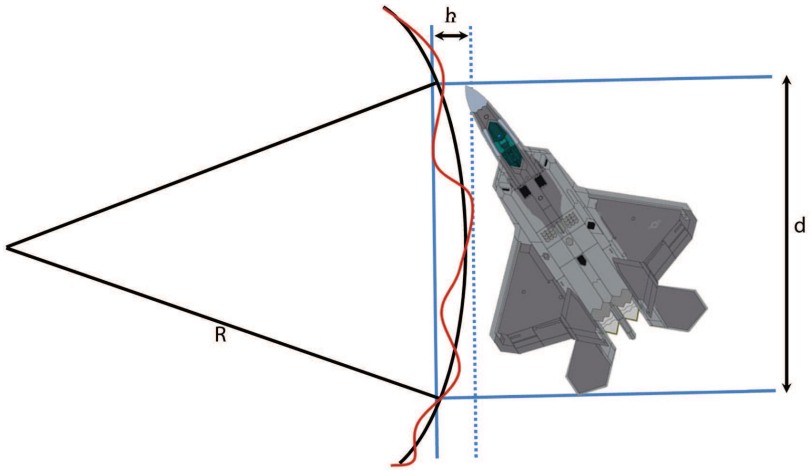

Figure 6. Field Distortions: Phase distortions of an incident EM field.

2.4 Plane Wave and Far Field

Electromagnetic waves radiate from a point source spherically in all directions. At some distance from the source, the waves appear as uniform plane waves illustrated in Figure 5. The magnitude and phase are equal at all points along the phase front [1, 8]. Once plane-waves are achieved, the target is said to be in the far-field.

In order to facilitate the far-field requirement, RCS test measurement facilities must meet certain requirements. The acceptable maximum phase difference found

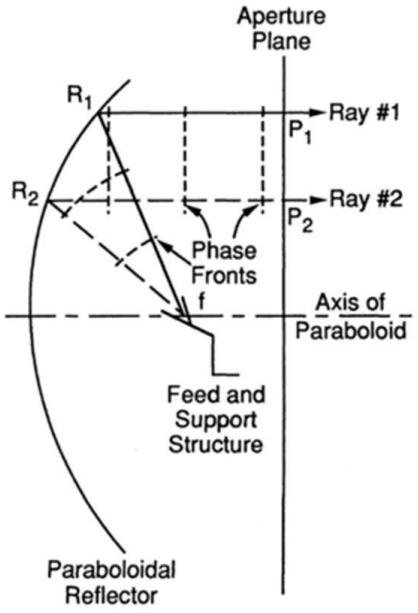

Figure 7. Reflector Plane Wave Generation: A parabolic reflector is used in compact ranges to generate a plane wave in a short distance [2].

in [1, 2, 12] can not exceed $\pi/8$ radians or 22.5 °. Figure 6 illustrates the phase difference, h, for a perfect spherical (black curve) EM wave front and distorted (red line) wave front illuminating a target. Some indoor ranges will utilize a parabolic reflector as a collimator to minimize the required distance. In outdoor ranges, as is the case of the range at White Sands, NM [13], the range must be greater than $2d^2/\lambda$.

Spherical waves can be synthesized to planer by using a lens or reflector to collimate the wave. Similar to a satellite dish collecting collimated rays to a single point at the dish focal point, through reciprocity, spherical waves emitting from a point source feed will reflect planer as illustrated in Figure 7 [2]. The feed antenna and reflector configuration used in the AFIT ACER lab is shown in Figure 8.

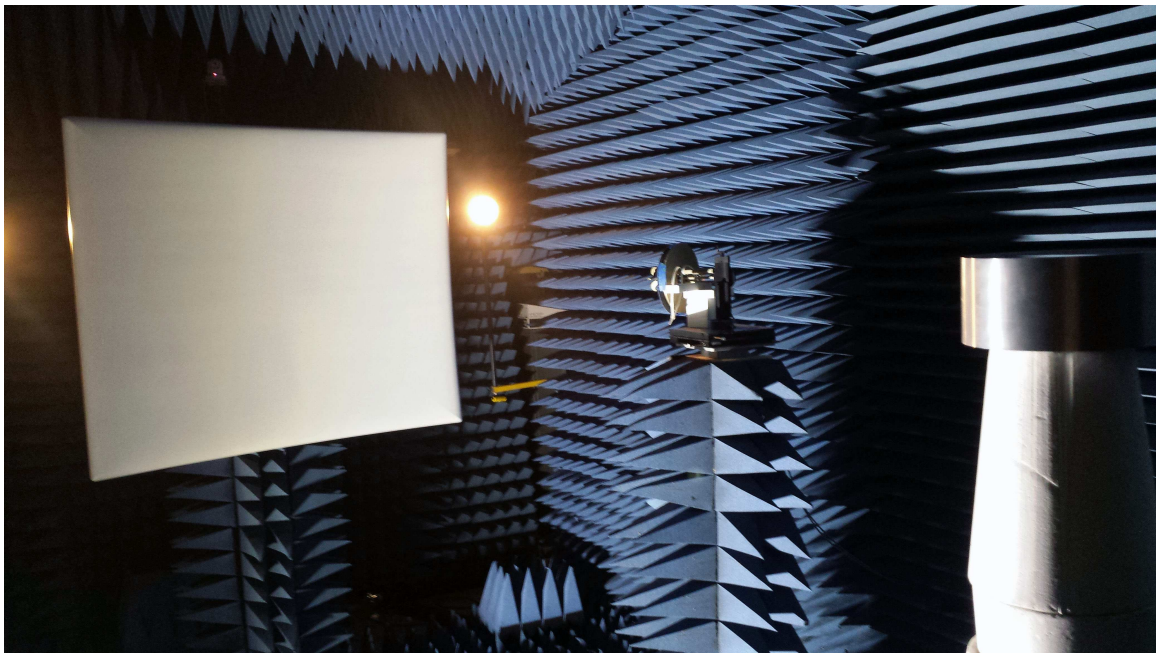

Figure 8. AFIT's ACER Horn Antenna and Reflector: The parabolic reflector and horn antenna configuration at AFITS's ACER lab.

2.5 Uncertainty Analysis

The definition of error is the difference between a measurement's true value and a measured value. Errors fall into two categories, systematic (*bias*) error, and random error [14]. Bias errors in data measurements occur from errors in the instrumentation, errors introduced by the human reading the measured values, and errors introduced by performing the measurement itself. Random errors are caused by noise and will present a Gaussian distribution with adequate samples. Bias error can potentially be removed, where error caused by noise can not.

Uncertainty in a measurement is an estimation of any remaining error after all other error corrections have been made [4]. Many errors in RCS measurements are corrected by diligent calibration techniques. Members from the Air Force Research Laboratory (AFRL) developed a method [15] to provide measurement accuracies of $\pm 0.25\ dB$ using inexpensive high-precision calibration targets.

To quantify the uncertainty in the field calculations, a Root-Sum-Square method [16] will be utilized. The uncertainty can be calculated by:

$$U = 2\left[\sum_{i=1}^{n}(\theta_i U_i)\right]^{\frac{1}{2}} \quad (6)$$

Where θ_i is the measurement result sensitivity and the partial derivative of the result with respect to each i^{th} independent measurement. U_i is the standard deviation of the i^{th} uncertainty source.

2.6 Relevant Research

2.6.1 Quadcopter.

To implement a quadcopter in the system design, a general understanding of the vehicle dynamics was required. A quadcopter's roll, pitch, and yaw angles are denoted in Euler angles as ϕ, θ, ψ, respectively. These angles are controlled by the differential thrust applied by each rotating propeller illustrated in Figure 9. A differential thrust between the port and starboard motor(s) control roll angle. Pitch is controlled by the differential thrust between the fore and aft motor(s). Differential thrust between two pairs of counter-rotating propellers creates a resultant increase of torque causing a yaw. There are many references available regarding quadcopter control and dynamics and should be consulted for a deeper understanding [17–19].

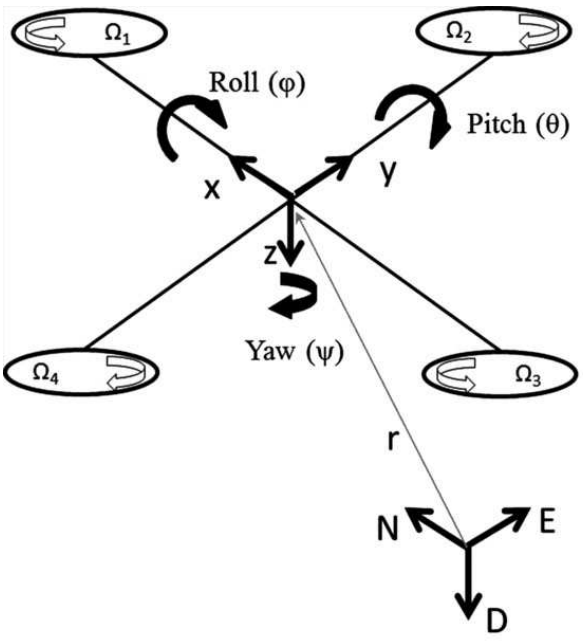

Figure 9. Quad Copter Free Body Diagram: The differential thrust between the quadcopter's motors control the roll, pitch, and yaw angles ϕ, θ, ψ. Translation in along the x, y, z axes results from directing the total thrust force [19].

2.6.2 Motion Capture.

An optical motion capture system was employed to provide accurate position measurements. In an optical motion capture system, an array of Charge-Coupled Device (CCD) cameras are configured to observe a volume of space. The cameras have a light source (usually red or infrared) and capture the light reflected by retro reflective markers. A marker must be visible to at least two of the cameras. Employing multiple cameras ensures a direct line of site [20]. In the software interface, a collection of markers attached to a rigid body can be grouped together as a single object with a measured position and pose. The advantage of using an optical motion capture system is accurate position and pose data with minimal EM interference from the observation equipment.

2.6.3 LabVIEW™ .

Based on its rapid development and easy troubleshooting capabilities, LabVIEW™ is the chosen central platform for software integration and hardware control. LabVIEW™ uses a graphical programming syntax to simplify the implementation of engineering concepts without the steep learning curve of some command line environments [21]. Many tools and add-on packages are available in LabVIEW™ and allowed for a modular design approach. As a result, subsystems were developed and tested using simulated inputs to confirm expected outputs prior to full upper level system integration.

2.6.4 Robot Operating System.

There are some limitations to LabVIEW™. Quadcopter technology is expanding at a rapid pace. As a result some tools and hardware control capabilities were not available. ROS (pronounced Ross [22]) was used to bridge that gap in hardware control. ROS is a command line based interface and does have a steep learning curve for hardware package development. However, the basic concepts and execution of standard commands requires minimal understanding of the inner workings of the software. An added benefit of ROS is its network based communication protocol. Tuft University developed a ROS toolbox for LabVIEW™ [23].

ROS employs a software development scheme to allow multiple independently running programs, referred to as **nodes**, to operate in parallel. Communication between the nodes is accomplished by sending **messages** over uniquely named **topics**. A node can **publish** messages to topics another node **subscribes** to. The central control of linking publishing nodes with subscribing nodes is performed by the ROS master [22, 24]. A simple example of the ROS communication structure is illustrated in Figure 10.

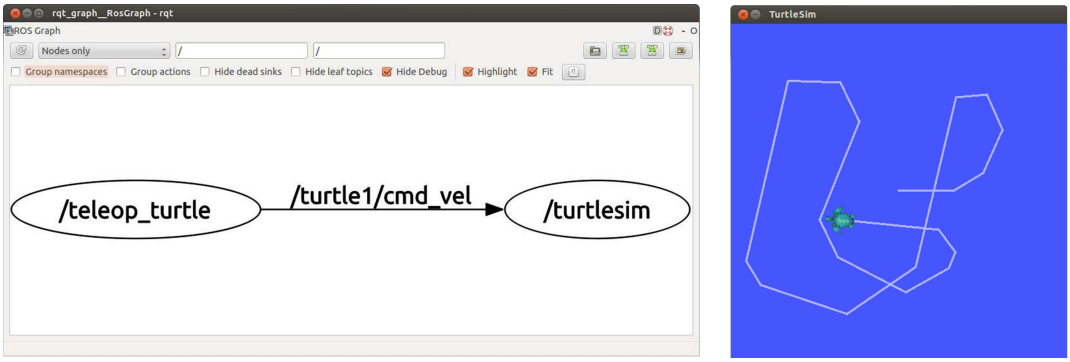

(a) ROS Communication Structure (b) ROS Simulation

Figure 10. ROS Node Communication Example: Keyboard commands are converted to ROS messages by the /teleop_turtle node and published to the /turtle1/cmd_vel topic. The /turtlesim node, subscribed to the /turtle1/cmd_vel topic, interprets the messages as directional controls for the simulated turtle to move about the blue field [22].

2.7 Summary

This chapter provided the technical background necessary for this thesis. Comprehension of basic radar principles is critical to understanding the role RCS plays. Further understanding of how RCS measurements are calculated and the mathematical requirements were provided in addition to the real world limitations. A brief description of EM fields and the development of plane waves was explained. The geodesic sphere was described and explained how the physical characteristics will electrically reflect the radar waves. Finally, uncertainty analysis is needed to apply the final outcome of measured field distortions to an end result measurement. All of the above listed areas collectively develop the research contained in this thesis.

III. Methodology

This thesis has two primary objectives: to engineer an integrated system to control a geodesic sphere encased quadcopter and use the integrated system to measure EM fields with a geodesic sphere encased quadcopter as a two-way probe. To accomplish these goals, the efforts of this thesis were separated into system design and data collection. System design is relatively straight forward—build it then use it. The data collection component was not as straight forward.

To meet the goals of collecting measurement data, three data groups were collected. The first collected data was a RCS characterization of the geodesic sphere and quadcopter. The second and third data groups collected were a measurement of the EM field at AFIT's ACER test facility using a one-way probing method and two-way probing method.

3.1 Sphere RCS Characterization

The sole purpose of the geodesic sphere is to electromagnetically "mask" the RCS response of the quadcopter. Although somewhat symmetrical, the RCS signature of a quadcopter can vary wildly over small changes in orientation. The design of the sphere not only reflects the incident waves before they are influenced by the quadcopter, the sphere eliminates drastic changes in RCS response over different orientations in a predictable manner.

To complete any analysis of probe measurements performed with the geodesic sphere encased quadcopter, depicted in Figure 11, a baseline RCS measurement of the geodesic sphere and quadcopter were accomplished. The baseline included a frequency sweep of the frequencies available at the range, $2 - 18\ GHz$ in $0.05\ GHz$ increments, over the azimuth angles from $0 - 360\ ^{\circ}$.

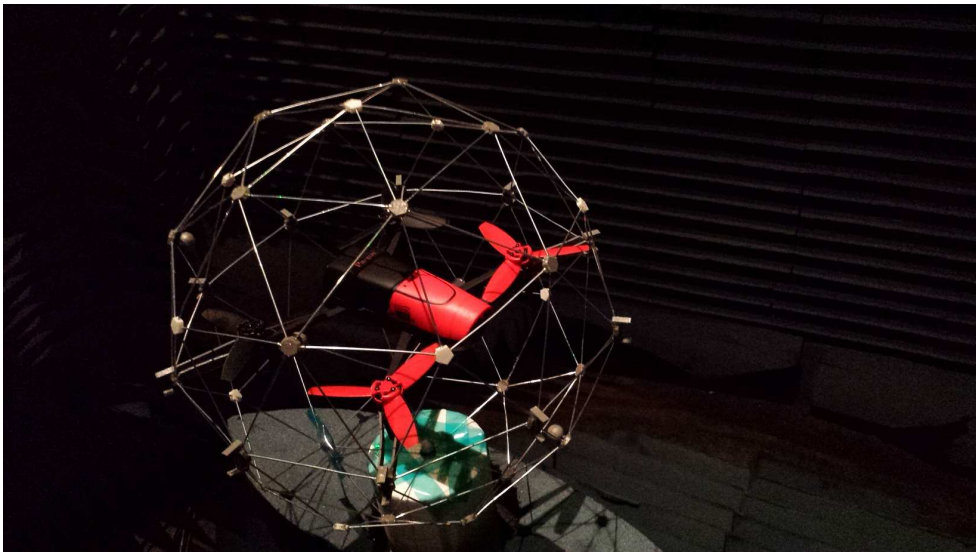

Figure 11. Sphere encased quadcopter: The Bebop quadcopter encased in a $462mm$ **radius** 2ν **geodesic sphere.**

The geodesic sphere used for this research effort was built by Dr. Peter Collins. The sphere is a 2 ν design with a 462 mm radius. Aluminum tubing cut to 100 mm and 118 mm in length were connected to 3D printed plastic pentagonal and hexagonal hubs to form the triangle lattice structure. The sphere was initially built as two hemispheres mated together using 3D printed plastic clips. The mounting arms were specifically designed for the Bebop, attaching to the housing of each motor similar to how the safety hubs attach shown in Figure 12. The cutoff frequency of the sphere was increased from 3 GHz to 4.5 GHz, by creating smaller triangles within the aluminum tube triangles using 24 AWG communication wire. A full and complete description of the geodesic sphere's fabrication and detailed explanation of it's RCS characterization is provided in Captain Dossett's thesis [5].

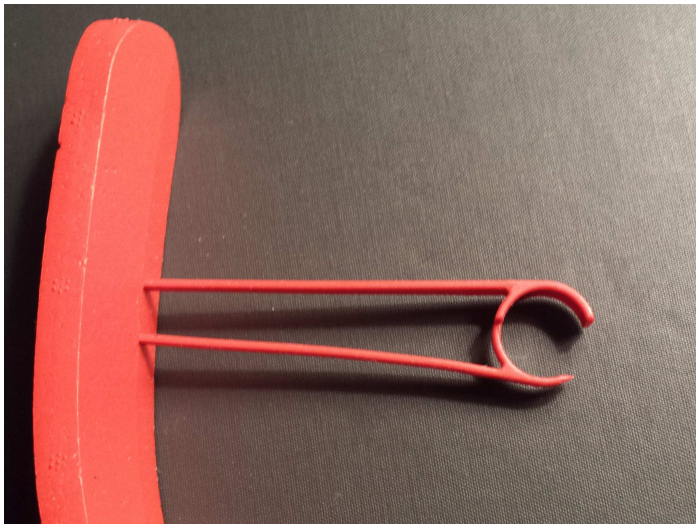

Figure 12. Bebop Safety Bumper Attachement Arm: Safety bumpers for the Bebop quadcopter attach at the base of the port and starboard motor housings.

3.2 System Development and Integration

Briefly described in section 1.5, the system engineering process is fully explained in this section. Whenever possible, an incremental capability approach was taken during the development process. Some integration tasks were accomplished in parallel; the majority of tasks were not incorporated until prior tasks were completed.

There are four primary systems: motion capture, path planning, flight control, and radar data capture. Motion capture is accomplished and processed by a standalone Vicon™ server and transmitted to a central processing computer running LabVIEW™. Path planning is accomplished on the central system using the motion capture data for real time flight control commands. These commands are transmitted by LabVIEW™ via ROS commands to a laptop inside the test chamber. The laptop communicates with the Parrot® Bebop over a wireless network. Finally, the central system transmits motion capture data and receives a time stamp from a computer controlling the radar measurement system. An overview diagram is shown in Figure 13.

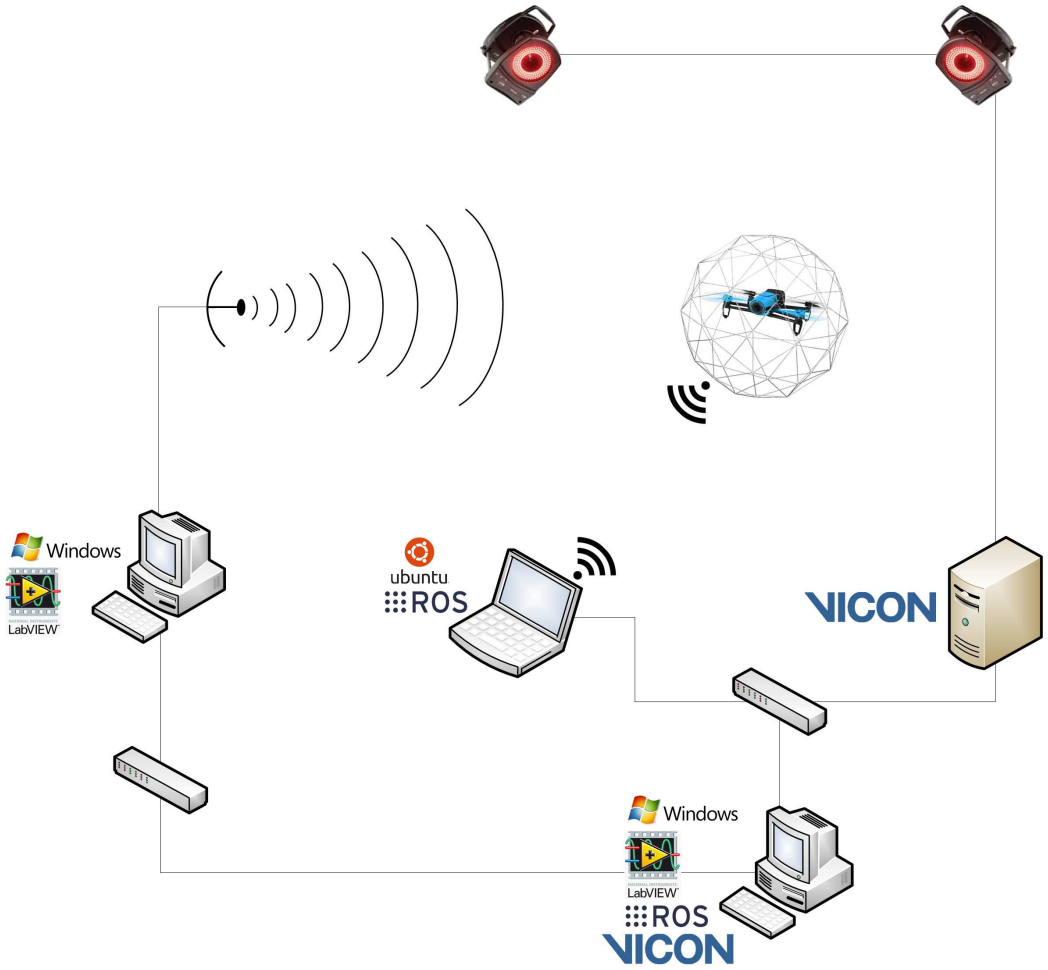

Figure 13. Integrated System Overview: A central computer processes motion capture data and path planning to send flight control signals to a laptop controlling the quadcopter. A secondary radar control computer receives motion capture data synchronized with RCS measurements.

3.2.1 Flight Control with ROS and LabVIEW™ .

The original quadcopter considered for this research was the Parrot® AR Drone 2.0. This was chosen because it was easily accessible from the AFIT's Automation and Navigation Technology (ANT) lab and a LabVIEW™ toolkit [25] was readily available for download and implementation in the LabVIEW™ environment. It was later determined that the integrated geodesic sphere exceeded the weight and balance specifications of the AR Drone 2.0. The sphere designed for the AR Drone weighed 150 g.

Fortunately, a ROS package is available to interface with the Parrot® Bebop Drone 1.0. The Bebop payload capacity enabled relatively unencumbered flight with an attached geodesic sphere with regards to weight and balance. The final sphere design for the Bebop weighed 105 g. Additional benefits of the Bebop are: an improved autopilot hover capability, twice the rotation rate (100 $^\circ/s$ to 200 $^\circ/s$), overall improved response to control inputs, and smaller form factor. The importance of reduced size allowed for a smaller, lighter geodesic sphere design which in turn provided better location estimation of the sphere as a scatterer. As another added benefit, the new geodesic sphere design exhibited smaller facet triangles and thereby increased the cutoff frequency of the sphere.

The first step in developing the flight control system, was to provide manual control inputs through a ROS command interface. This was initially accomplished by entering takeoff and land topic commands by terminal line entry on a laptop running Ubuntu® 14.04.03 and ROS Jade distribution. For safety purposes, the propeller blades were removed from the Bebop. Next, bebop_autonomy ROS topics needed for manual flight were mapped to the control inputs of a Microsoft® Xbox 360® controller and published to the corresponding topics subscribed by the bebop_autonomy nodes. Once the Bebop responded satisfactorily to the controller inputs, the propeller blades were replaced and the Bebop was flown.

The AR Drone 2.0 and Bebop flight control inputs are the same. They are a proportional value between -1 and 1 of a user defined maximum: vertical velocity, angular velocity about yaw, angle in pitch, and angle in roll. If no input is given for the vertical velocity, the internal autopilot will maintain altitude given any combination of roll, pitch, or yaw input.

The next step was to allow manual control of the quadcopter using the LabVIEW™ interface. After configuring the Xbox 360® controller in LabVIEW™, the bebop_autonomy

ROS topics were initialized in LabVIEW™ using VI from the ROS LabVIEW™ toolbox, illustrated in Figure 14. Once the topics were established, LabVIEW™ interpreted control inputs from the Xbox 360® controller then published ROS messages to their respective bebop_autonomy topic, illustrated in Figure 15. Similarly, subscribed messages were translated from their respective ROS topics to retrieve data from the Bebop, specifically battery level and flight status. The flight status topic was used to ensure conflicting takeoff and land commands were not encountered.

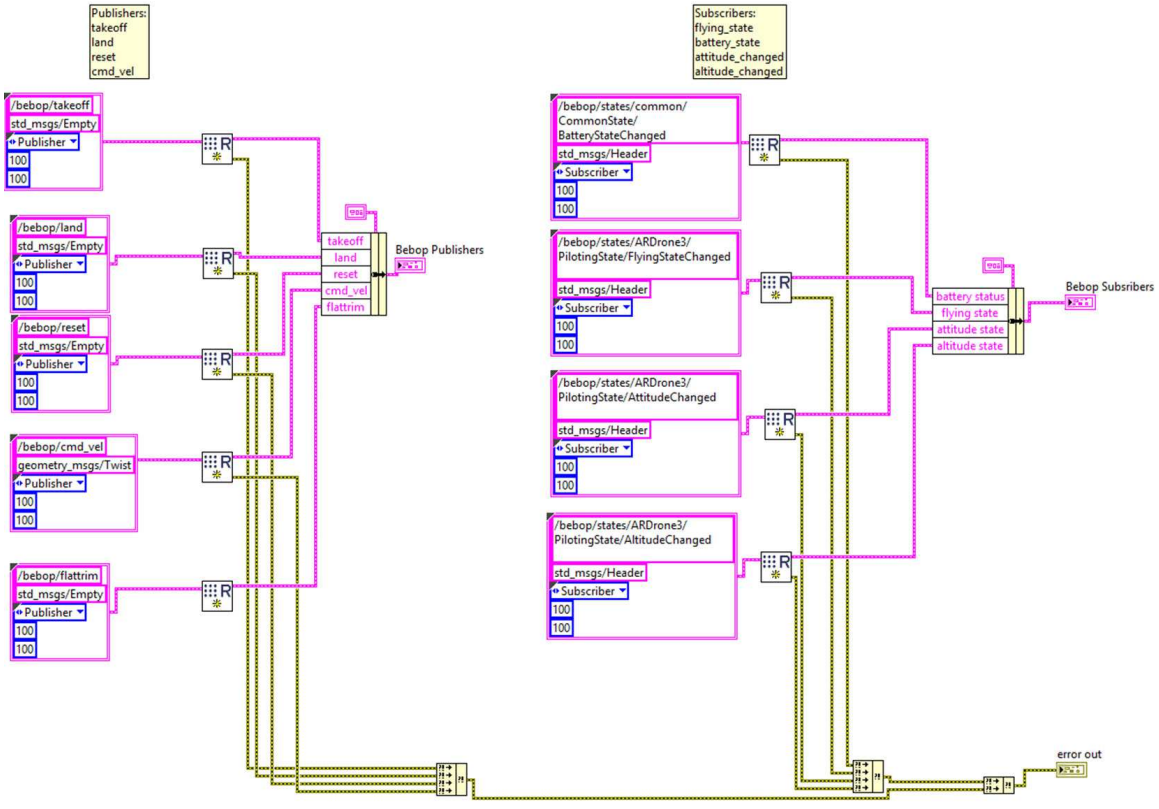

Figure 14. Bebop ROS Topics: Each Published and Subscribed ROS topics were initialized in LabVIEW™.

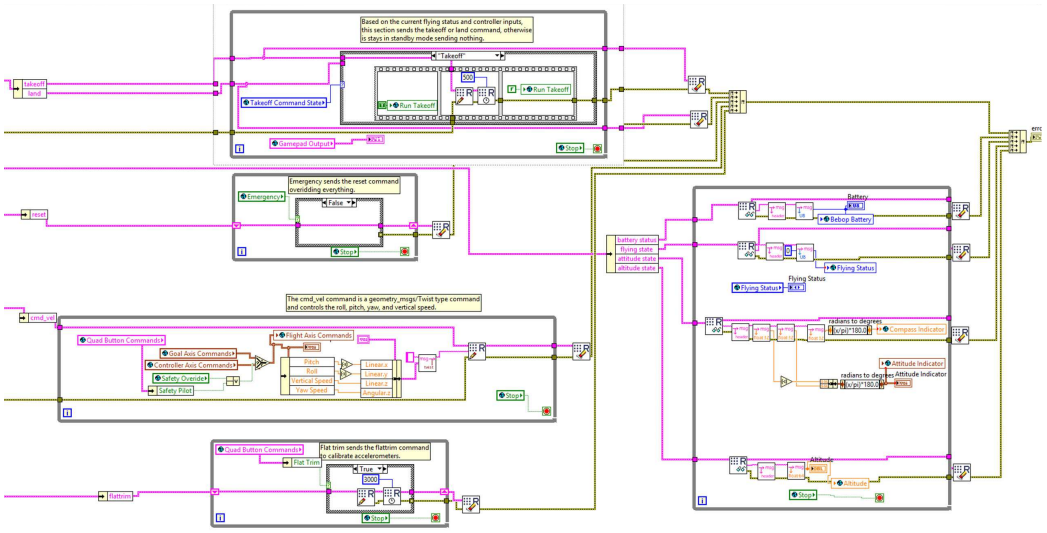

Figure 15. Bebop ROS Commands: LabVIEW™ interpreted inputs for manual and autonomous control of the Bebop are translated and published to ROS topics using VIs from the ROS toolbox.

3.2.2 Motion Capture in LabVIEW™ .

Motion capture served two purposes in the integrated system; feedback for autonomously navigating the test environment and for recording the position a target during RCS data collection. The motion capture system used for the research in this thesis is a Vicon MX™ operating six IR cameras. Vicon Tracker™ 3.1.1 was installed on the same computer operating LabVIEW™. The Tracker software is the primary software that interprets the user defined objects defined with 1.5 *ms* latency for a single object, 1.9 *ms* for five objects and 2.8 *ms* for 10 objects. Figures 16 and 17 show the Vicon Tracker™ interface and relative orientation of the cameras located in the ACER chamber. Figure 18 illustrates reflector placement to allow for unique object creation in the Vicon Tracker™ software.

Vicon™ DataStream SDK v1.5 x64 was installed to interface LabVIEW™ with the Vicon™ data. This software was provided by Vicon™ to allow LabVIEW™ to see the positioning data. A new Virtual Instrument (VI)was created to bring in the position and pose data.

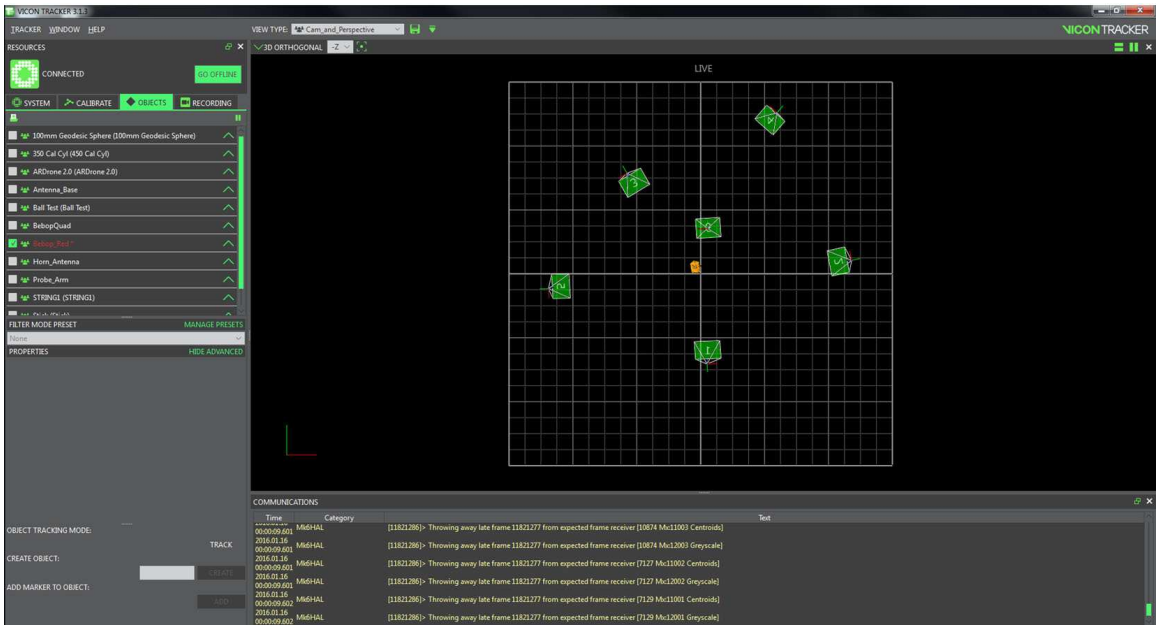

Figure 16. Vicon™ Chamber Overhead View: The Vicon Tracker™ interface and relative camera position placement in AFIT's ACER test facility. The orange object is an object depiction of a Parrot® Bebop.

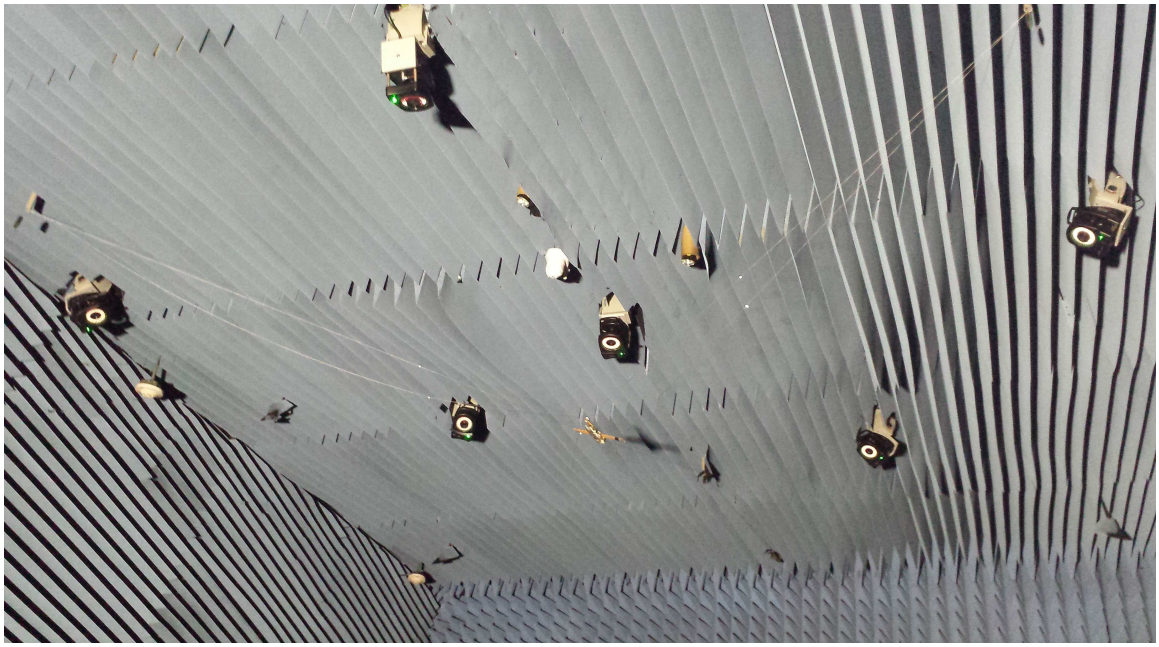

Figure 17. ACER Chamber Ceiling Camera Configuration: Mounted in the cieling of the ACER test chamber are 6 Vicon™ IR cameras to track objects located in the test space with the Vicon Tracker™ software.

Figure 18. Bebop Reflective Dot Placement: By placing multiple IR reflective dots on the Bebop quadcopter, a unique object was recognized by the Vicon™ system for position and pose data capture.

3.2.3 Global to Body Translation.

Once the position and pose data was streaming into LabVIEW™, it needed to be presented in a usable form for path planning purposes. The Euler angles reported by Vicon™ were in a global frame. To find the local body referenced angles of roll, pitch, and yaw (ψ, ϕ, θ), Euler XYZ angles (α, β, γ) were converted from the inertial body to the vehicle body angle about the global z-axis (γ) using the matrix found in [26]:

$$R_i = \begin{bmatrix} cos\ \gamma & sin\ \gamma & 0 \\ -sin\ \gamma & cos\ \gamma & 0 \\ 0 & 0 & 1 \end{bmatrix} \tag{7}$$

$$\begin{bmatrix} \psi \\ \phi \\ \theta \end{bmatrix} = R_i \begin{bmatrix} \alpha \\ \beta \\ \gamma \end{bmatrix} \tag{8}$$

Once the quadcopter's pose was properly referenced, a delta position vector between a current and goal position was calculated. The Vicon™ system produced the six-dimensional position information based on its defined global coordinate system. In order for the quadcopter to perform the same in any orientation with respect to the global system, a body frame rotation was accomplished. The Vicon™ angles for roll, pitch and yaw (ϕ, θ, ψ) were put into the direction cosine matrix $\mathbf{C_n^b}$, where c and s are *cos* and *sine* respectively [27].

$$\mathbf{C_n^b} = \begin{bmatrix} c\theta c\psi & c\theta s\psi & -s\theta \\ s\phi s\theta c\psi - c\phi s\psi & s\phi s\theta s\psi + c\phi c\psi & s\phi c\theta \\ c\phi s\theta c\psi + s\phi s\psi & c\phi s\theta s\psi - s\phi c\psi & c\phi c\theta \end{bmatrix} \tag{9}$$

A position delta array was created between the desired position coordinates $\mathbf{X_{com}}$and the Vicon™ measured position $\mathbf{X^n_{meas}}$,

$$\mathbf{\Delta X^n} = \mathbf{X_{com}} - \mathbf{X^n_{meas}} \tag{10}$$

,

and multiplied the rotation matrix by the position delta array.

$$\mathbf{\Delta X^b} = \mathbf{C^b_n}\ \mathbf{\Delta X^n} \tag{11}$$

The output of that multiplication resulted in the x, y, z deltas in the body frame of the quad-rotor.

3.2.4 PID Development and Tuning.

Proportional, Integrator, Derivative (PID) controllers were added to each of the 4 control inputs. In order to optimize the individual PID controllers the capability to record data points over a specified time period was created. The data gathered was input signals to the quad-rotor and VICON observed velocities. A total of 7 data runs were collected at 10000 ms each. This equates to 200 data points at 50 ms each. The first five runs were varying manual stick inputs controlling vertical vel, yaw vel, x vel, and y vel while in hover mode. To get a better representation of the drone's flight characteristics, hover mode was turned off and full deflection was input into the y direction.

The collected data was fed into a LabVIEW transfer function generating VI. The VI outputs a transfer function of the order specified. This transfer function was then simulated to model the quad-rotor's response to a specific input. The individual transfer functions and responses are seen below.

3.2.4.1 Quadcoptor Transfer Function.

$$H_{(x,y)}(s) = \frac{-1214.66s + 5697.77}{0.00061107s^3 + 0.361154s^2 + 1.55707s + 1} \quad (12)$$

$$H_z(s) = \frac{1075.23}{0.0396208s^2 + 0.30358s + 1} \quad (13)$$

$$H_{yaw}(s) = \frac{-0.086414s + 1.62728}{0.00066499s^2 + 0.172215s + 1} \quad (14)$$

3.2.4.2 PID Tuning.

Once the transfer functions were determined, the PID needed to be tuned. A step by step tutorial guide was used, www.ni.com/tutorial/6931/en/, specifically for the PID controller VI was used. Upper and lower output boundaries from PID controller were set at -1 to 1. After trial and error in simulation with an impulse response of 400 mm for X, Y, and Z and $\pi/2$ for Yaw, the initial PID controller coefficients were used for flight test. The simulated impulse response for X and Y can be seen in Figure 19. Minor adjustments to the PID coefficients were required to achieve the desired flight characteristics.

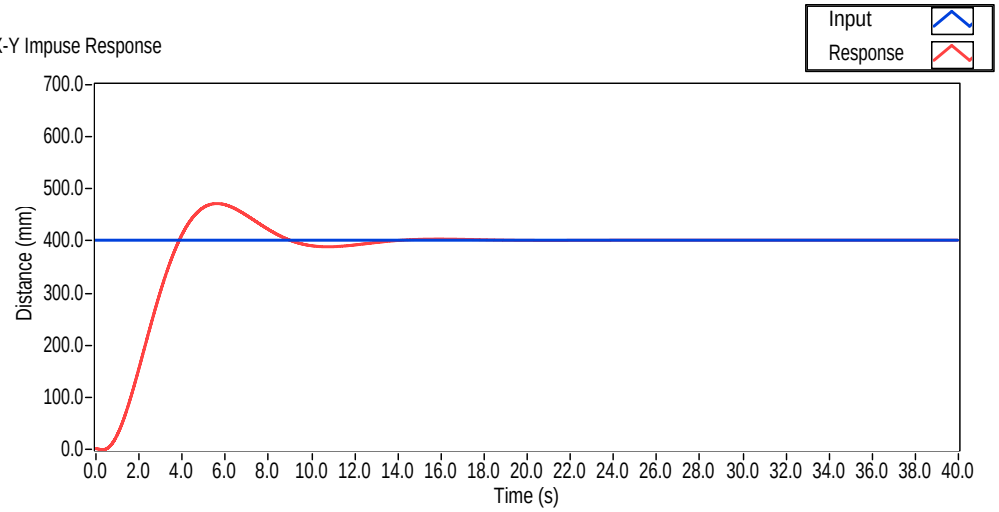

Figure 19. PID Tuning: X and Y direction PID controlled impulse response.

3.2.5 Path Planning.

After fine tuning the PID controllers the Bebop demonstrated adequate flight characteristics when commanded to navigate manually defined way-points in the Vicon™ space. The three flight profiles were the last step developed in the flight control system, an XZ plane raster scan, XY slant raster scan, and helical scan.

For the XZ plane and XY slant raster scan, the user will define the desired end-points of each scan with the number of intermediary points desired. An upper and lower altitude are defined with number of intermediary points. A translational velocity between way-points must also be defined by the user. At the beggining of the flight, the highest altitude is reached first. The scan altitude is lowered for each subsequent lateral scan. The XZ plane raster scan flight profile allows the user to scan multiple XZ planes for different values along the y-axis.

The helical scan converts the translational velocity into a tangential velocity for the circle or ellipse created by the user inputs. The user will also enter the starting and ending altitude with a number of rotations required.

Once the user defines the flight profile specifications, an array of way-points is built. When the mission is activated, the quadcopter will navigate the way-points using a state machine. The first state is to translate to the first goal way-point. If the distance to the goal way-point is less than a user defined proximity value, $200mm$, the quadcopter will hold it's current position for $0.5s$. This hold state is to allow the quadcopter an opportunity to approach the desired way-point without getting "stuck" for a long period of time. Afterwards, an intermediate goal location increments, at the rate determined by the user, to the next goal way-point. The cycle repeats until the final way-point is reached.

3.2.6 Position and RCS Data Synchronization.

The flight control system with motion capture and automatic way-point translation was functional. The final integration step for the total system was to synchronize position data from the Vicon™ system with the RCS data on the Lintek 4000 radar system. Fortunately, the Lintek 4000 uses LabVIEW™ to interface with the radar control hardware. In addition to local and global variables, LabVIEW™ utilizes network shared variables. This feature allowed the position data reported by Vicon™ to be shared with the Lintek 4000. Within the LabVIEW™ structure of the Lintek 4000 machine, the position and pose data of the Bebop is recorded to a file at the same time the data from the frequency sweep is recorded. The length of time between position recordings is dependent upon the frequency band and increment frequency defined in the Lintek 4000 interface. For redundancy and potential improvement in position fidelity, the time stamp of the computer running the Lintek 4000 LabVIEW™ interface is shared with the computer running the Vicon™ and flight control software. This may allow for post process synchronization of the position data with a higher fidelity in position and pose.

The timing accuracy of the each computers timebase is accurate to 1 ms [28]. Loading of the CPU can introduce jitter. Timing between the two computer systems may also be delayed 2 to 10 μ by the network switches, with an additional 122 μs for high traffic [29].

3.2.7 Integration Issues.

The AR Drone and Bebop are equipped with a downward facing camera and ultrasonic sensor. At altitudes less than 8 m the quadcopter's altitude is maintained based on readings from the ultrasonic sensor. When no pitch and roll commands have been input, the quadcopter will go into a hover mode. The camera is acti-

vated in hover mode to maintain position using image processing. The design of the sphere had a connecting hub located directly in the path of the camera and ultrasonic sensor. It is unclear which one had the most detrimental impact, but the bottom pentagon of aluminum tubes were removed to eliminate interference of either sensor.

After the geodesic sphere was attached to the Bebop, it was expected that flight characteristics would change from the increased weight and altered moment of inertia. However, intermittently the Bebop would yaw without a yaw command given. In some instances after a yaw input was given, the Bebop would continue rotate after the input was removed. No clear pattern was recognized to determine the cause of this issue. It is believed that the physical attachment points inadvertently would impart a strain on the struts, rotating the motor, thereby changing the directional force vector of lift. At one point, the sphere attachment arms were zip tied to the struts of the Bebop. This caused an uncontrollable rotation immediately after take-off.

One of the goals of this thesis research was to determine what affect, if any, different rotation rates had on field probe measurements. This area could not be investigated. For a quadcopter, a rotation in yaw is initiated by an increased resultant torque. Two diagonal motors, rotating in the same direction, increase their propeller rotation rate thereby increasing torque in one direction. The remaining motors, rotating the opposite direction of the other two, reduce their propeller rotation rate and thereby reduce a counteracting torque. The increase in lift from the faster motors compensate for the decrease in lift of the slower motors. As a result, altitude is maintained and the resultant increase in torque about the z-axis induces a yaw. With the additional weight of the sphere, any rotation in yaw greater than 65 $^{\circ}/s$ caused the Bebop to lose altitude control and descend regardless of vertical

velocity inputs. This phenomenon paired with the intermittent rotation problem described above eliminated the ability to investigate the influence of rotation rates on two-way probe measurements.

3.3 RCS Measurement Calibration

To remove systematic errors in RCS measurements and tie the measured signal levels to RCS values, the measurement must be calibrated. Prior to analysis, all two-way probe RCS measurements were calibrated. The calibration process required measurement of the background, any target mounts present during a measurement, and measurements of a level 700 and 950 squat calibration cylinder. The equation [15] for providing a calibrated measurement is:

$$\sigma_{cm} = \left[\frac{\sigma_{tar} - \sigma_{bkg}}{\sigma_{cal\ meas} - \sigma_{cbk}}\right] \sigma_{cal\ thr} \tag{15}$$

$$\varepsilon = \frac{\sigma_{cal\ meas}}{\sigma_{cal\ thr}} \tag{16}$$

Where:

σ_{cm} = Calibrated measurement

σ_{tar} = Measurement of target (on target pylon mount)

σ_{bkg} = Measurement of background only (target pylon mount)

σ_{cal} = Measurement of calibration target (750/900 squat cylinder)

σ_{cbk} = Measurement of calibration background (calibration target pylon mount)

$\sigma_{cal\ thr}$ = Theoretical value of calibration target

Additionally, the 750 and 900 cylinders were calibrated to one another. The statistics of the difference between a cylinder's calibrated measurement and it's theoretical RCS, bounded the uncertainty of measurements made with that particular calibration.

3.4 EM Field Measurements

The primary focus of this thesis research effort is encompassed in the actual measurements of the EM fields using a geodesic sphere encased quadcopter. As described in Chapter I, a systematic approach was taken to ascertain the utility of a geodesic sphere encased quadcopter acting as a two-way probe. First one-way probing measurements were accomplished. Then it was verified the ACER test lab was capable of performing two-way probe measurements. Finally, a two-way probe measurement was accomplished using an airborne geodesic sphere encased quadcopter. The full details of how these measurements were accomplished and their analysis are provided in Chapter IV.

3.5 Summary

In order to measure EM fields using a geodesic sphere two-way probe, the RCS measurements of the geodesic sphere must be known. Knowledge of the geodesic sphere's RCS came from characterization measurements. From there the RCS measurements were associated with the geodesic sphere's position and pose. By combining information from the geodesic sphere's RCS characterization, EM fields measurements, and uncertainty analysis, the EM fields can be determined and represented.

IV. Analysis and Results

This chapter will discuss the setup, results, and analysis of the process for validating a Geodesic Sphere used as a two-way probe. The process was implemented in three stages. Stage One required knowledge of the test chamber's field characteristics measured by a one-way probe. The one-way probe measurement was established as the foundational baseline of comparison for the final flight tests. Stage Two implemented the two-way probe concept. A path to phase relationship comparison was made between an object with known phase response and the geodesic sphere. Stage Three incorporated different flight paths of the quadcopter with and without the geodesic sphere. Comparisons were made to the one-way probe baseline to determine the overall effectiveness of the two-way probe concept. Additionally, limitations and deficiencies were identified and will be discussed further in Chapter V.

All measurements were conducted at AFIT's RCS lab. Position (x, y, z) and Pose $(roll, pitch, yaw)$ data points were captured and recorded using the Vicon™ Tracker and DataStream software. The x, y, z coordinates were measured in millimeters (mm) and the pose orientation angles were measured in degrees (°). Position, pose and a time stamp of the radar computer were recorded at the end of a polarization's frequency sweep, not at the time each individual frequency measurement was taken. This was due to a lack of understanding how the LabVIEW™ software controls the radar system's measurement timing. Knowledge of a target's position and pose data at each frequency sweep sample facilitated post processing visualization of a phase front's characteristics in the test chamber.

4.1 Expectation

When determining the field characteristics within the radar test chamber, the expected outcome from all measurement sources and frequency was a field with a minimum of 914.4 mm × 914.4 mm (3 ft × 3 ft), quiet zone arbitrarily centered 500 mm above the pedestal with a path parallel to the chambers centerline. The quiet zone was expected to be oriented such that from the central point above the pedestal platform, estimated visually and defined in the Vicon™ space as the (x,y,z) coordinates $(0, 0, 500)$, the difference in phase between $(0, 0, 500)$ and $(0, \pm 452.7, 500)$ should not exceed the standardized $\frac{\pi}{8}$ radians or 22.5 ° explained in Chapter II. Where ± 452.7 mm is half of 914.4 mm and would place the center of the phase front in the center of the quiet zone. The same should be true when comparing the phase difference between the points $(0, 0, 500)$ and $(0, 0, 500 \pm 452.7)$. Moving away from the radar antenna and reflector was established as the positive y axis. Positive x and z are defined as right-hand orthogonal to the positive y-axis. Figure 20 illustrates the orientation of the Vicon™ space in relation to the AFIT's RCS test chamber. The orange blob was a Vicon™ object represention of a Parrot® Bebop Drone placed on a foam column in the center of the test chamber. The Vicon™ origin was established in the Vicon™ software using a 5 point calibration "wand" provided as shown in Figure 21.

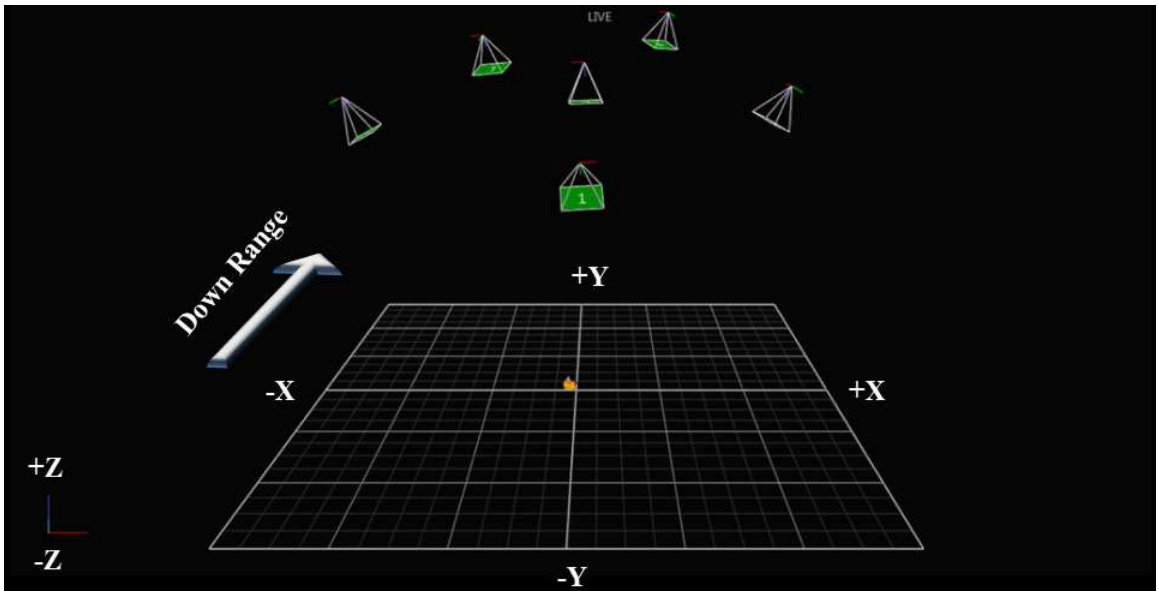

Figure 20. Chamber Layout: Orientation of the Vicon™ x, y, and z axis as configured in the radar chamber.

4.2 One Way Probe Results and Analysis

Prior to the work accomplished in this thesis, the actual field characteristics within AFIT's radar chamber were unknown. To properly understand the effectiveness of the two way probe concept, a better understanding of the field's characteristics was required. This was accomplished using a one way probe in the form of a horn antenna attached to a rail capable of translating along the rail. The pur-

Figure 21. Vicon™ Calibration Wand: Wand for Calibrating the Vicon™ motion capture system.

pose of establishing the one-way probe baseline was not to directly compare for exactness with the two-way probe. Fundamentally it was assumed that field interactions with the rail and other components of the apparatus cause errors in one-way probes. The one-way probe test was designed to confirm the two-way probe's capability to determine basic characteristic's of a phase front's shape in a test chamber.

To establish a foundational basis of comparison of the one way probe's measurements to the Quad Probe's measurements, a Vicon™ object was created representing the horn antenna. The horn antenna's Vicon™ object centroid was located at the cross-sectional center of the horn on the plane representing the circular end. The placement of the reflective dots seen in Figure 22a directly correspond to the orange dots found in the Vicon™ screen capture seen in Figure 22b. The subsequent object centroid defined in the Vicon™ software was represented by the subdued cube. All phase measurements captured with the one-way probe reference the aforementioned object centroid of the horn antenna. It should be noted that

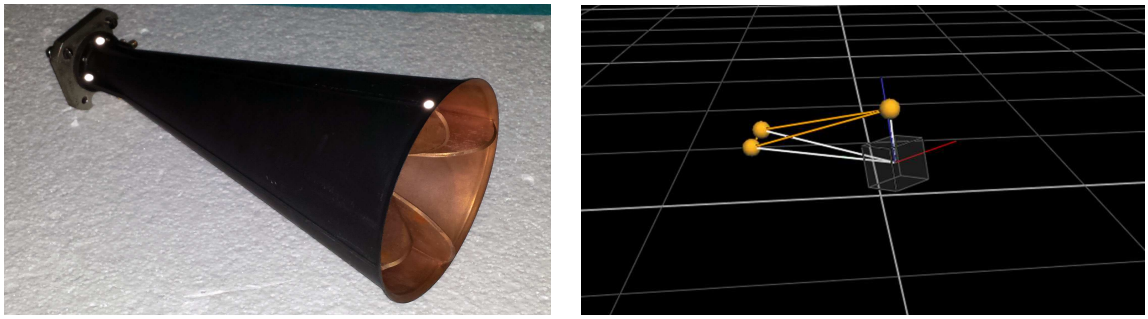

(a) Horn Antenna (b) Horn Antenna Vicon™ Object

Figure 22. Horn Antenna in Vicon™: Refelctive dots were added to the Horn Antenna to create a Vicon™ track-able object.

a calibration for the horn measurement was not accomplished. The impact of the antenna pattern on the measurement was also not considered. These were both assumed to not have a detrimental impact to the results because this research was solely focusing on the phase of the radar measurements. Figure 23 depicts the an-

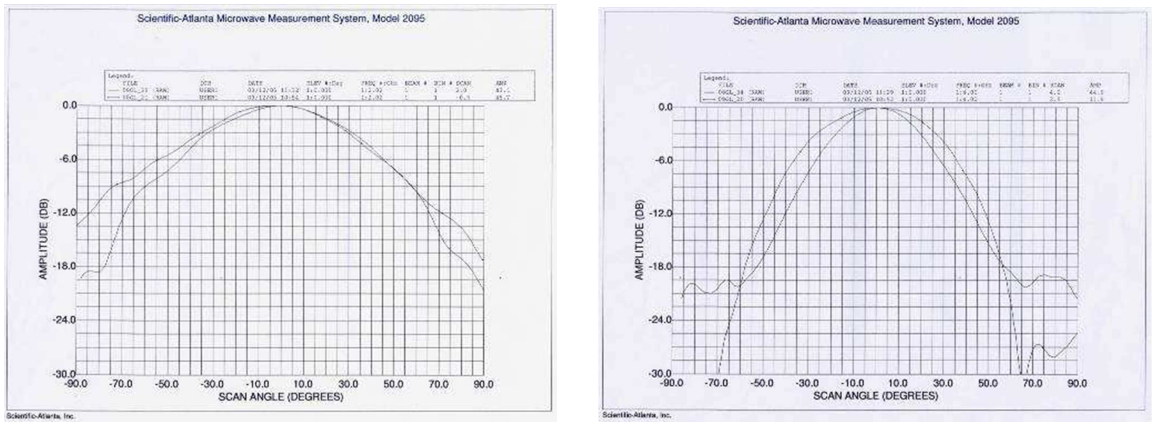

(a) 2 GHz (b) 4 GHz

Figure 23. Quad-Ridge Double Polarization Antenna Pattern: Antenna pattern for 2 and 4 GHz of a Coaxial Horn Quad-Ridge Double Line Polarization Antenna similar to the one used in this research.

tenna pattern when viewed at -19 ° of a Quad-Ridge Antenna similar to the one used for this research. Calibration and impacts of the antenna pattern may need to be considered in future work.

The antenna's lateral position was controlled by a system of pulleys and gears attached to a rotating puck driven by the pedestal's control mechanism. Each 360 ° of rotation of the pedestal mechanism translated the antenna 13 mm. Each measurement configuration accomplished was captured by driving the pedestal control mechanism in 50 ° increments, resulting in a translation of 1.8 mm. Figure 24 illustrates the horizontal and vertical configurations of the one-way probe.

A total of four primary measurements were conducted. Three measurements were accomplished in the horizontal configuration with the fourth in the vertical configuration. The translational endpoints of the measurements are listed in Table 1. The angle documented with each measurement configuration was in reference to the x-axis.

The physical translational path of the probe, as represented in the Vicon™ space, is illustrated in Figure 25. The visible short distance oscillations of path tra-

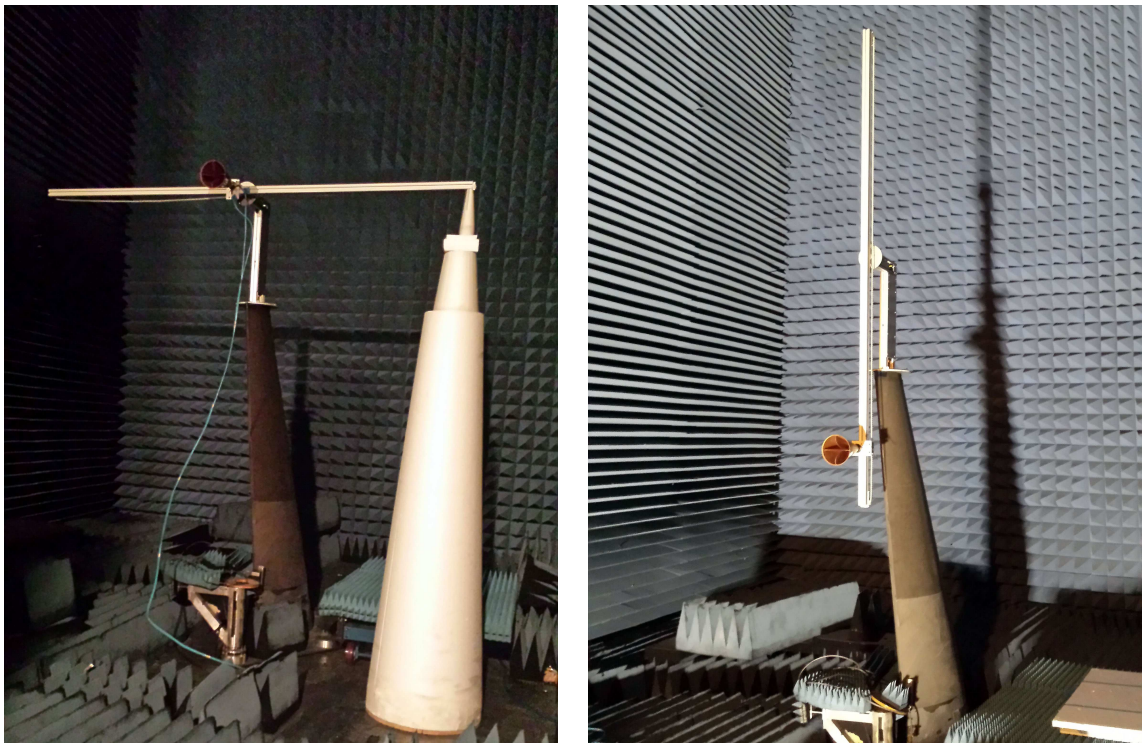

(a) Horizontal (b) Vertical

Figure 24. One Way Probe: A Horn Antenna configured on a rail to translate through the radar field measuring magnitude and phase at specific coordinates in the chamber.

jectory may be caused by the jitter previously observed in the Vicon™ system. Deviations over long distances were attributed to a combination of the physical movement of the probe arm and possible drift in the Vicon™ system over long durations.

The resulting phase front's characteristics were observed as illustrated in Figure 26. When the rail was perpendicular to the downrange direction is represented by the blue curve in the plot. Angling the probe 19 ° downrange exacerbated the fields slanted nature, as shown by the red line. The measurement appeared the most planar when the probe was rotated −19 °, as indicated by the yellow line.

Table 1. One-Way Measurement Endpoints: Translational endpoints for One-way probe measurements

Measurement	Start(mm)	End(mm)	Pol	Freq(GHz)
Horizontal $\parallel$ X	$(998, 369, 505)$	$(-1012, 345, 498)$	HH/VV	$2 : 0.05 : 18$
Horizontal $\angle 19^\circ$	$(1110, 627, 504)$	$(-994, 164, 507)$	HH/VV	$2 : 0.05 : 18$
Horizontal $\angle -19^\circ$	$(1091, 52, 506)$	$(-1005, 784, 497)$	HH/VV	$2 : 0.05 : 18$
Vertical $\parallel$ Z	$(-43, 391, -698)$	$(-59, 368, 1654)$	HH/VV	$2 : 0.05 : 18$

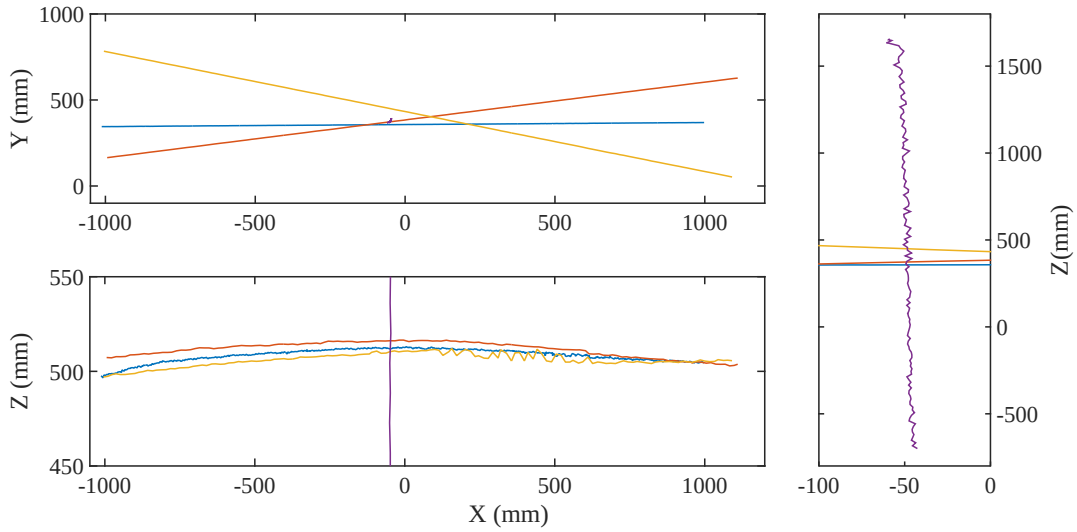

Figure 25. Paths of One-Way Probe: The recorded path of the one-way probe measured in the Vicon™ space, blue line was the probe translating orthogonal to the downrange direction, the red line represents the path angled 19°, the yellow line was -19° and the purple represents the vertical translation.

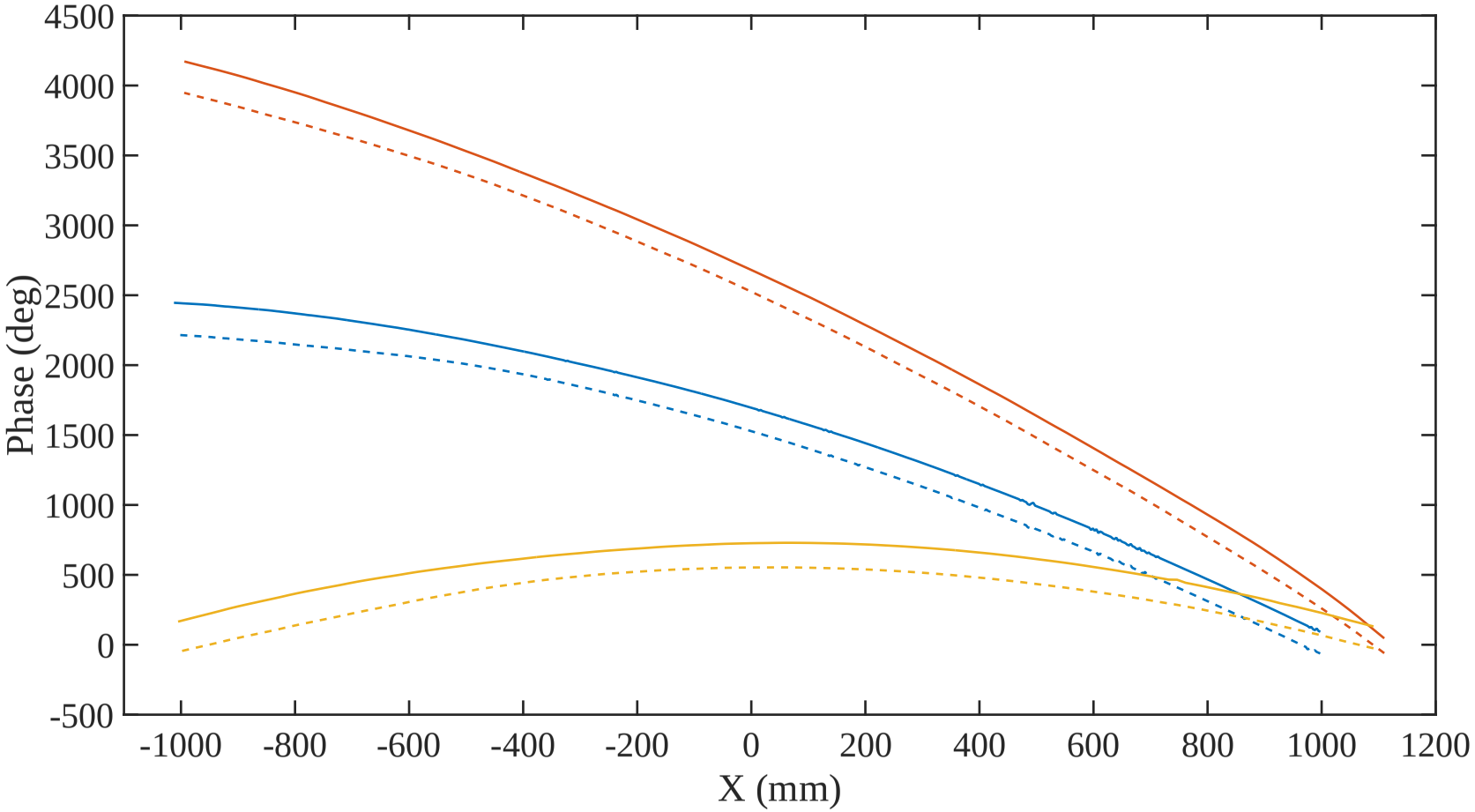

Figure 26. One-Way Probe Measured Phase: The measured phase for each orientation of the horizontally configured one-way probe. Similarly to the path measurements, the blue line was from the orthogonal measurement, the red line was the 19° angled measurement, and the yellow line was the -19° angled measurement. The solid and dashed lines were the vertical and horizontal polarizations, respectively.

4.2.1 Causes of Deviation.

The angled nature of the phase front was most likely caused by cross range offset of the feed antenna. Figures 27 and 28, illustrate variations of the phase front for changes in lateral position, elevation, and frequency. Additionally, the observed phase deviations along the x-axis indicated the reflector was misaligned about its central y axis.

When the -19 ° measurement data were observed, the true dimensions of the quiet zone was calculated for each frequency in both width and height shown in Figures 29 and 30. For the $2 - 5\ GHz$ frequency band, the average dimension of the horizontal quiet zone was 477 mm and the average dimension for vertical was 461 mm. Both of the horizontal and vertical dimensions were less than the assumed 914 mm. The cause of the large lobe deviation shown in Figure reffig:Horz20 is unknown.

The angled appearance of the field was not anticipated, however could be used to demonstrate the utility of using a quadcopter inside a geodesic sphere to more rapidly determine EM field characteristics and deviations. The software was designed to easily allow alterations to the flight path. Re-creating the -19 ° one-way probe measurement was accomplished by providing the two end-points and will be discussed later in this chapter.

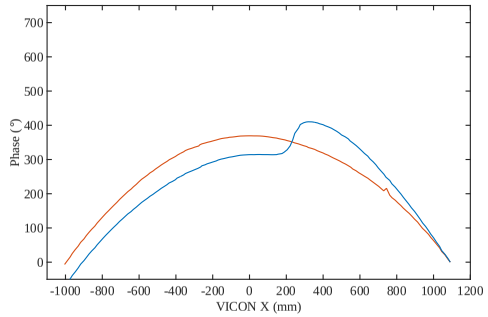

(a) $2.0GHz$

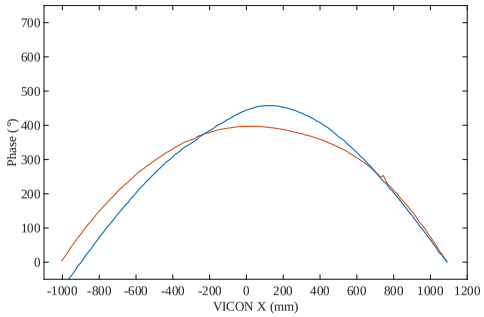

(b) $2.5GHz$

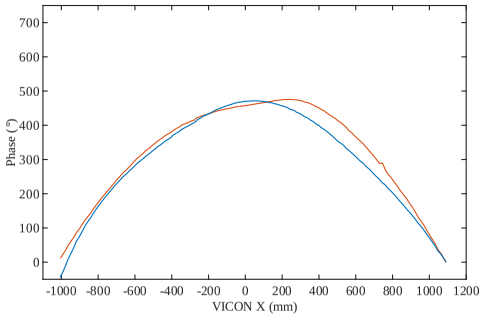

(c) $3.0GHz$

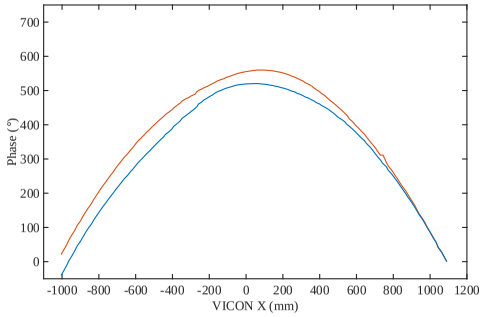

(d) $3.5GHz$

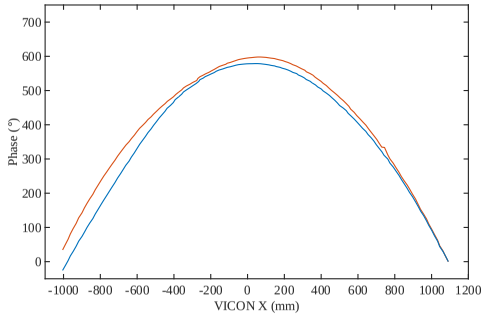

(e) $4.0GHz$

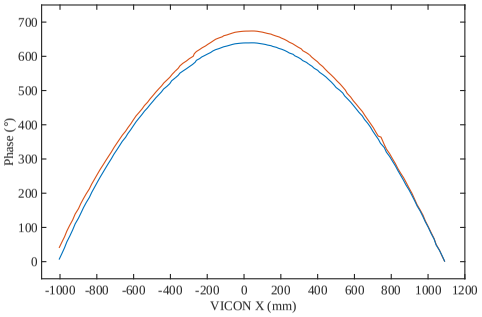

(f) $4.5GHz$

Figure 27. One-Way Probe Horizontal Phase Measurement: The phase front representation measured by a horizontal scan of the test volume at -19 for $2.0 - 4.5Ghz$.

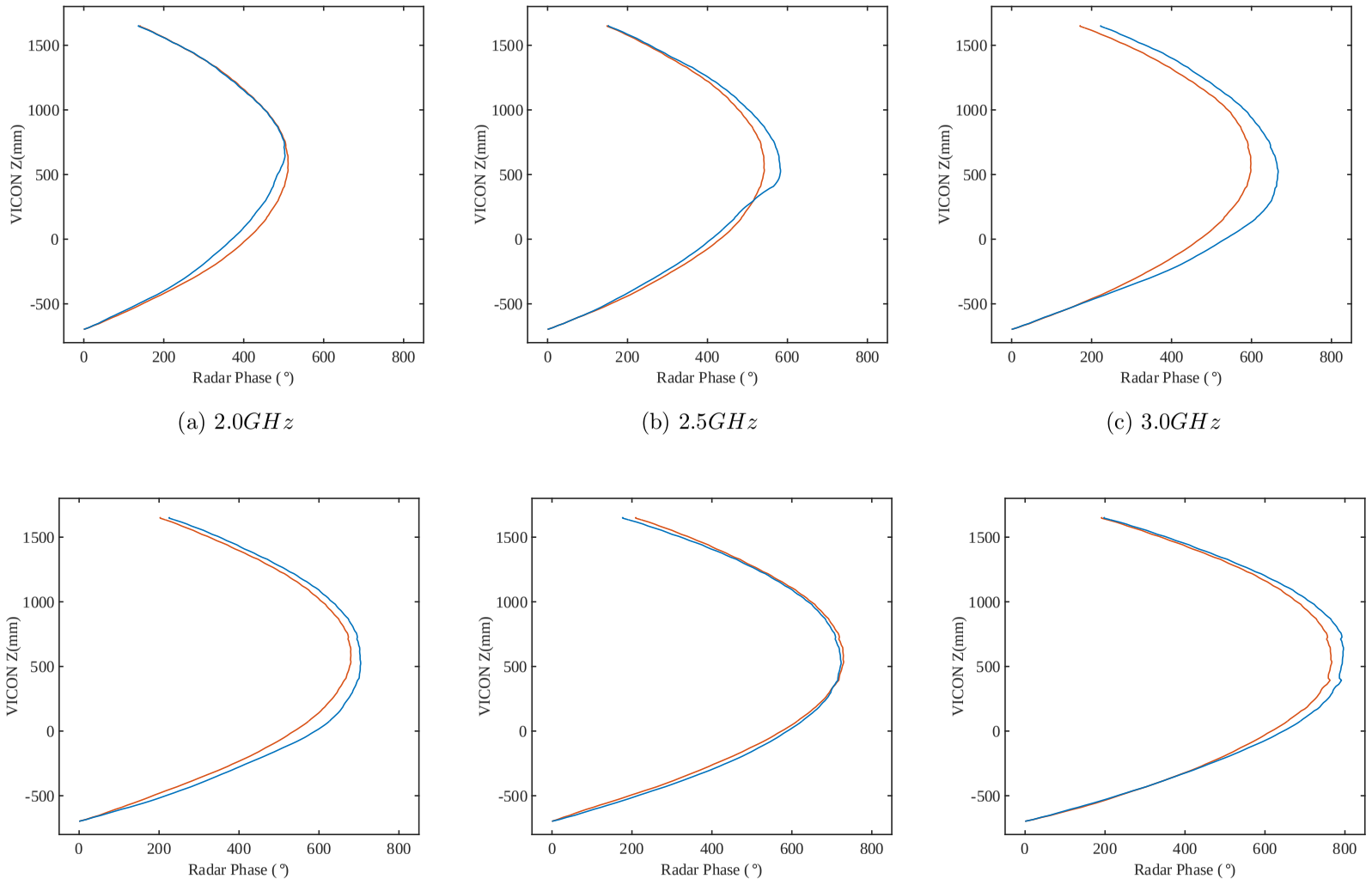

(a) $2.0GHz$ (b) $2.5GHz$ (c) $3.0GHz$

(d) $3.5GHz$ (e) $4.0GHz$ (f) $4.5GHz$

Figure 28. One-Way Probe Vertical Phase Measurement: The phase front representation measured by a vertical scan at the center of the test volume for $2.0 - 4.5Ghz$.

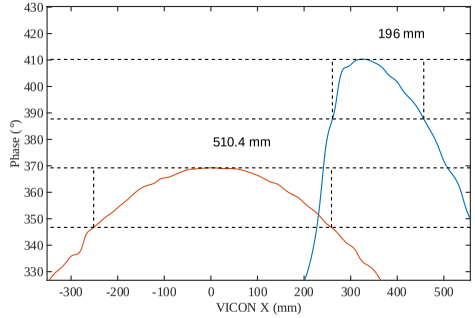

(a) $2.0GHz$

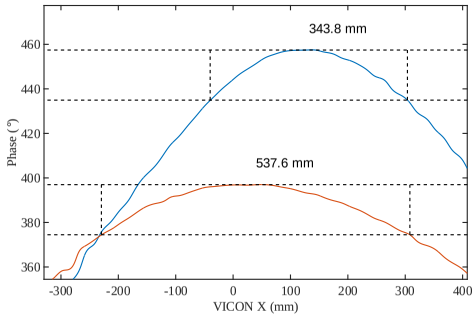

(b) $2.5GHz$

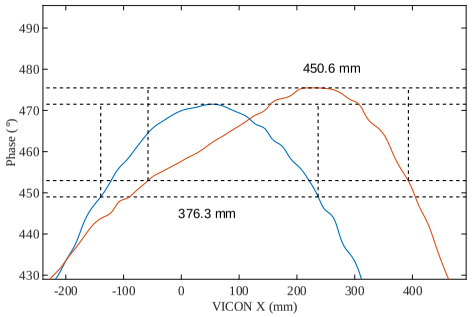

(c) $3.0GHz$

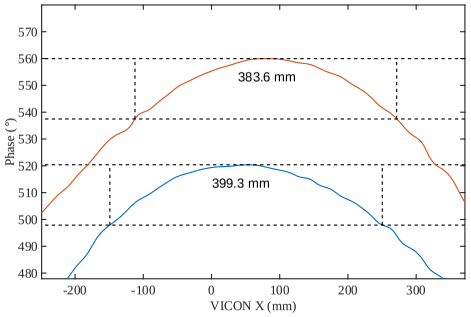

(d) $3.5GHz$

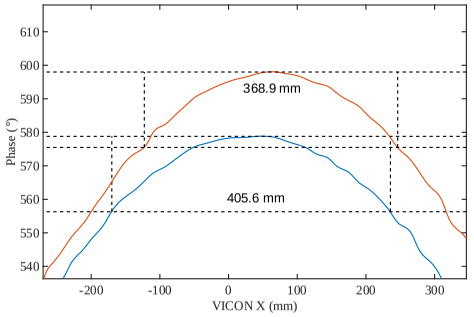

(e) $4.0GHz$

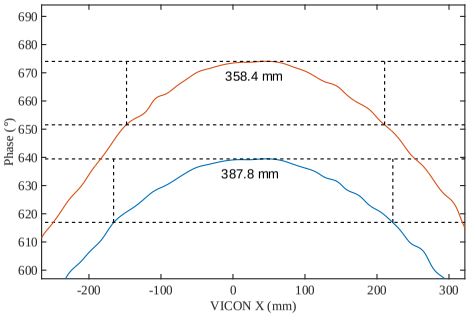

(f) $4.5GHz$

Figure 29. Horizontal Quiet Zone: Each $22.5°$ quiet zone was calculated for the -19 horizontal sweep. Shown are the $2.0 - 4.5Ghz$ frequency measurements.

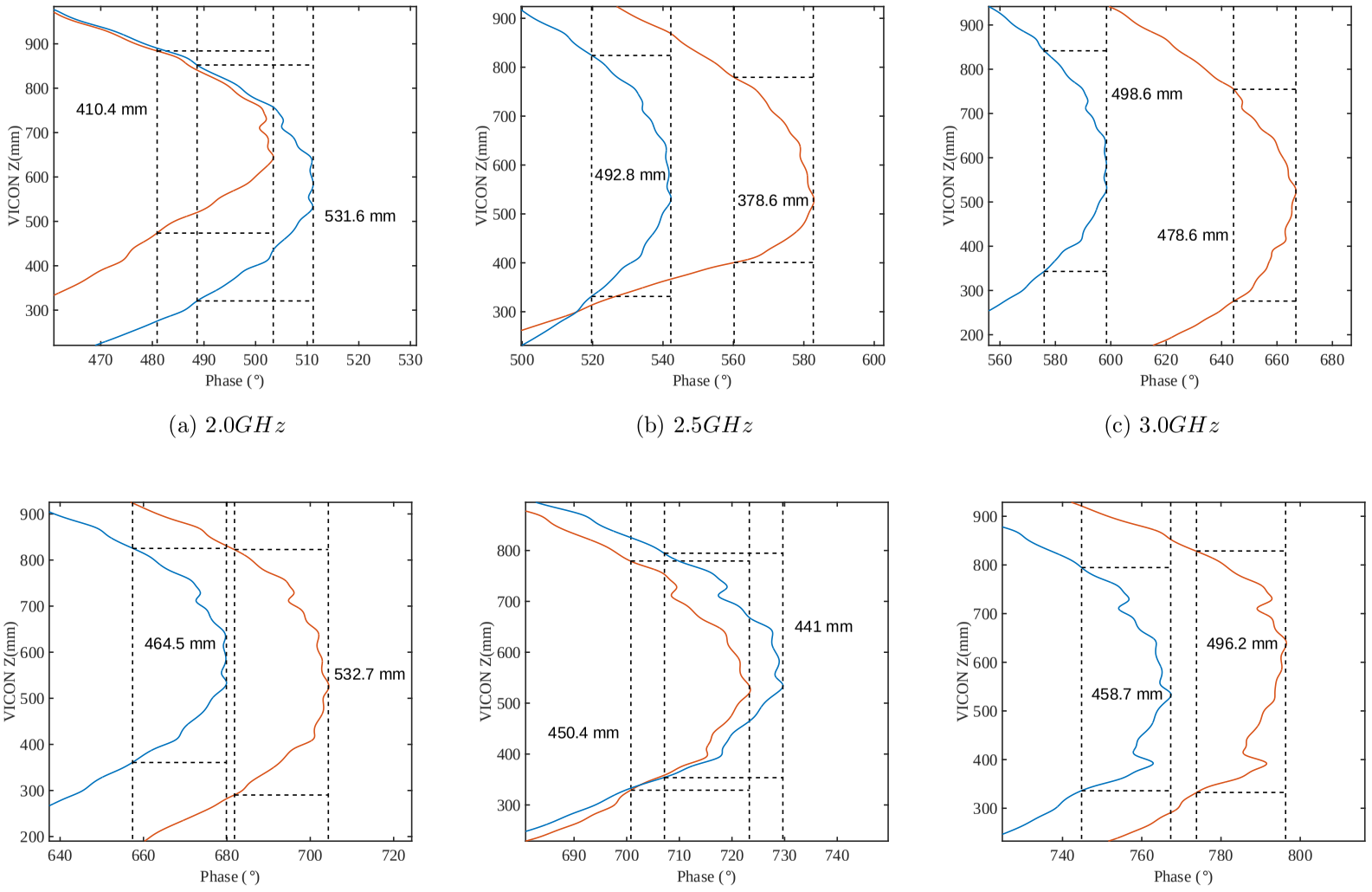

(a) $2.0GHz$ (b) $2.5GHz$ (c) $3.0GHz$

(d) $3.5GHz$ (e) $4.0GHz$ (f) $4.5GHz$

Figure 30. Vertical Quiet Zone: Each 22.5° quiet zone was calculated for the vertical sweep. Shown are the $2.0 - 4.5Ghz$ frequency measurements.

4.3 Two Way Probe Expectation

Upon setting a one-way probe baseline, the next phase was to understand the two-way probe capability of the system integrated with the Vicon™ motion capture system. In this step, an object with a known phase response and the geodesic sphere were translated through the test chamber. It's phase measurements and Vicon™ position data were captured and compared. The 375 calibration cylinder (3.75 *in* radius) with known phase response was used as the two-way probe baseline. The result of the physical translation in and out of the phase front was expected to match the recorded radar phase measurement. The 375 calibration cylinder should not require any phase subtraction based on pose. However, by performing pose dependent phase subtraction on the sphere's measurement, the translational path should be recreated.

To define the 375 calibration cylinder as an object in the Vicon™ software, reflective tape was placed asymmetrically on the cylinder illustrated in Figure 31. The 375 calibration cylinder's object centroid in the x, y, and z-axis, was visually aligned in the Vicon™ Tracker software using the center square of reflective tape. It was assumed that the reflective tape had little to no affect on the 375 cylinder's phase response.

After performing calibration measurements using 750 and 900 calibration cylinders, two radar measurements were conducted with the cylinder as the target. For the first measurement, the 375 cylinder was centered on the foam column (Figure reffig:TwoCylCen) and measured from 0 ° to 360 ° in 0.25 ° increments. The target was stationary at each position increment when illuminated by the radar. The 375 cylinder was then placed off center (Figure 32b) of the foam column and the measurement was repeated. The same procedures were performed using the geodesic sphere as the measurement target illustrated in Figures 32c and 32d. The

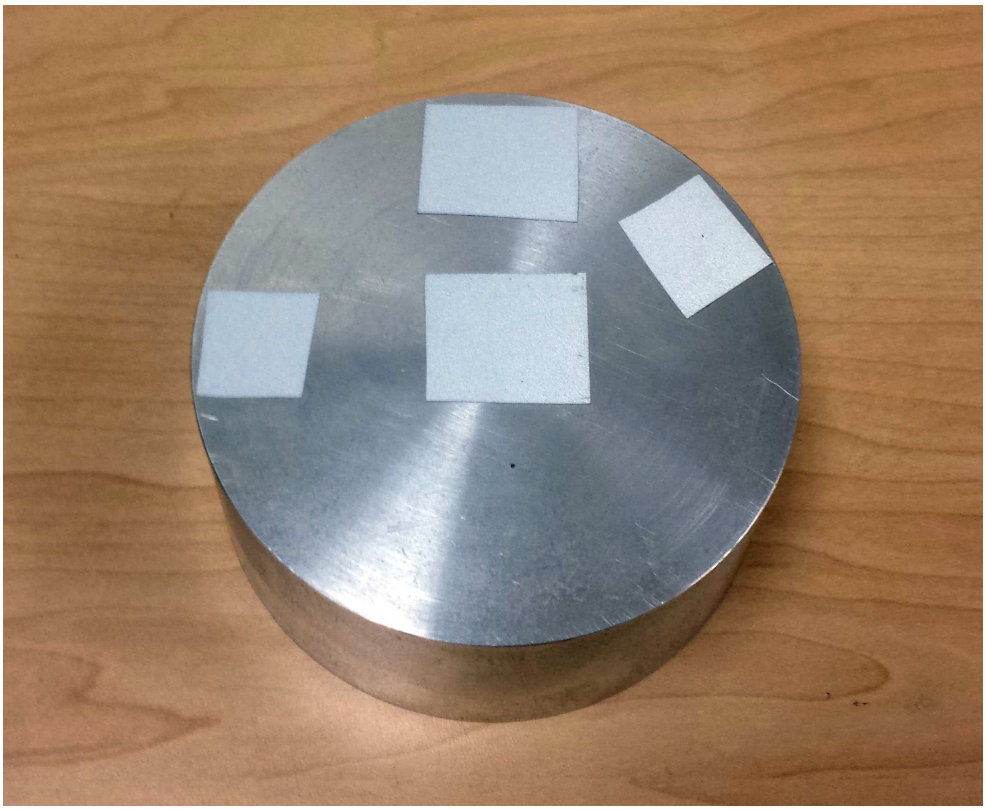

Figure 31. 375 Calibration Cylinder: Reflective tape attached to 375 calibration cylinder to capture object motion in Vicon™ software.

sphere was oriented with 1.11 ° and 1.26 ° pitch and −1.52 ° and −0.950 ° roll for the centered and off centered measurements respectively. To minimize any residual effects induced by differences in height, the 375 cylinder was placed on additional foam spacers to raise its center to the same height as the center of the geodesic sphere. The average height measurements for the 375 cylinder and sphere were 320 mm ± 0.73 and 300 mm ± 1.1 respectively. For both the 375 cylinder and the geodesic sphere, each radar measurement was begun at the 0 ° yaw position ±0.02 °. Also, every attempt was made to place the target in the same y-axis location for the off centered measurement as it was in the centered measurement. The physical representations of the paths traveled in the four measurements is illustrated in Figure 33.

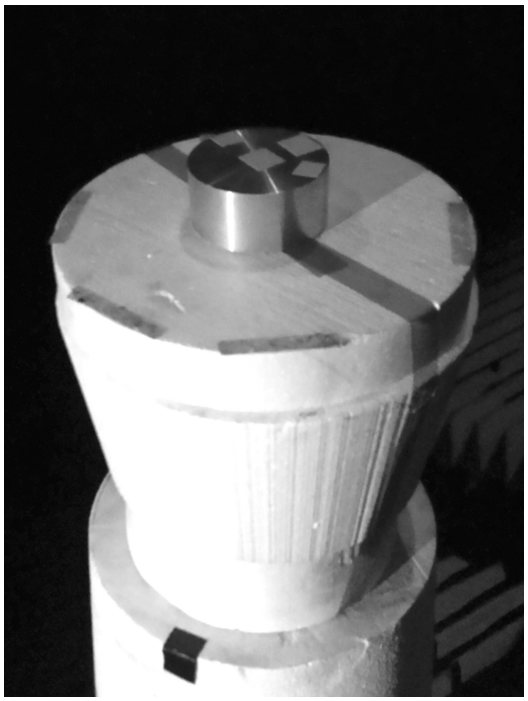

(a) Centered 375 Cylindar

(b) Offcenter 375 Cylindar

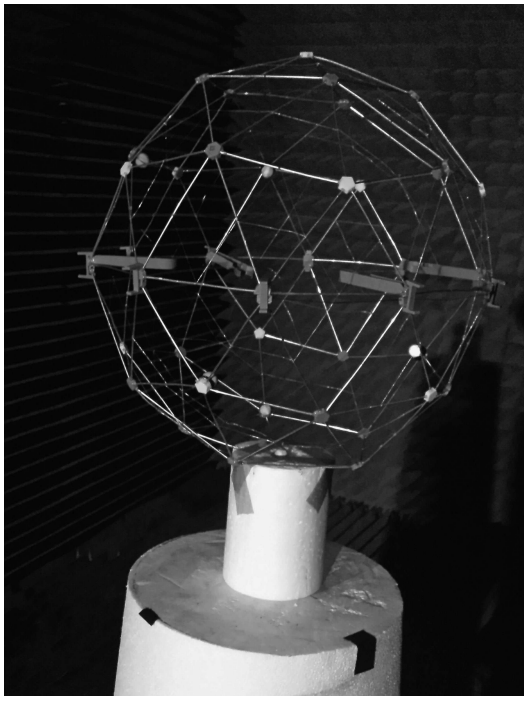

(c) Centered Sphere

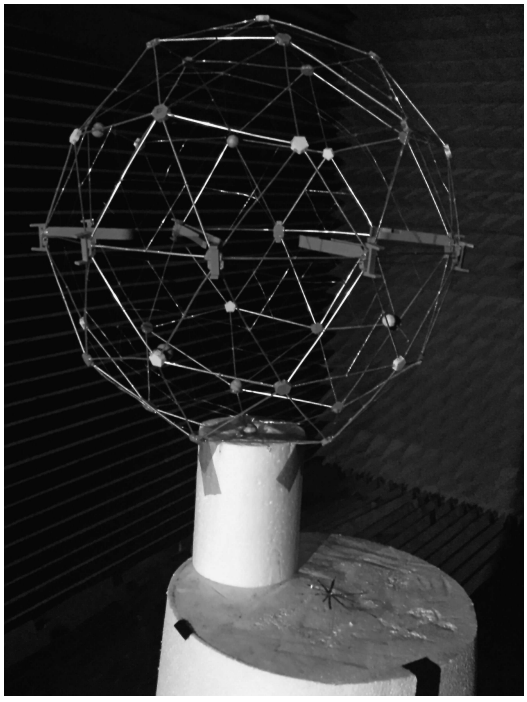

(d) Offcentered Sphere pp

Figure 32. Two Way Probe verification placement: To verify the two way probe capability a 375 calibration cylinder and the geodesic sphere were placed in the center of the foam column and off center of the foam column then rotated 360°.

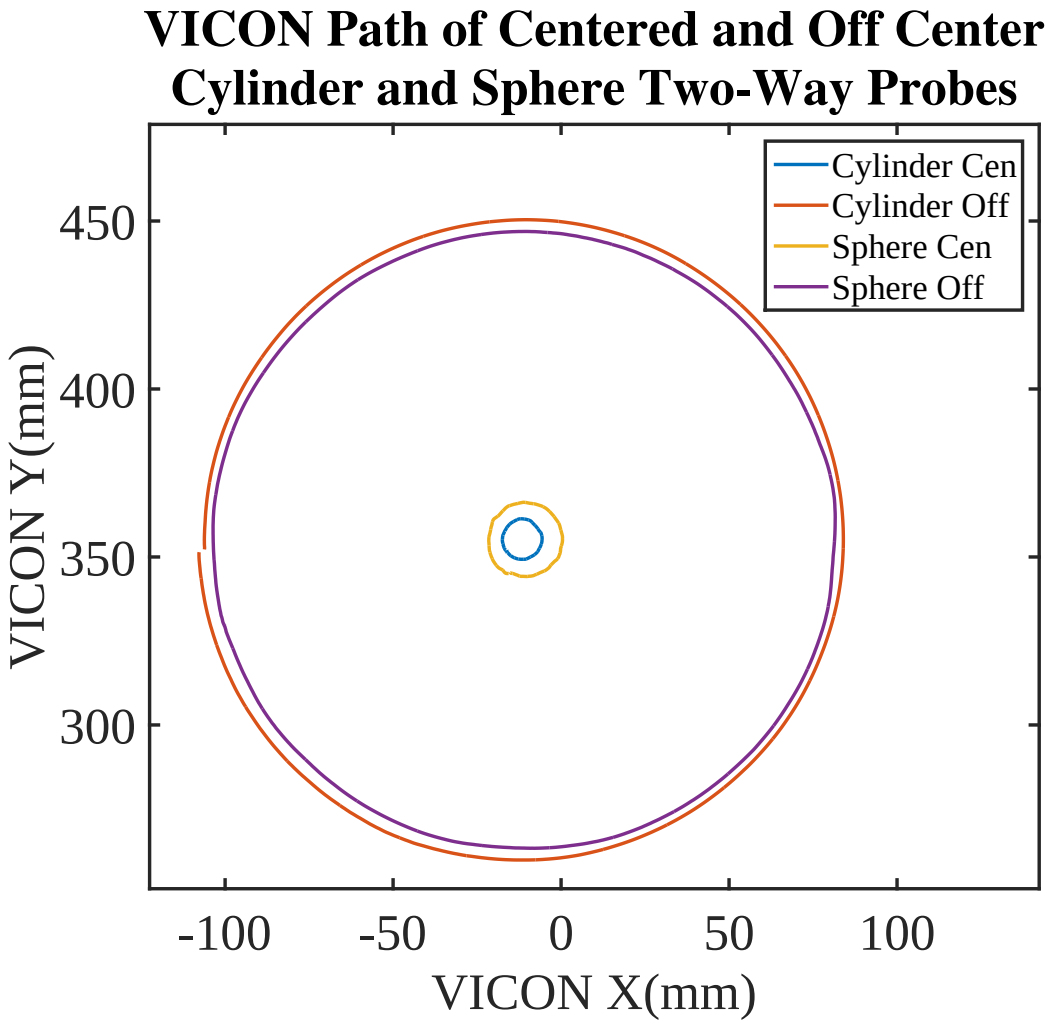

Figure 33. 375 Cal Cyl/Sphere Path: The physical rotational path captured from Vicon™ of the 375 calibration cylinder and Geodesic sphere centered and off center of foam column.

To aid in post processing analysis, the target object's Vicon™ defined centroid position and pose was recorded with the position of one outer marker used to define the object illustrated in Figure 34. The path of the object's centroid and outer marker determined accuracy of placement on the foam column and accuracy of the centroid's defined location. The solid blue and purple line represents the objects centroid path for the 375 cylinder and sphere respectively. It was apparent that the cylinder and sphere were not perfectly centered. The solid green path represents a reflective marker used to define it's respective Vicon™ object. The dashed lines

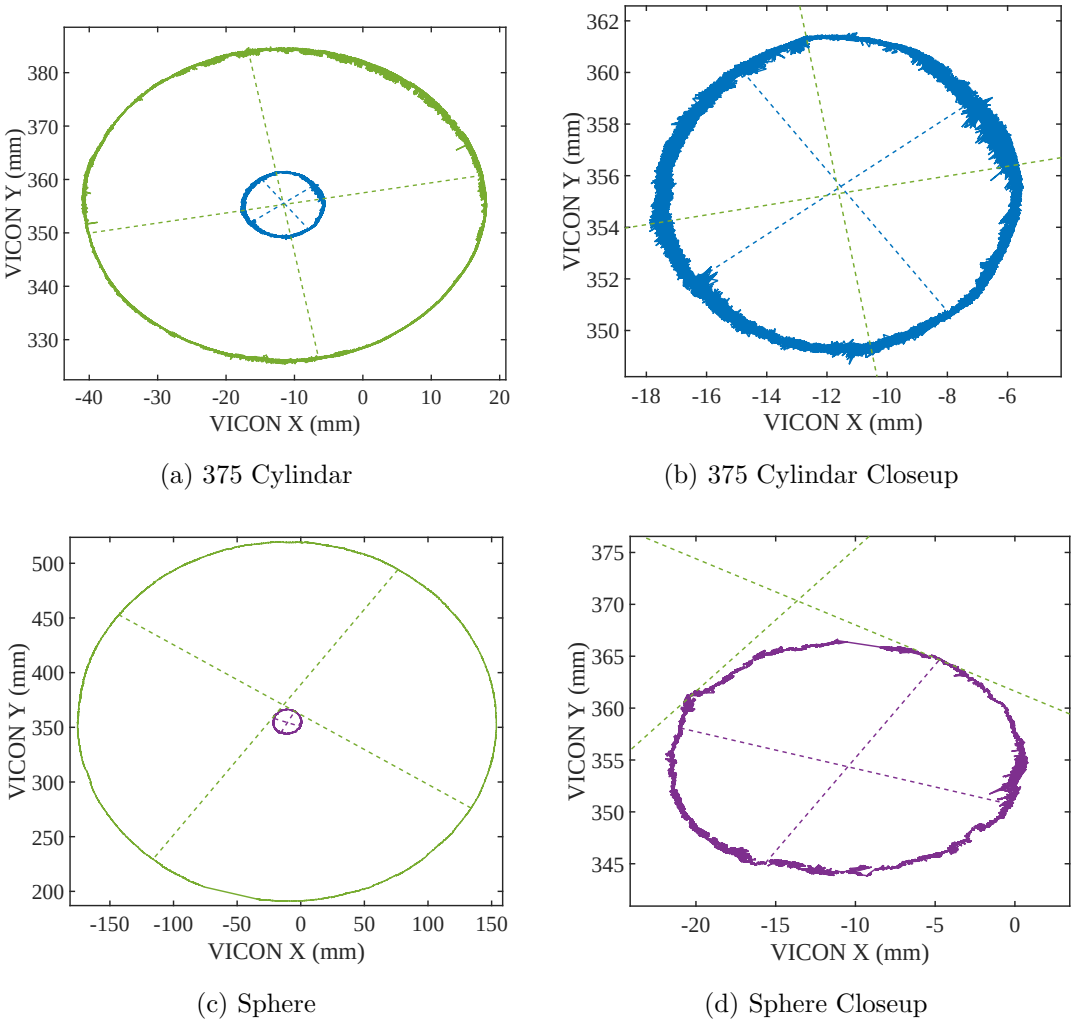

(a) 375 Cylindar

(b) 375 Cylindar Closeup

(c) Sphere

(d) Sphere Closeup

Figure 34. Two Way Points of Rotation: The offset between each objects center of rotation indicates the error in the object centroid defined in Vicon™ Tracker.

represent two crosswise chord lines for each object's circular path. The intersection of the dashed lines indicate the point of rotation for that object. As a representation of a truly physical object, the center of rotation for the outer marker was the true center of rotation for the foam column. The difference in outer marker and object centroid rotation centers was a combination of how accurate the centroid was defined in the Vicon™ space, how level the object was during the test, and the accuracy of the Vicon™ origin definition. In the case of the 375 cylinder, the centroid's rotation center was within 1 mm of true. The sphere's centroid rotation center was within 15 mm.

Improperly defining the object centroid location could impact calibration measurements of the sphere's scattering characteristics. At a minimum the object centroid offset should be compensated for when recording each sphere's scattering characteristics. This research did not determine the effects of an ill-defined Vicon™ origin, centroid misalignment, or deviations in object pose during it's calibration process. The potential impacts of the three aforementioned topics will be discussed in the uncertainty section later in this chapter.

4.4 Cylinder/Sphere Two-Way Probe Results and Analysis

After applying the calibration measurements taken previously, each objects translation in the Vicon™ y-axis was converted to a phase translation by using the unwrap command in MATLAB®. After which, a visual comparison concluded the process to be effective. Comparisons were them made between the physical phase translations and radar phase measurements. As expected, a translation of the 375 cylinder in physical space directly related to a translation of the radar phase measurement as shown in Figure 35. There were minor frequency dependent differences between the Vicon™ and radar phase measurements. These differences may be

caused by the 375 cylinder not being level, noise recorded in the radar measurement, and/or the effects of the reflective tape on RCS measurements.

A similar comparison was performed using the captured data of the sphere, however, it was accomplished by a two step process. Initially the calibrated raw radar phase measurement for the centered and off centered sphere were compared to the respective path. This comparison of the raw phase to Vicon™ phase was considered an uncompensated measurement. The results of the uncompensated phase measurements are depicted in Figures 36a, 37a, 38a, and 39a. The final analysis performed on the off centered sphere measurement was done by subtracting the yaw dependent phase measurement of the sphere. By having measured the phase characteristics of the sphere at each yaw position, the phase subtraction was completed by using Equation 17:

$$e^{(jP_{co}(\theta))} = \frac{e^{(jP_{uo}(\theta))}}{e^{(jP_{uc}(\theta))}} \tag{17}$$

In Equation 17, P_{co} is the compensated phase value of the off centered target, P_{uc} and P_{uo} are the uncompensated phase measurement of the centered and off centered target respectively, and θ is the observed body aspect angle of the target. After performing the subtraction, the phase measurements were unwrapped. Figures 36b, 37b, 38b, and 39b show the compensated measured phase compared to the calculated phase translation measured using Vicon™. In general, the compensated phase values matched the target's physical path through the phase space.

There were instances of anomalies in the compensated phase values like that seen in Figures 37b and 38b for the vertical polarizations of the 3.4 GHz and 3.9 GHz measurements. It was believed that one or two instances of ambient noise in the test chamber causeed deviations in the measurement that were not recoverable

when unwrapping in post processing. However, in the example of the 2.9 GHz horizontal polarization measurement the signal at that frequency contained too much distortion to recover a viable compensated phase value. It was unknown if the excess ambient noise was encountered during the centered measurement, off centered measurement, or both. Three dimensional representations of the measured phase as it related to frequency and aspect angle for the off centered 375 cylinder and sphere are illustrated in Figure 40. System noise was apparent in the lower frequencies for the 375 cylinder measurement, which was an unfortunate characteristic of the radar used. Deviations in the $5GHz$ horizontal polarization seen in Figure 39b may be caused by improper alignment for the phase subtraction. The errors observed in roll, pitch, and yaw between the two measurements of the sphere are listed in Table 2.

Table 2. Two-Way Measurements Pose Error: Average Error Between Pose Measurements of Centered/Off Centered Sphere

Measurement	Δ
roll	$0.175^\circ \pm 0.08$
pitch	$-0.572^\circ \pm 0.26$
yaw	$-0.142^\circ \pm 0.13$

Because there was only one measurement accomplished with the sphere centered, it was unclear what impact differences in pose had on the compensation calculation.

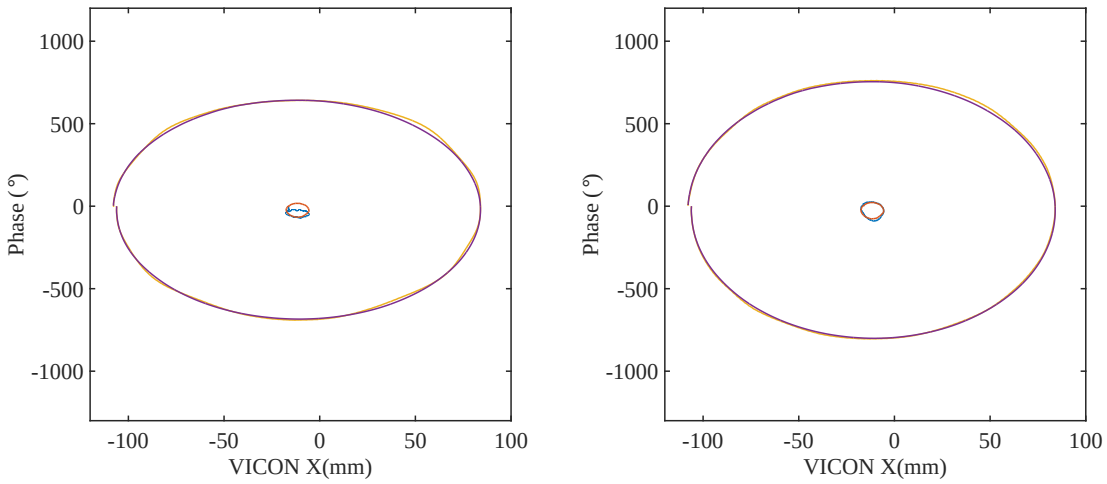

(a) $2.9GHz$ pp

(b) $3.4GHz$ tt

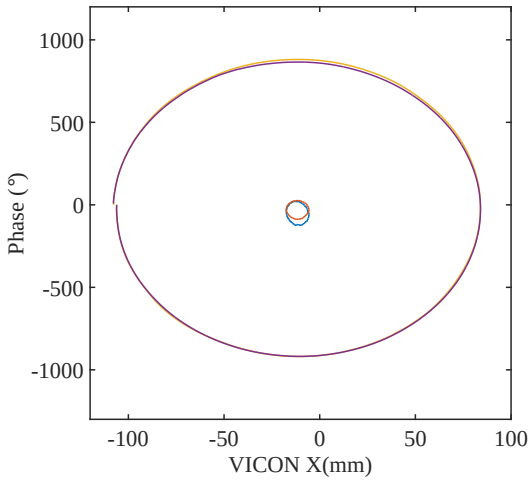

(c) $3.9GHz$ tt

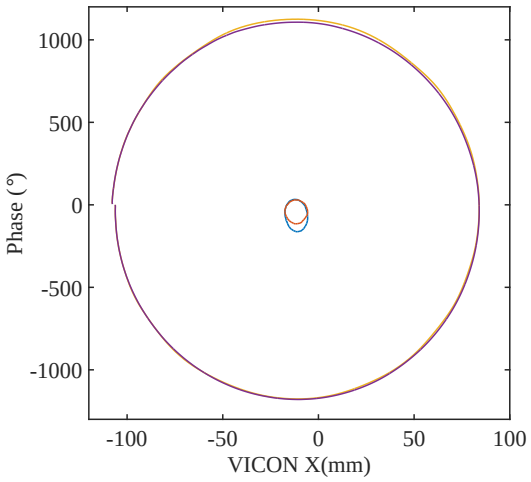

(d) $5GHz$ pp

Figure 35. Two Way Probe Verification of 375 Cylinder: The measured phase of 375 calibration cylinder compared to the phase as recorded in Vicon™ space while rotated on a foam column.

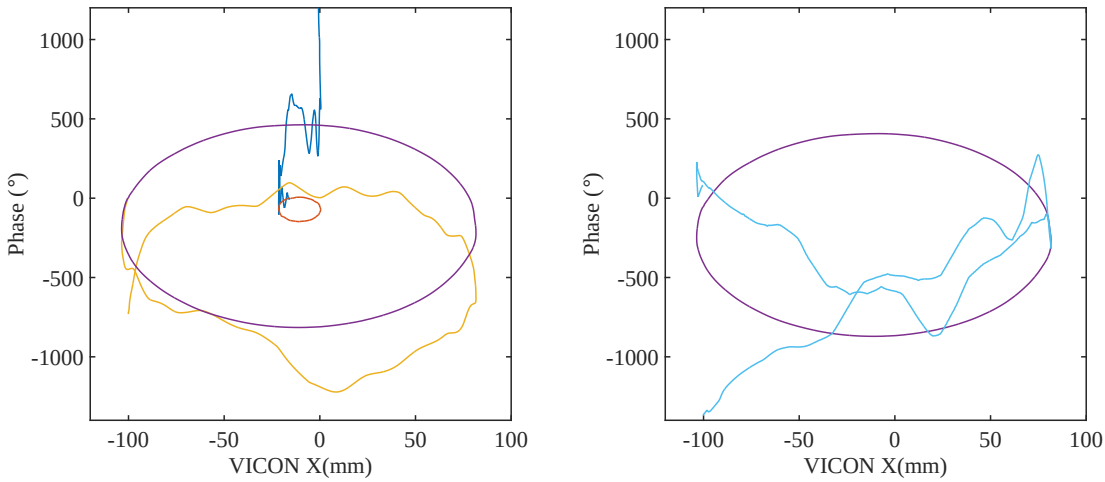

(a) 2.9Ghz Uncompensated

(b) 2.9Ghz Compensated

Figure 36. Two Way Probe Verification of Sphere 2.9Ghz**: Phase representation of 375 calibration cylinder and geodesic sphere rotated off center of foam column.**

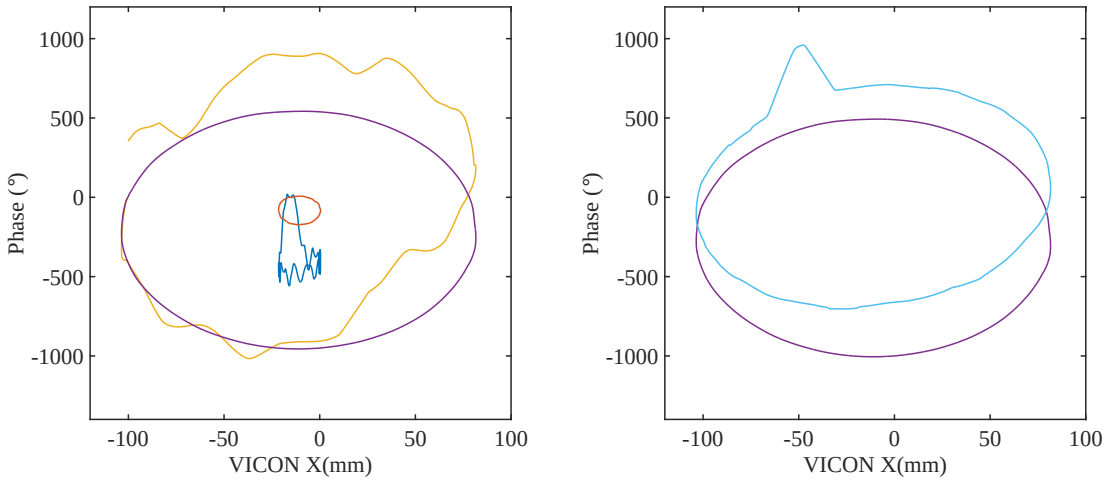

(a) 3.4GHz Uncompensated

(b) 3.4GHz Compensated

Figure 37. Two Way Probe Verification of Sphere 3.4Ghz**: Phase representation of 375 calibration cylinder and geodesic sphere rotated off center of foam column.**

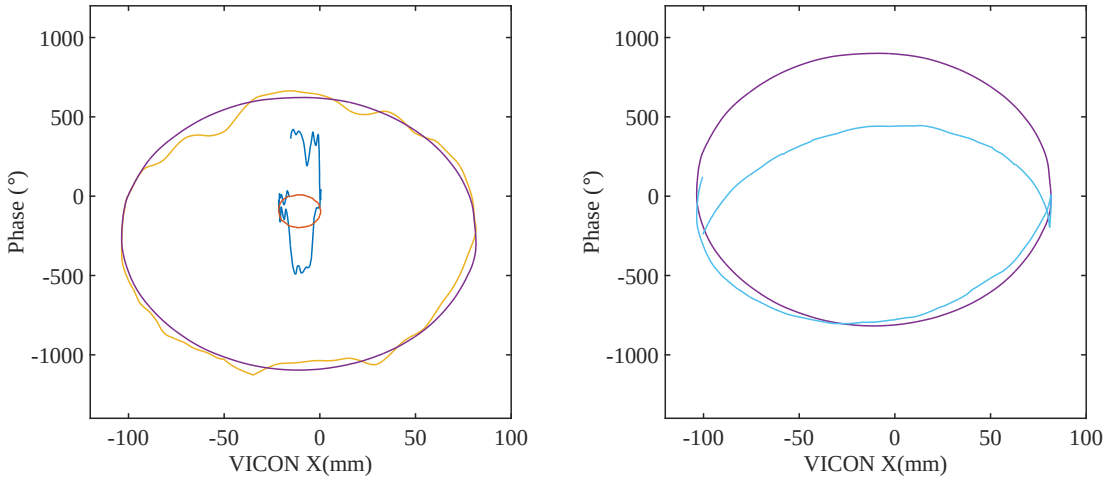

(a) 3.9Ghz Uncompensated

(b) 3.9Ghz Compensated

Figure 38. Two Way Probe Verification of Sphere 3.9Ghz**: Phase representation of 375 calibration cylinder and geodesic sphere rotated off center of foam column.**

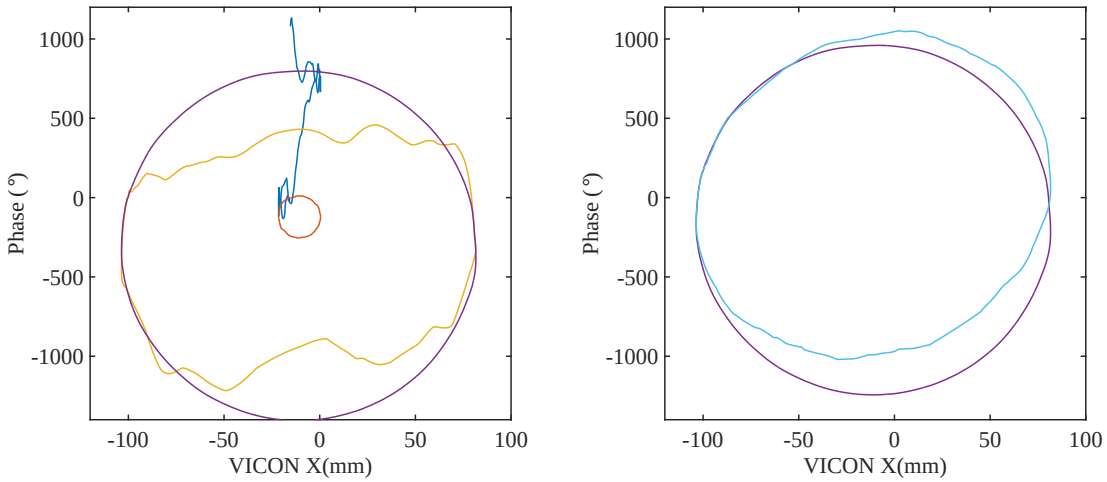

(a) 5GHz Uncompensated

(b) 5GHz Compensated

Figure 39. Two Way Probe Verification of Sphere 5GHz **: Comparison between calculated Vicon™, uncompensated, and compensated phase of the sphere while rotated on a foam column.**

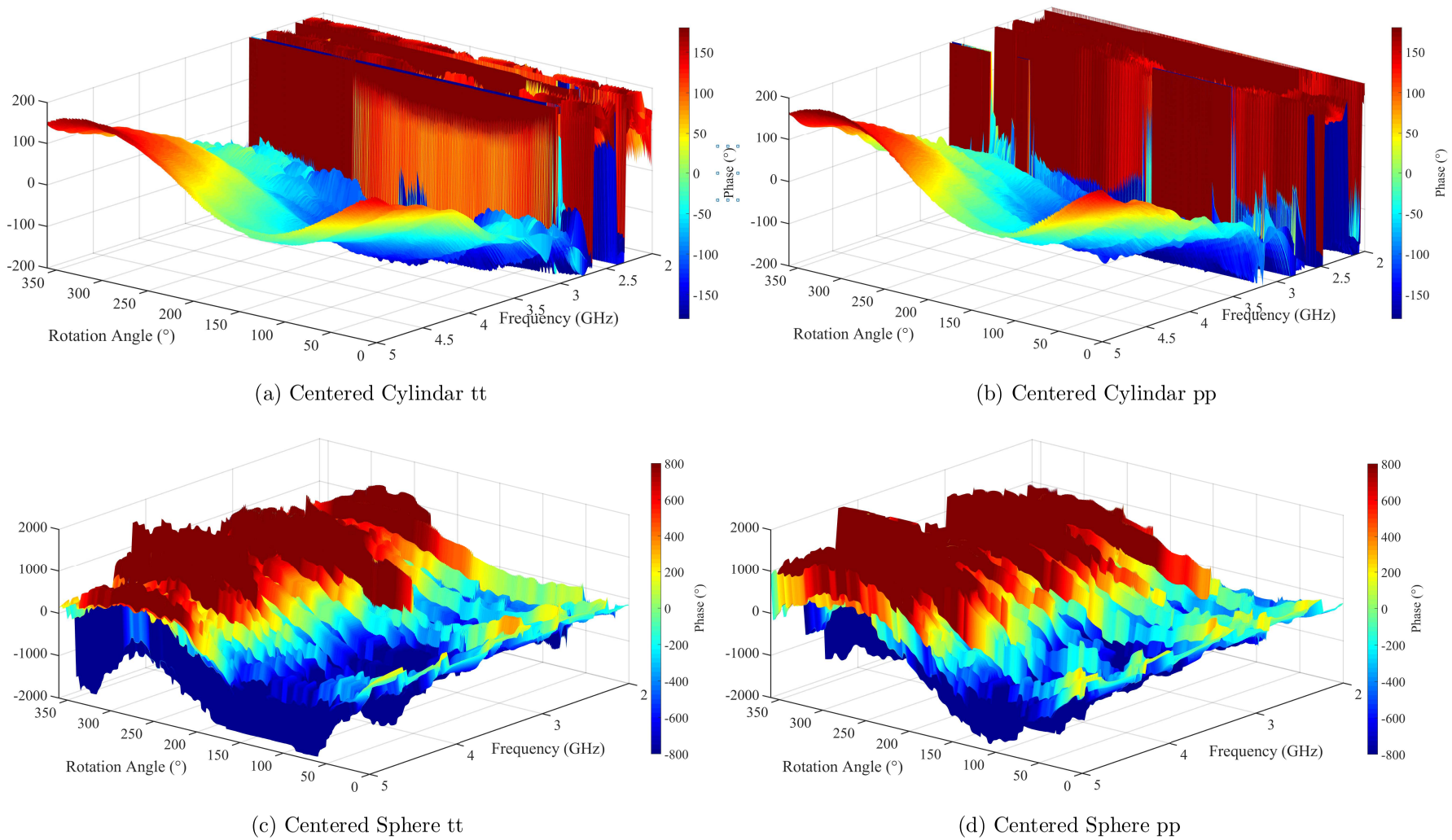

(a) Centered Cylindar tt

(b) Centered Cylindar pp

(c) Centered Sphere tt

(d) Centered Sphere pp

Figure 40. Two Way Probe verification: Phase representation of 375 calibration cylinder and geodesic sphere rotated off center of foam column.

As a result of performing a start and stop two way probe measurement with a known target, it was confirmed the system was capable of perming the procedure. Furthermore, by performing the same process with the geodesic sphere, it was concluded the geodesic sphere was viable to be used as a two-way probe. Additional analysis of the results will need to be accomplished quantify errors found in the measurements as well as areas for improvement. By undergoing the two way probe verification process, important focus areas were uncovered and will be addressed in Chapter V.

4.5 Expectation from Quad

The final stage in this research project was to capture phase measurements within an RCS test volume using a geodesic sphere. Given the results found in stage two, the expectation going into stage three was to see similar degradation in phase response but maintaining a distinguishable path through phase space. Controlled by the program defined in Chapter III, a Parrot Bebop quadcopter was encased by a geodesic sphere then flown through the test volume. There were three primary flight patterns available: Raster Scan in the XZ Plane, XY Slanted Raster Scan, and Helical Scan. This research will focus on the XZ raster scan and XY slanted raster scan. Figure 41 shows the geodesic sphere encased quadcopter flying an XZ raster scan pattern at AFIT's RCS lab. The flight measurement data collected of sphere encased Quad-copter was submitted to Captain Dossett for position and pose compensation and field characteristics deconstruction.

Prior to the first flight, phase response measurements of the quadcopter with sphere at different pitch values listed in Table 3 were made. Captain Dossett used the pitch and yaw data along with the corresponding RCS measurements to cre-

ate a data mesh of the geodesic sphere. This mesh represented the expected phase value for each pitch and yaw during a flight test measurement.

Table 3. Quadcopter and Geodesic Sphere measurements: Quadcopter w/ Geodesic Sphere Phase response over yaw and pitch

Pitch (deg)	Azimuth (deg)	Pol	Freq(GHz)
5	$-20 : 0.5 : 20$	HH/VV	$2 : 0.05 : 18$
4	$-20 : 0.5 : 20$	HH/VV	$2 : 0.05 : 18$
3	$-20 : 0.5 : 20$	HH/VV	$2 : 0.05 : 18$
2	$-20 : 0.5 : 20$	HH/VV	$2 : 0.05 : 18$
1	$-20 : 0.5 : 20$	HH/VV	$2 : 0.05 : 18$
0	$-20 : 0.5 : 20$	HH/VV	$2 : 0.05 : 18$
-1	$-20 : 0.5 : 20$	HH/VV	$2 : 0.05 : 18$
-2	$-20 : 0.5 : 20$	HH/VV	$2 : 0.05 : 18$
-3	$-20 : 0.5 : 20$	HH/VV	$2 : 0.05 : 18$
-4	$-20 : 0.5 : 20$	HH/VV	$2 : 0.05 : 18$
-5	$-20 : 0.5 : 20$	HH/VV	$2 : 0.05 : 18$

Four successful flights with captured RCS data were accomplished. A list of the flight path type, x-y start and end points, altitude positions, and frequencies describing the successful flights are provided in Table 4. A three dimensional visualization of an XZ raster scan flight and XY slant scan flight are illustrated in Figures 43 and 44. Each flight iteration provided more insight to the capabilities and limitations of the integrated radar and flight control system. In the first two flights, data from three frequencies at one polarization were collected to reduce the scan time to $\approx 0.8\ s$ between frequency sweeps. Between the first two flights the frequency band was changed to a band with greater signal to noise ratio (SNR).

It was determined that including both polarizations and increasing the frequency sweep to $2 : 0.1 : 5\ GHz$ increased the frequency sweep time to $\approx 0.9\ s$.

Table 4. Flight Parameters: Flight Profile, Position Inputs, Speed, and Radar Parameters for Quad w/ Sphere (Q/S) and Quad Only (Q).

Flight Path	$(x_s : x_e, y_s : y_e)(mm)$	Altitude (mm)	Freq(GHz)	Pol
XZ Raster Q/S	$(-1000 : 1000, 360 : 360)$	$757, 300, -157$	$2.1 : 1.0 : 4.1$	V
XZ Raster Q/S	$(-1000 : 1000, 360 : 360)$	$757, 300, -157$	$3.5 : 0.5 : 4.5$	V
XZ Slant Q/S	$(-1000 : 1000, 1400 : -800)$	$1100 : -200 : 100$	$2 : 0.1 : 5$	H/V
XY Slant Q	$(1090 : -1008, 52 : 784)$	500	$2 : 0.1 : 5$	H/V
XY Slant Q/S	$(1090 : -1008, 52 : 784)$	500	$2 : 0.1 : 5$	H/V

4.6 Results of Quad/Sphere Probe

When analyzing the first two flights, it became apparent there was an under sampling problem. Flight time was limited to battery endurance with an average maximum flight duration of 220 s. To achieve scans with multiple altitudes, the translation velocity was 100 mm/s. As a result, each pass in the scan was limited to $13 - 21$ data points. For the first XZ raster scan flight, 15 data points were collected over a 1100 mm translation in x at a constant y. Given the phase front's characteristic through a perpendicular scan, at 3.5 GHz,the phase transitioned through six 2π iterations as shown in Figure 42. Further testing with an increased sample space was required to make a qualitative conclusion of the system's effectiveness.

Due to limited time and material availability, a single geodesic sphere was constructed. Unfortunately, the sphere to quadcopter attachment point design intermittently interfered with flight stability, causing the quadcopter and sphere to crash. Additionally, it was determined that two batteries failed to hold charge during a

Figure 41. Flying Sphere Encased Quad-Copter: Demonstrated flight capability of a flying Quad-Copter encased in a geodesic sphere with captured radar data.

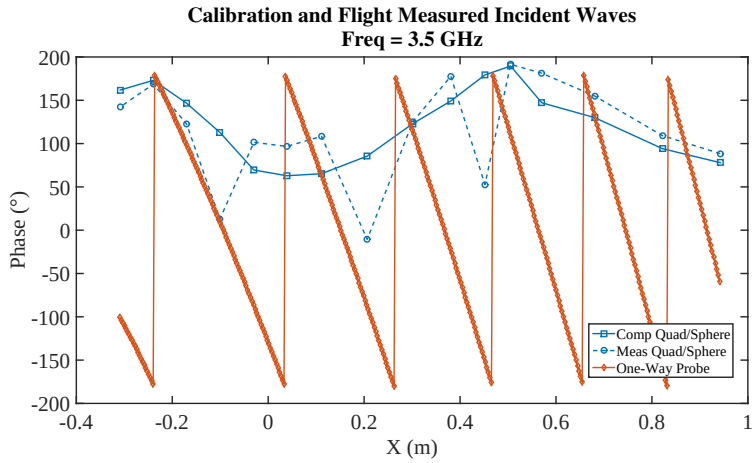

Figure 42. Phase Comparison of XZ Raster Scan Flight: Under sampling of the sphere encased Quad-Copter is believed to limit determination of phase front characteristics.

flight causing the quadcopter to enter an emergency shutdown state. After a crash, the measurements from Table 3 would need to be re-accomplished; evident in the before and after phase difference seen in Figure 45.

To truly provide correlations in the one-way probe measurements and the geodesic sphere two-way probe, data sampling was improved and the quadcopter was flown along a flight path similar to the -19 ° measurement described earlier. The z position was set at 500 mm. Due to the battery life flight time limitation the data sam-

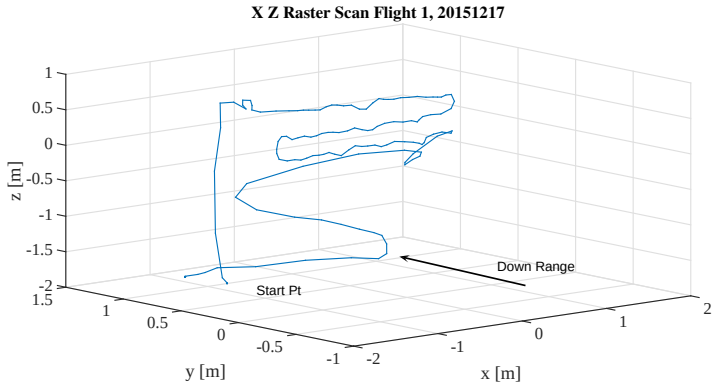

Figure 43. XZ Plane Raster Scan Flight: Initial flight path of a Sphere encased Quad-Copter at three stepped down altitiudes of 750**,** 300**, and** $-150mm$ **at a rate of** $100mm/s$ **in the XZ plane at** $Y = 360mm$**.**

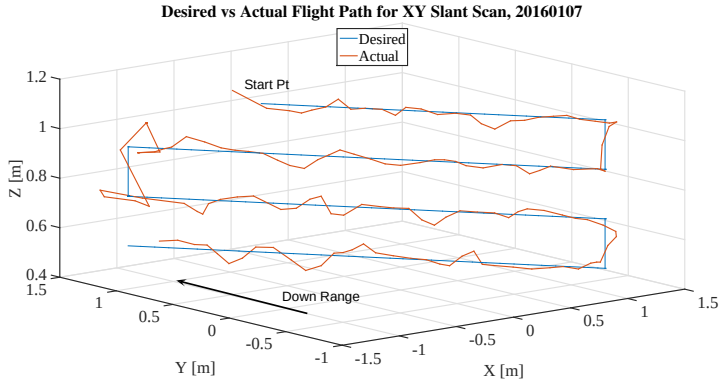

Figure 44. XZ Slanted Raster Scan Flight: Slanted flight path of a Sphere encased Quad-Copter at four stepped down altitiudes of 1100**,** 900**,** 700**, and** $500mm$ **at a rate of** $100mm/s$ **XY path endpoints of** $(-1000, 1400)$ **and** $(1000, 800)$**.**

pling was improved by reducing the flight translation velocity to 9 mm/s. Increased battery life may further improve data sampling.

A -19 ° flight profile was accomplished with the geodesic sphere. However, before performing re-calibration measurements of the sphere, the quadcopter entered an unstable state, and sustained irreparable impact damage to the sphere shown in Figure 46. Further analysis of the 500 mm, -19 ° XY slant scan flight data may provide similar results seen in the uncompensated sphere measurements explained earlier. Although not ideal, a 500 mm, -19 ° XY slant scan flight measurement of the quadcopter without a sphere was conducted.

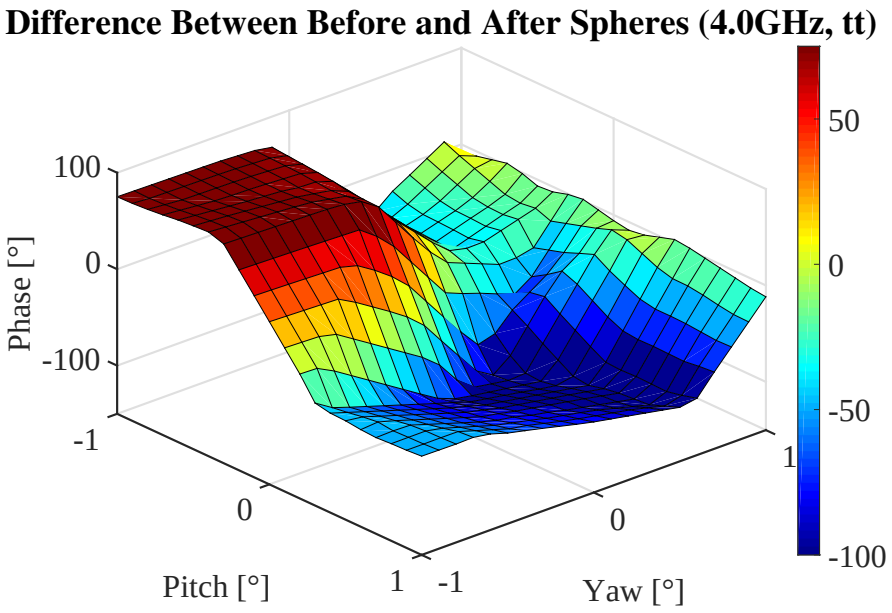

(a)

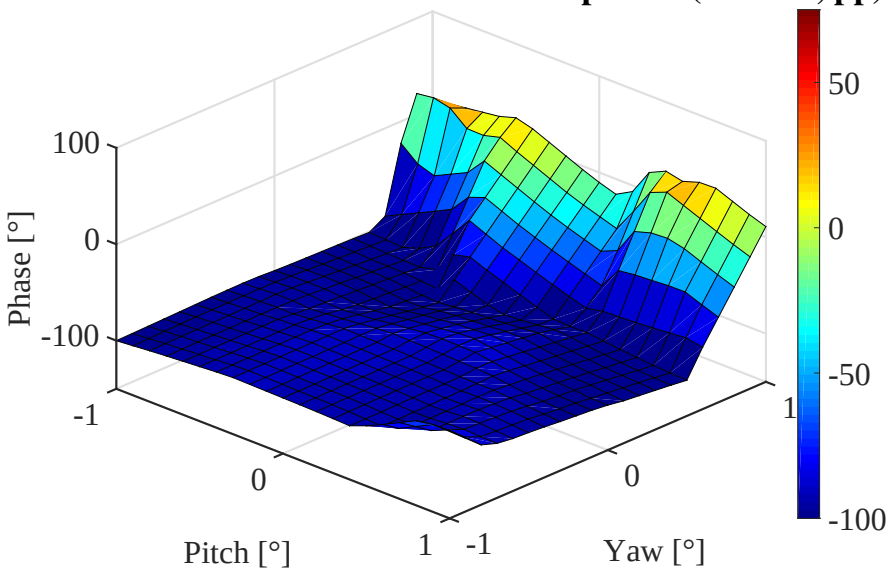

(b)

Figure 45. Sphere Before/After Crash Phase Difference TT: Observable differences in calibrated measurements after the sphere sustained impact damage.

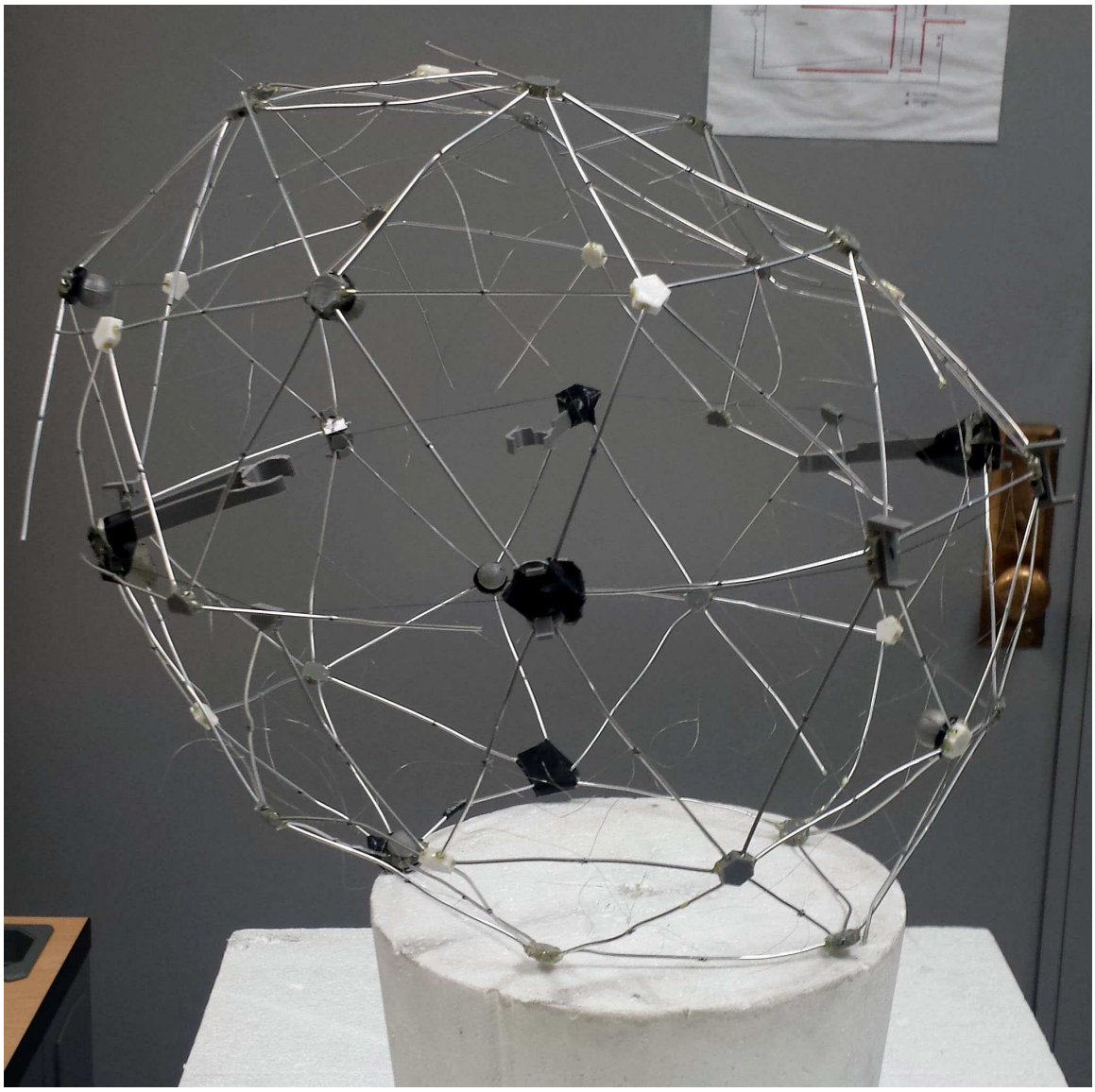

Figure 46. Damaged Sphere: Aftermath of catastrophic crashed caused by platform instability.

By using the quadcopter by itself as a two-way probe, the phase characteristics of different pose orientations was required. Because of time limitations, two pose orientation measurements were accomplished. First, the quadcopter was placed level at 0.47 ° ± 0.05 of pitch, shown in Figure 47a on the foam column and rotated in yaw from −5 ° to 5 ° in 0.25 ° increments. The quadcopter was then placed on its side with 90 ° ± 2 of roll. It was then rotated in pitch from −10 ° to 10 ° in 0.25 ° increments. The two measurements were linearly interpolated and normalized to represent a phase difference given a specified pitch and yaw. Finally, the two difference factors were crosswise added to develop a crude yaw and pitch angle dependent lookup matrix. The impact frequency had on the phase for yaw and pitch is illustrated in Figures 48 - 51. It was readily apparent that certain frequencies have visibly smoother differences in phase over each pose orientation.

It should be noted that the effect roll has on the quadcopter's phase measurement was not investigated. Future work should understand how roll impacts the phase response over the pitch and yaw orientations observed during flights.

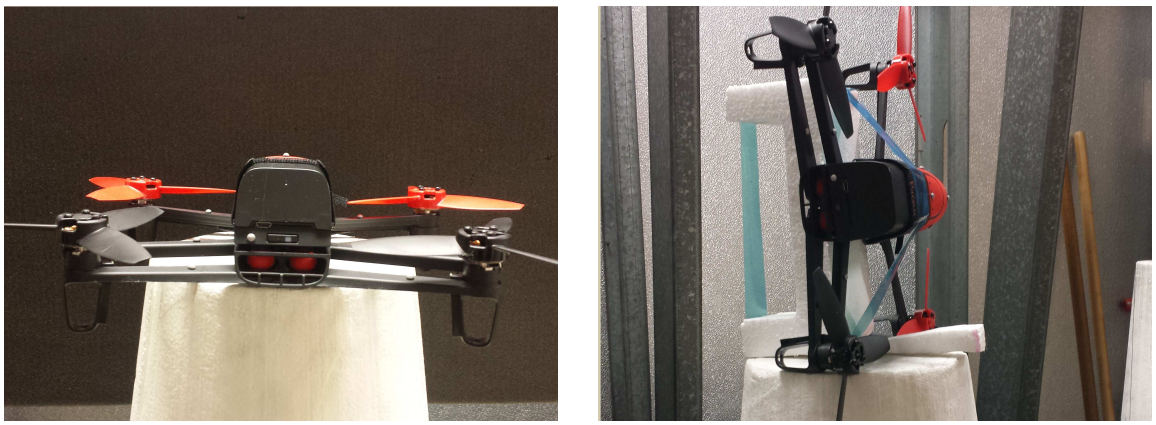

(a) (b)

Figure 47. Quad Only Yaw/Pitch Measurements: The Quad was placed flat (a) and on it's side (b) rotating the foam column to record the phase characteristics over ±5° of yaw and ±10° of pitch.

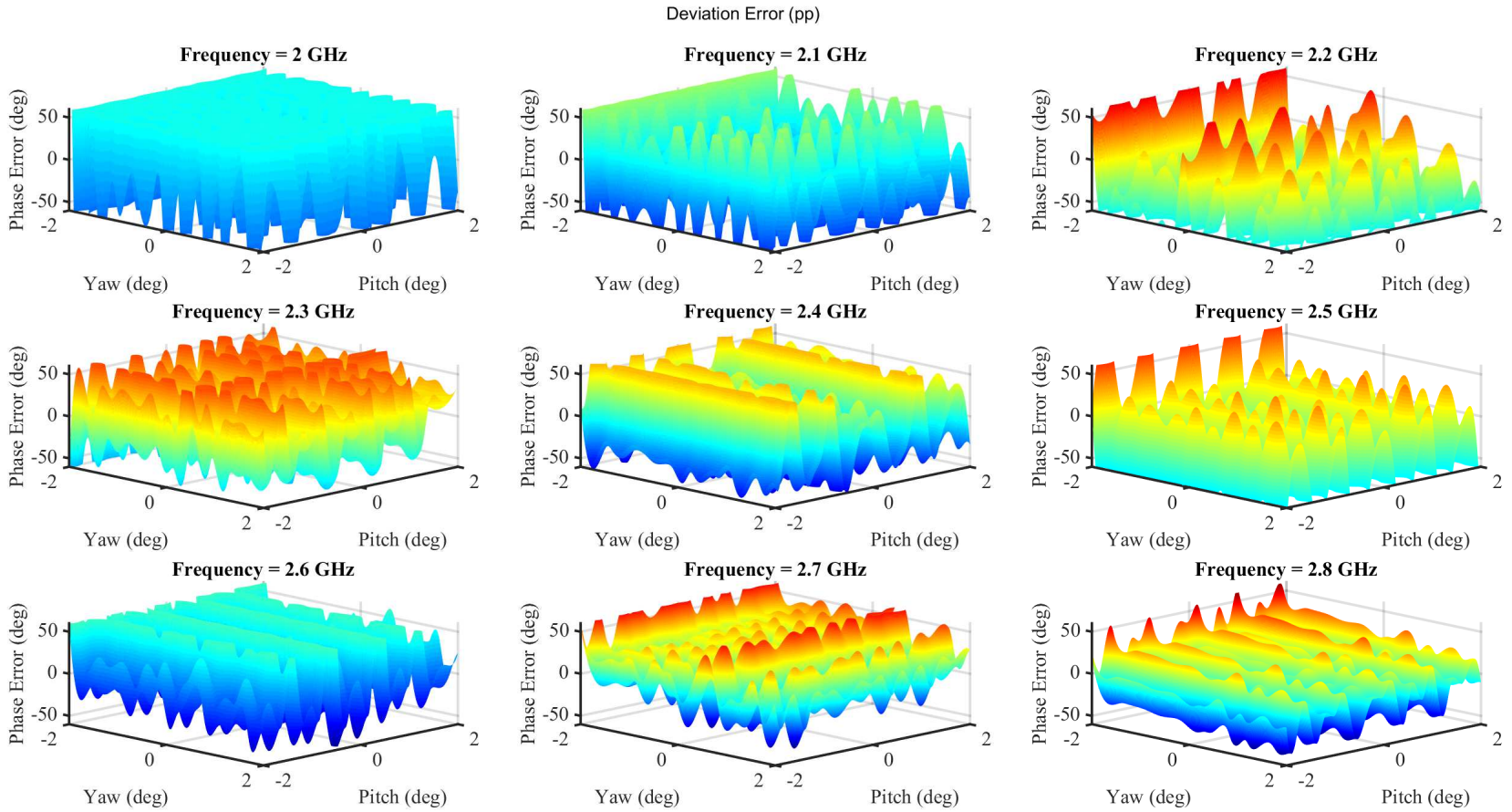

Figure 48. Pose Phase Deviations: Phase differences based on pitch and yaw aspect changes for the $2.0-2.8GHz$ band. Minor changes in either orientation could cause major changes in the measured phase based on the frequency response indicated here.

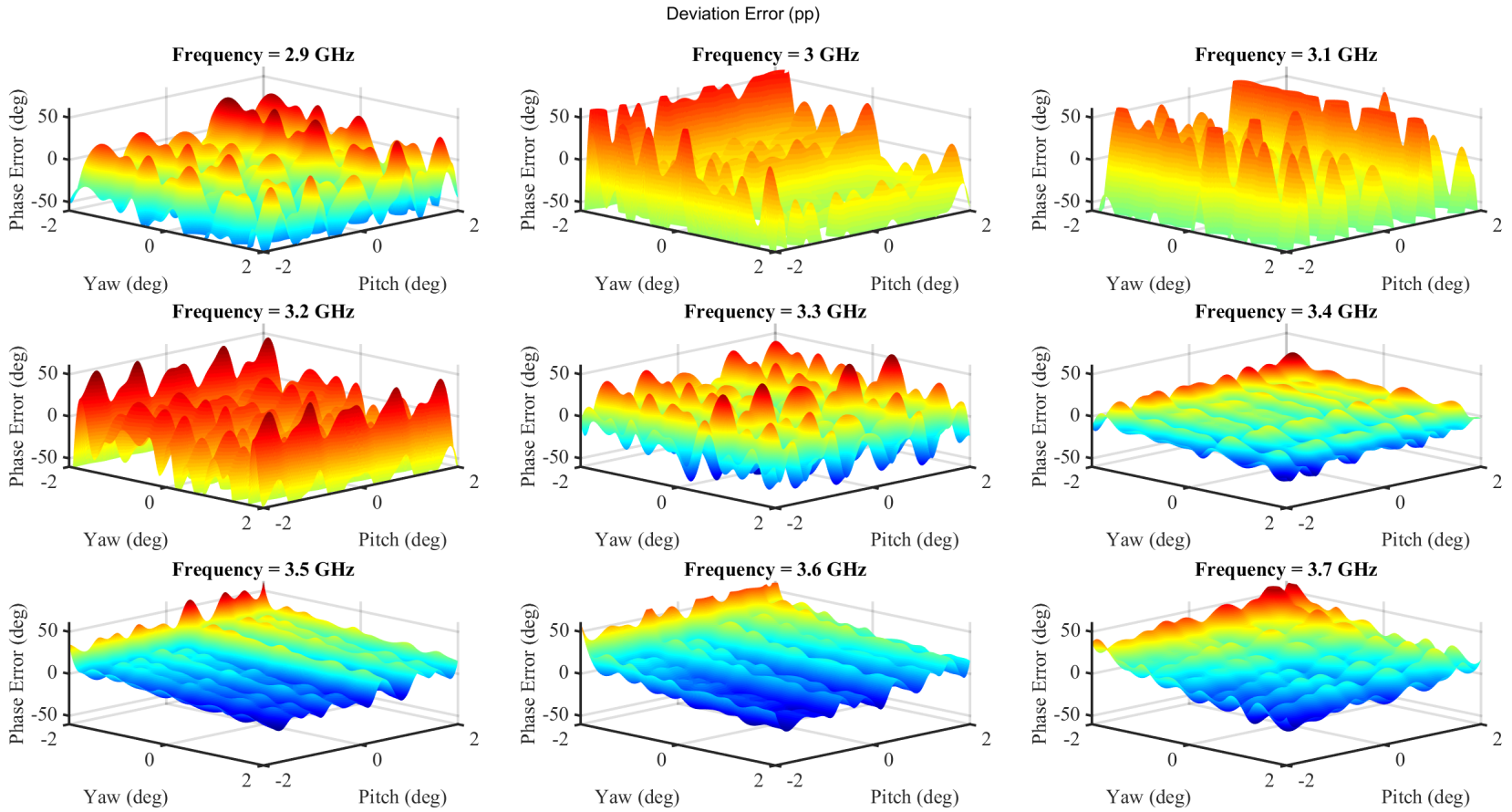

Figure 49. Pose Phase Deviations: Phase differences based on pitch and yaw aspect changes for the $2.9-3.7GHz$ band. Minor changes in either orientation could cause major changes in the measured phase based on the frequency response indicated here.

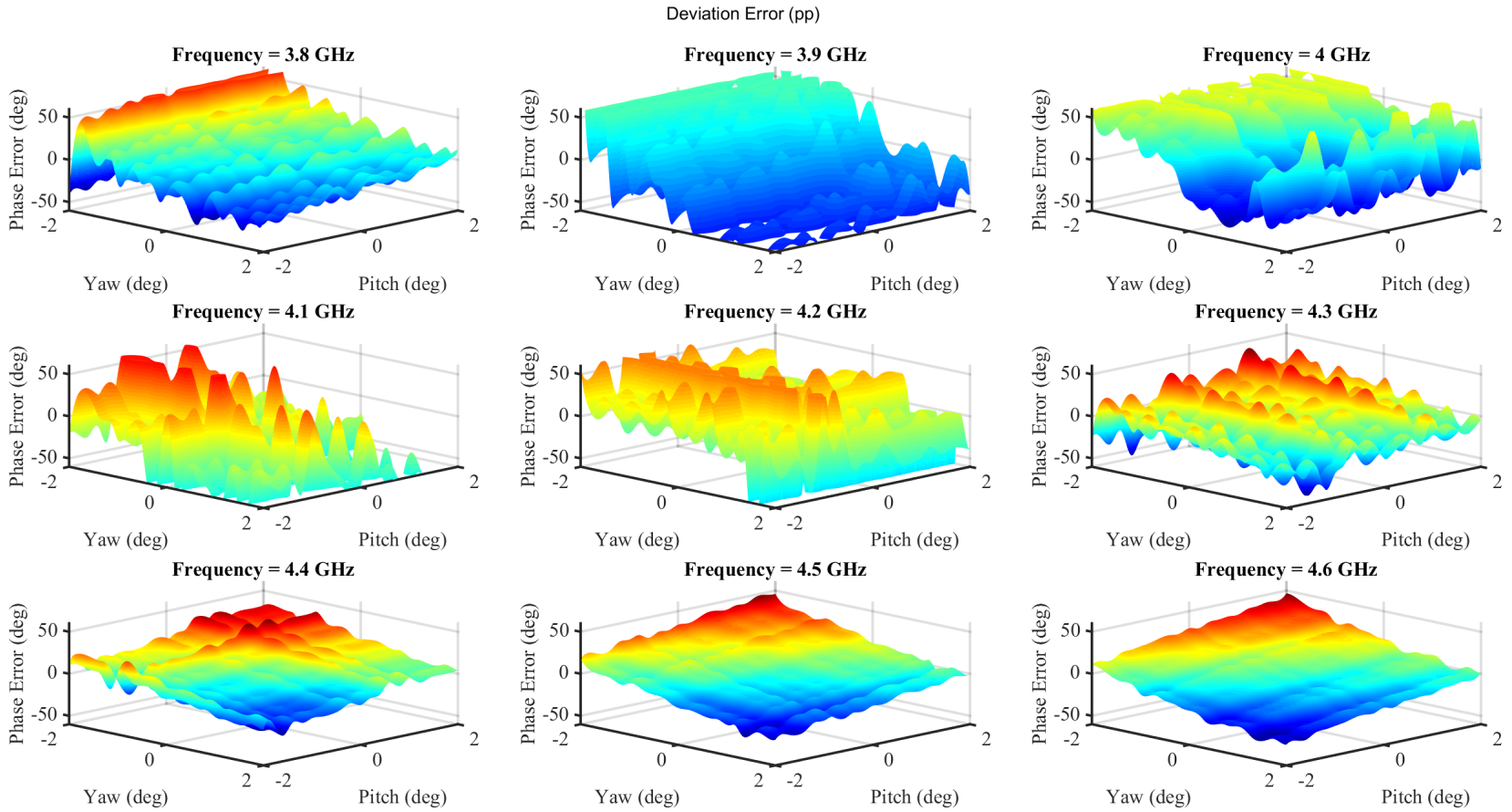

Figure 50. Pose Phase Deviations: Phase differences based on pitch and yaw aspect changes for the $3.7-4.6GHz$ band. Minor changes in either orientation could cause major changes in the measured phase based on the frequency response indicated here.

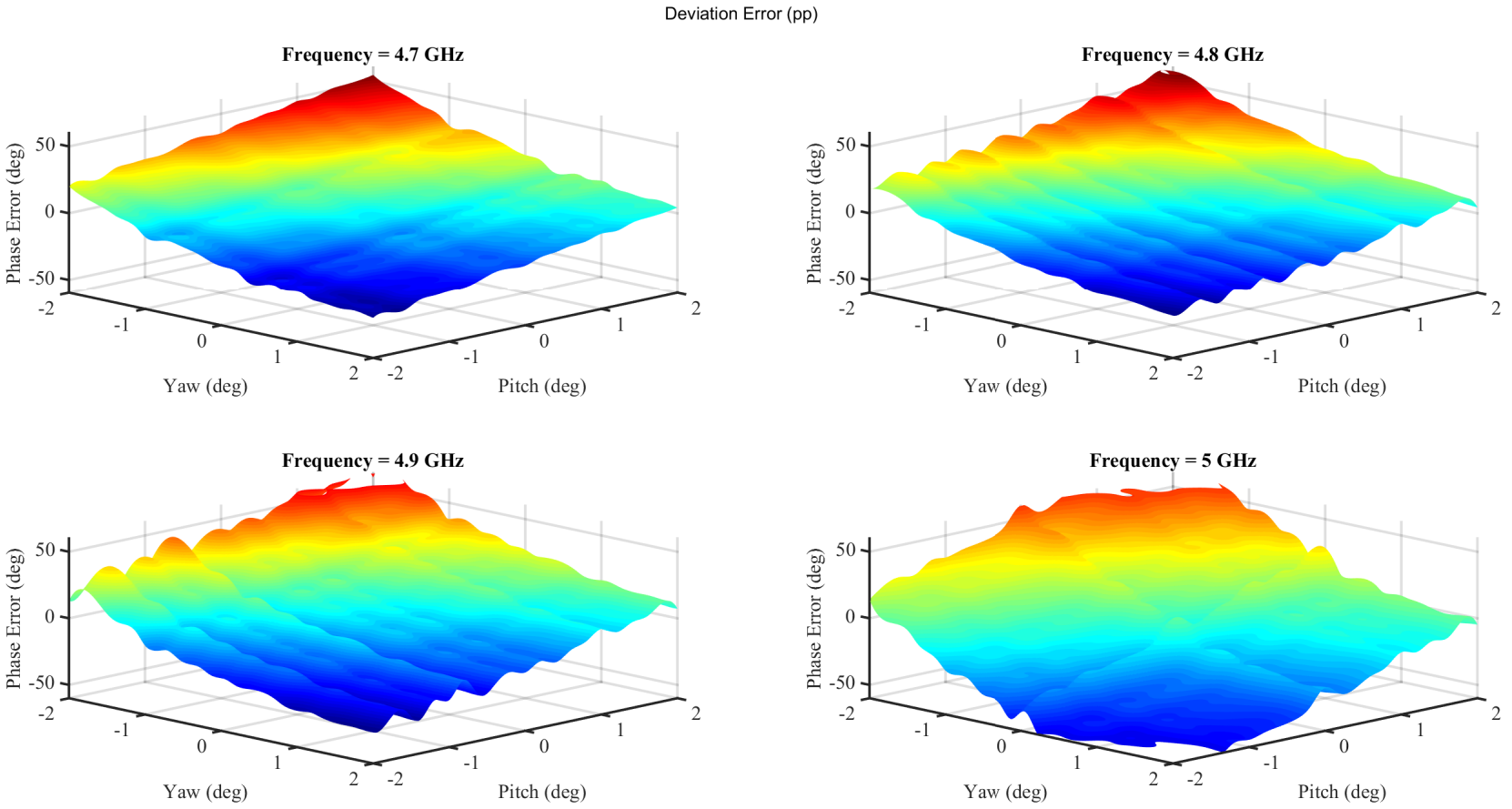

Figure 51. Pose Phase Deviations: Phase differences based on pitch and yaw aspect changes for the $4.7-5.0GHz$ band. Minor changes in either orientation could cause major changes in the measured phase based on the frequency response indicated here.

After calculating the quadcopter's pitch and yaw dependent phase characteristics, the data measured during the flight was analyzed. The quadcopter only, 500 mm, -19 ° XY slant scan flight profile was accomplished to compare against the one-way probe baseline. The flight position and pose statistics are shown in Figures 52 and 53. At each data point along the flight path, the phase measurement was phase compensated for pitch and yaw, as well as motion compensated in the y direction to the flight path goal position. The same phaser subtraction method mentioned in section 4.4 was applied. Because the two-way probe phase measurement experiences a round-trip doubling, the motion compensation was given a multiplication factor of 2. Additionally, the final compensated phase measurement was divided by two to allow for a direct comparison to the one-way probe measurement.

Altitude compensation was considered during the development of pose and motion compensation. It was solely based on the phase differences observed in the one-way probe measurements. The altitude compensation was accomplished similarly to pose compensation. A lookup table was created based on the phase difference between the measured altitude and the phase at 500 mm. No major impact to the final phase analysis was observed and was subsequently removed from the compensation calculation. The altitude error was accounted for in the uncertainty analysis.

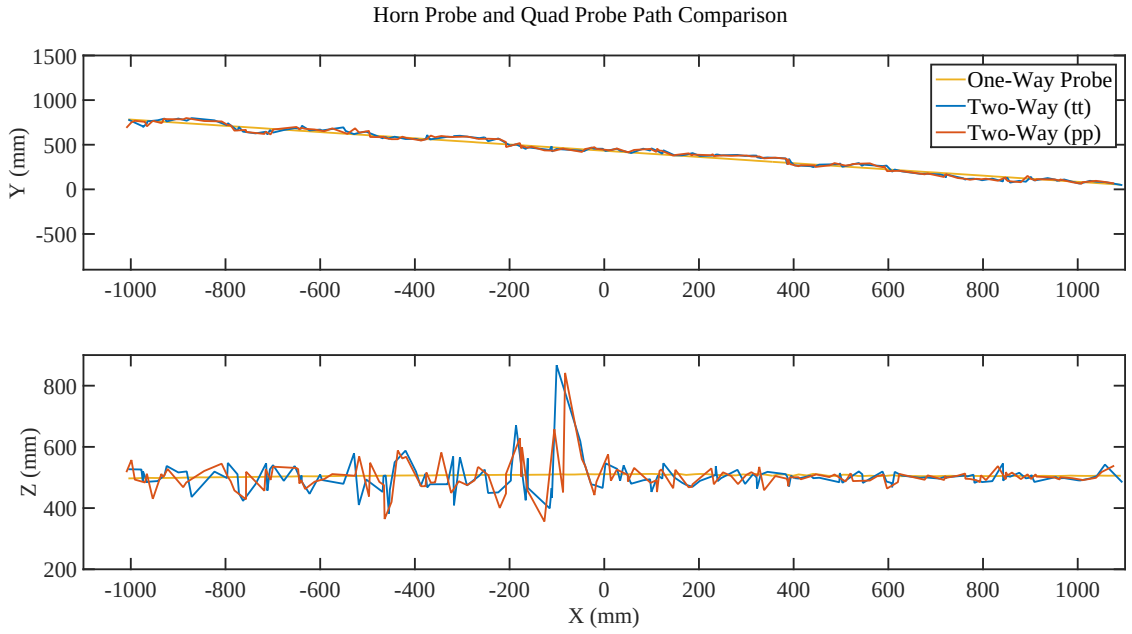

Figure 52. Paths of Two-Way Probe: The recorded path of the two-way probe measured in the Vicon™ space.

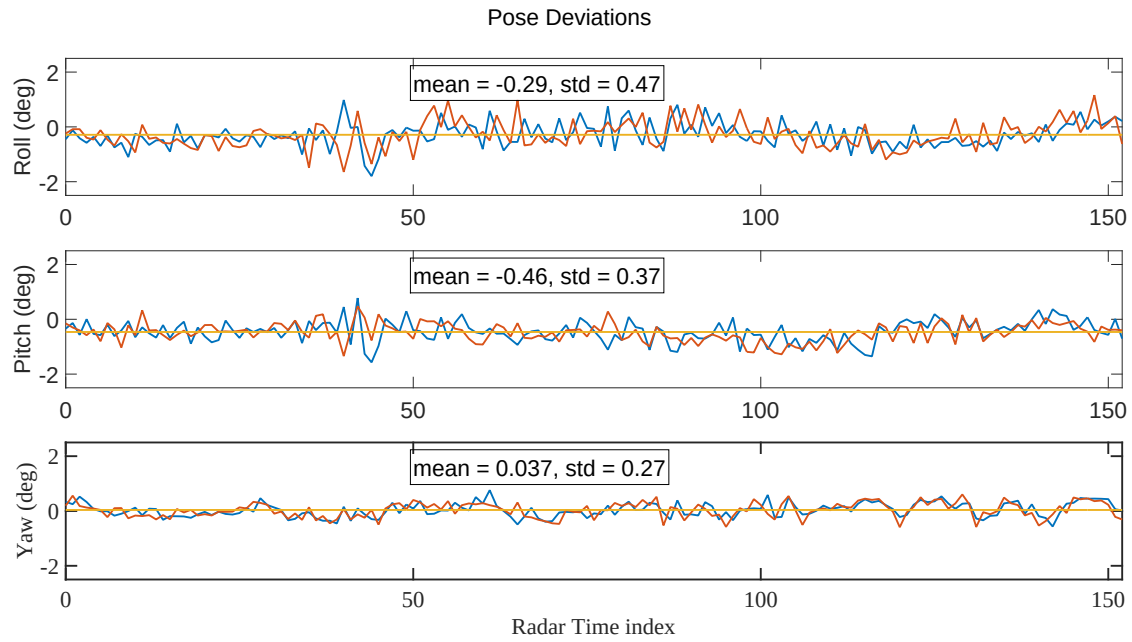

Figure 53. Probe Pose Deviations: The recorded path of the two-way probe measured in the Vicon™ space.

After compensation was applied, the data was smoothed over 21 sample points using a moving average filter; the results may be inconclusive at this point. The compensated phase response for each frequency was observed individually. On their own there does not appear to be a noticeable correlation between the one-way and two-way probe measurements. Though when observed together, as shown in Figure 54, a pattern was observed. As each phase front cycles through 2π iterations, moving from right to left, the phase for each frequency sample dips down then trends positively. Each frequency sample positively follows the second 2π iteration increase with increasing predominance as frequency was increased. Additionally, a ripple was on the left for all frequency samples. It was unclear if the pattern was caused by the measurement, or by the smoothing operation of a discontinuous pattern, or a combination of the two.

When the phase was unwrapped, a few examples demonstrated where the measured phase potentially reflected the general shape of the phase front. The best example with the closest shape over the entire path was the 2.2 GHz vertical polarization measurement shown in Figure 55. Another example with positive results was the horizontal polarization for 4.3 GHz shown in Figure 56. Observing the sample in the same manner as the flight path, the 4.3 GHz pp sample closely follows the measurement gathered by the one-way probe. Further examples demonstrate similar but less conclusive results as seen in Figure 57. However, the remaining results do not appear to have any similarity to the one-way probe measurement as depicted in Figure 58.

At the reduced translation velocity the quadcopter did not monotonically increase in the x direction. It was believed the phenomenon could impact the unwrapping of the phase in post processing. A sorting function was performed on the data to ensure a positive increase in x was observed by the unwrap function. How-

ever, no conclusive results were observed. Some samples were arguably improved visually, Figures 59 and 60 while others where degraded, Figures 61 and 62.

An attempt was made to combat errors from smoothing a discontinuous function. The phase measurements were unwrapped about -180 ° to 180 °, smoothed with an 81 point moving average, then returned to the angles from phaser form. The best visual results are illustrated in Figure 63. Immediately, a comparable response was identified. At each of the end-points in x, the phase increased with phase measured with the one-way probe. The phase transitioned through 180 ° to 180 ° within $25 - 200$ mm between each probe's measurement. Then followed the general curvature of the phase front between 700 mm and -700 $mm \pm 100$ in x. The results exhibited here are not conclusive on their own. Deeper analysis must be accomplished to better understand the moving average's impact. It can be concluded that general phase front characteristics can be reconstructed using pose and motion compensated phase measurements from a quadcopter base two-way probe. Examples where the reconstructed phase front bared little to no resemblance to the original one-way field probe measurement are shown in Figure 64.

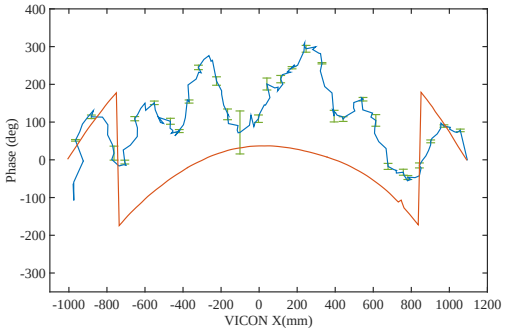

(a) 2.5GHz tt

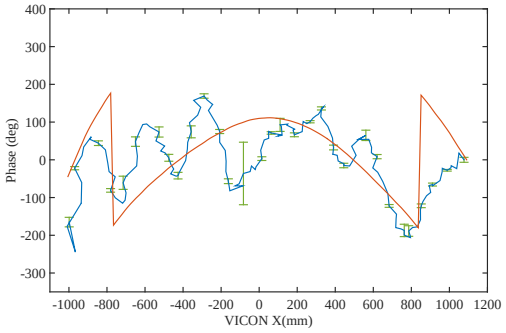

(b) 3.0GHz pp

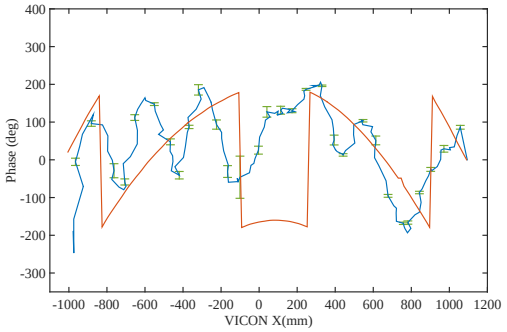

(c) 3.5GHz tt

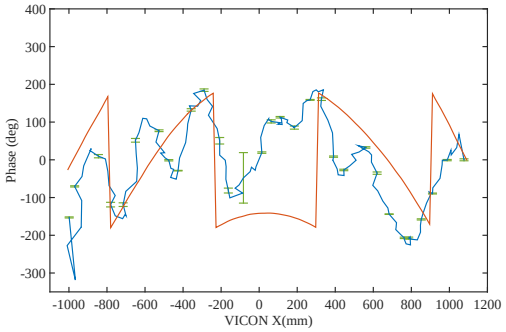

(d) 4.0GHz pp

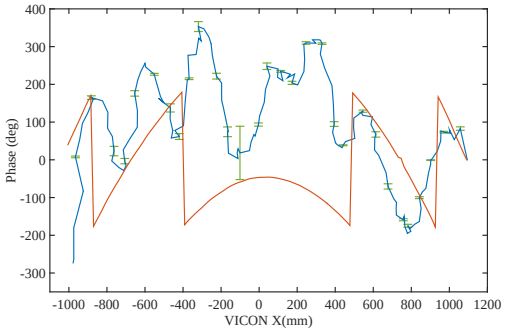

(e) 4.5GHz tt

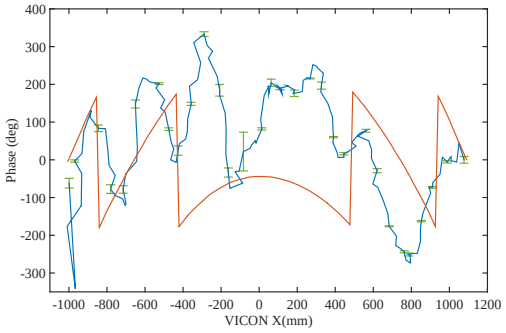

(f) 5.0GHz pp

Figure 54. Flight Phase $2.0 - 5.0GHz$**: The smoothed phase data demonstrates a similar pattern between each frequency with a general tendency to follow the one-way probe measurements.**

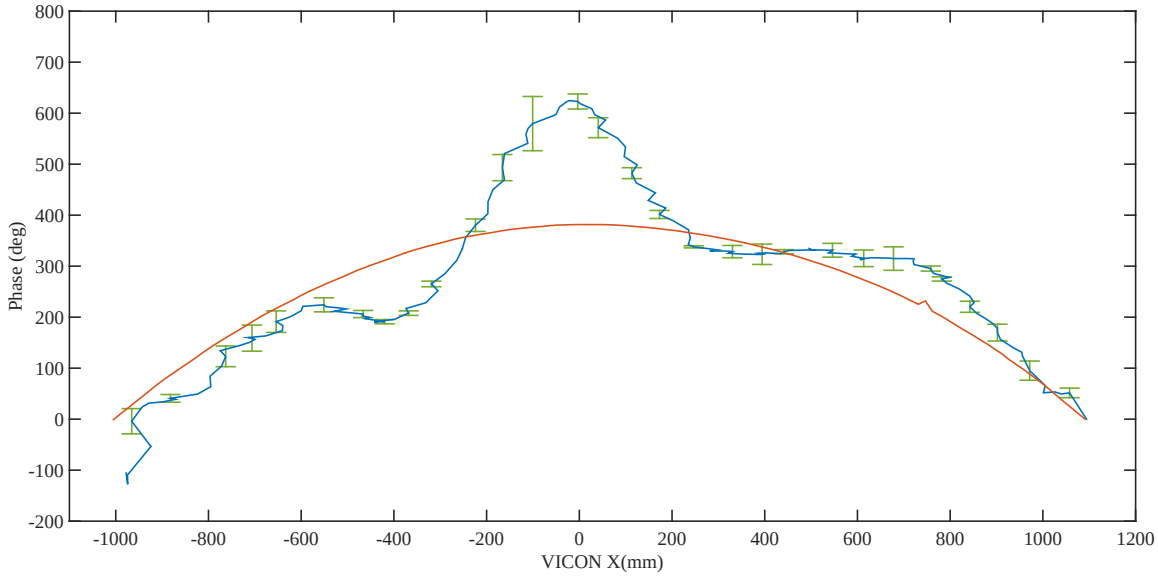

Figure 55. Flight Unsorted Unwrapped Phase $2.2GHz$ tt: Unsorted and unwrapped phase comparison of Quad-Copter only flight to one-way probe measurement for $2.2GHz$ vertical polarization.

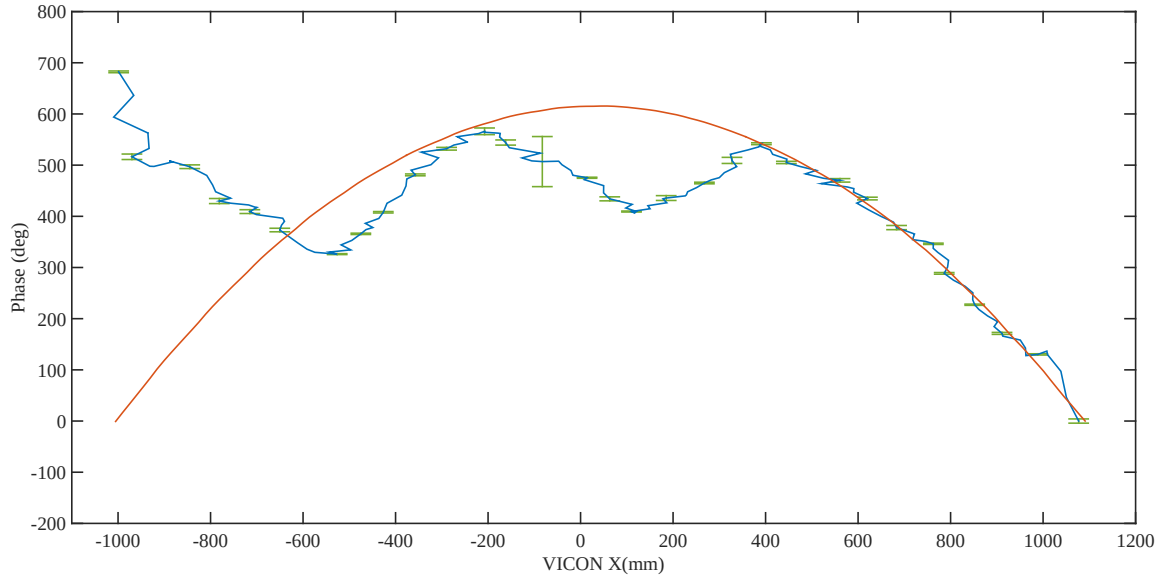

Figure 56. Flight Unsorted Unwrapped Phase $4.3GHz$ pp: Unsorted and unwrapped phase comparison of Quad-Copter only flight to one-way probe measurement for $4.3GHz$ horizontal polarization.

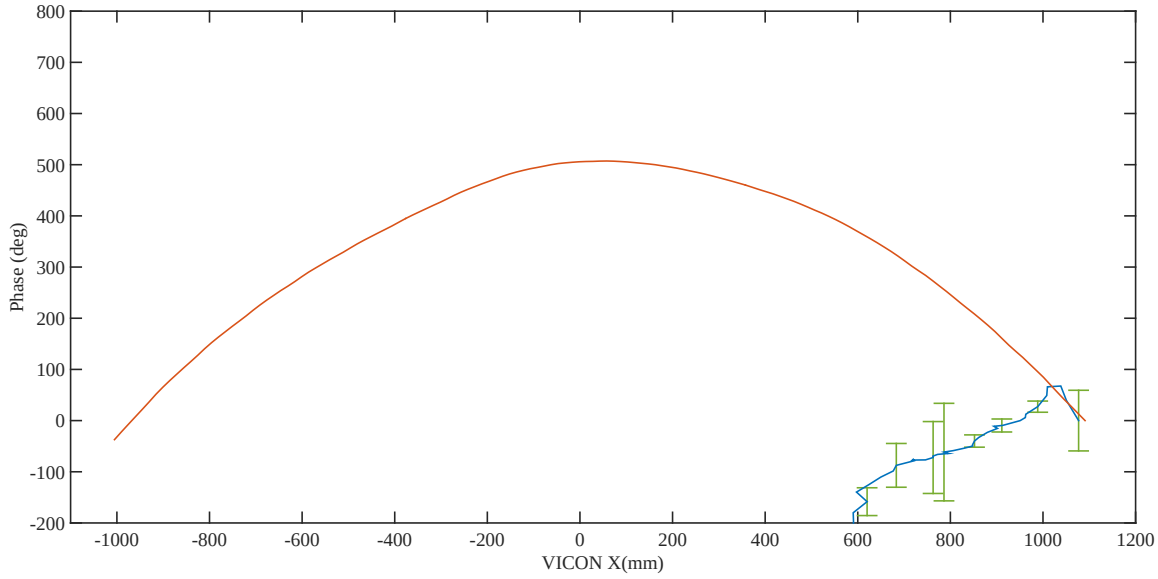

Figure 57. Flight Unsorted Unwrapped Phase $3.4GHz$ pp: Unsorted and Unwrapped phase comparison of Quad-Copter only flight to one-way probe measurement for $4.GHz$ horizontal polarization.

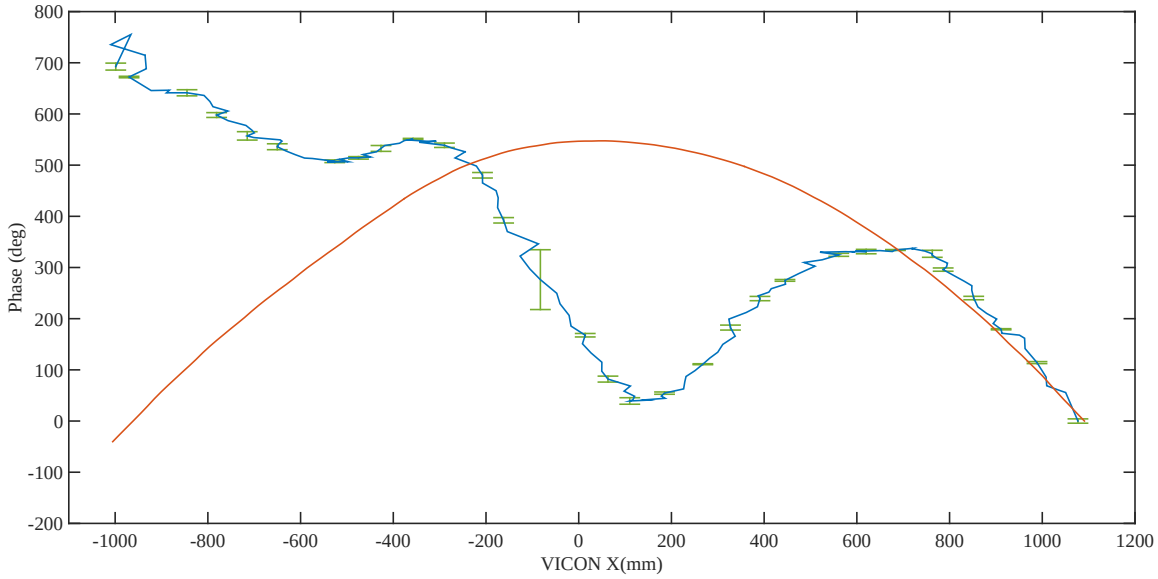

Figure 58. Flight Unsorted Unwrapped Phase $3.4GHz$ pp: Unsorted and Unwrapped phase comparison of Quad-Copter only flight to one-way probe measurement for $4.GHz$ horizontal polarization.

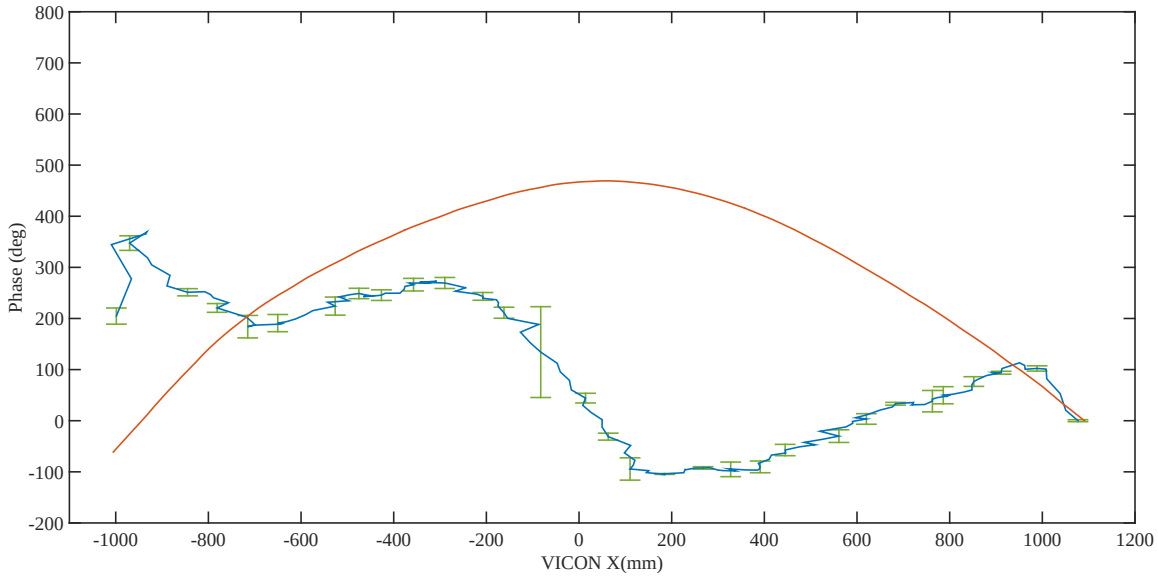

Figure 59. Flight Unsorted Unwrapped Phase $2.9GHz$ pp: Unsorted and Unwrapped phase comparison of Quad-Copter only flight to one-way probe measurement for $2.9GHz$ horizontal polarization.

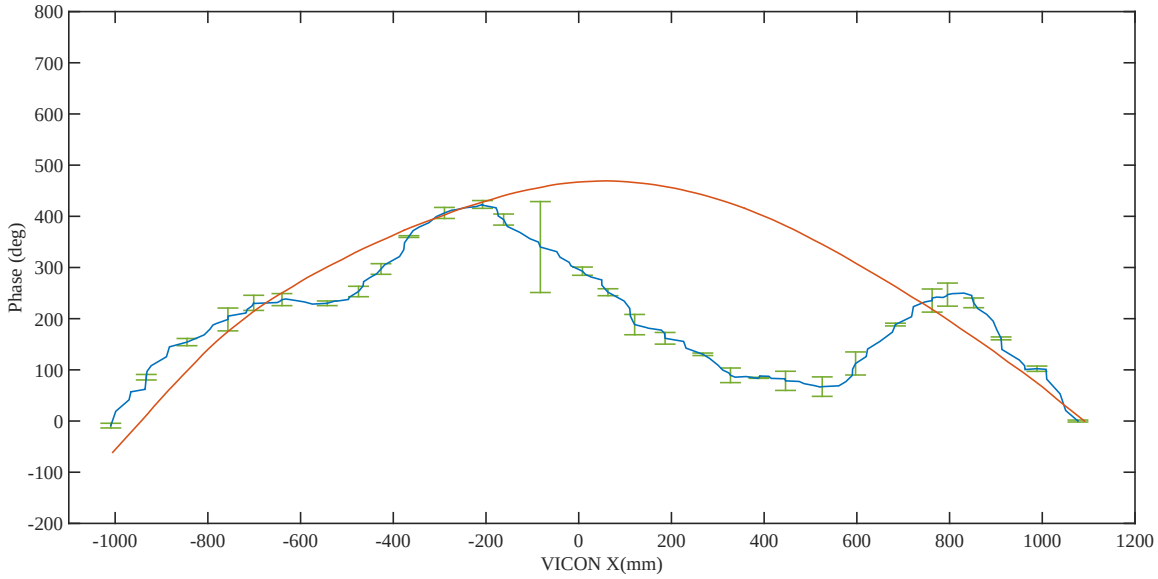

Figure 60. Flight Sorted Unwrapped Phase $2.9GHz$ pp: Sorted and Unwrapped phase comparison of Quad-Copter only flight to one-way probe measurement for $2.9GHz$ horizontal polarization.

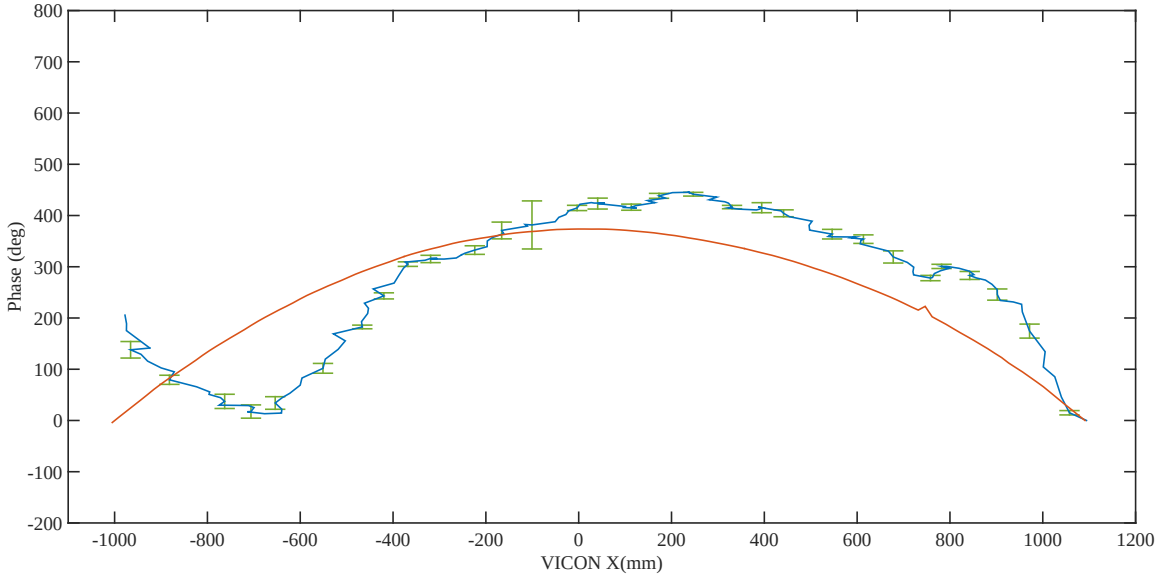

Figure 61. Flight Unsorted Unwrapped Phase $2.1GHz$ pp: Unsorted and Unwrapped phase comparison of Quad-Copter only flight to one-way probe measurement for $2.1GHz$ horizontal polarization.

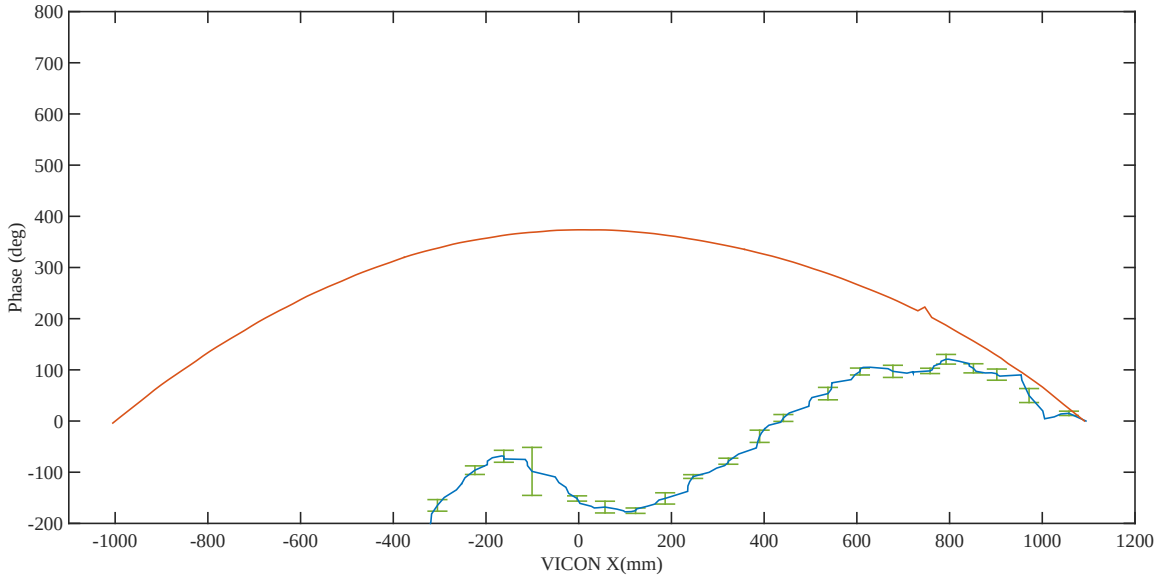

Figure 62. Flight Sorted Unwrapped Phase $2.1GHz$ pp: Sorted and Unwrapped phase comparison of Quad-Copter only flight to one-way probe measurement for $2.1GHz$ horizontal polarization.

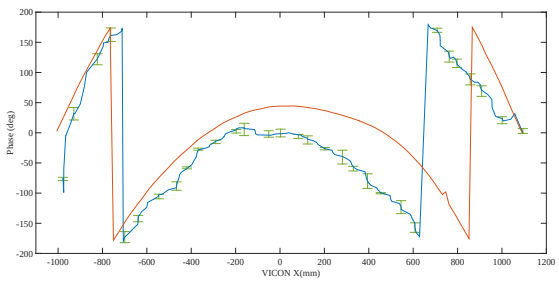

(a) $2.6GHz$ tt

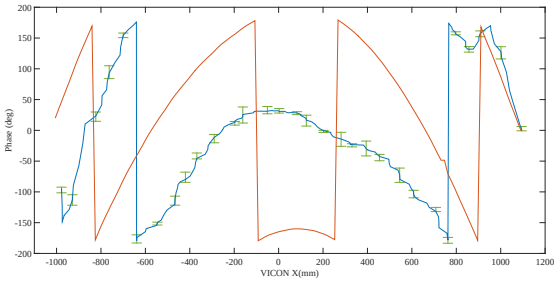

(b) $3.5GHz$ tt

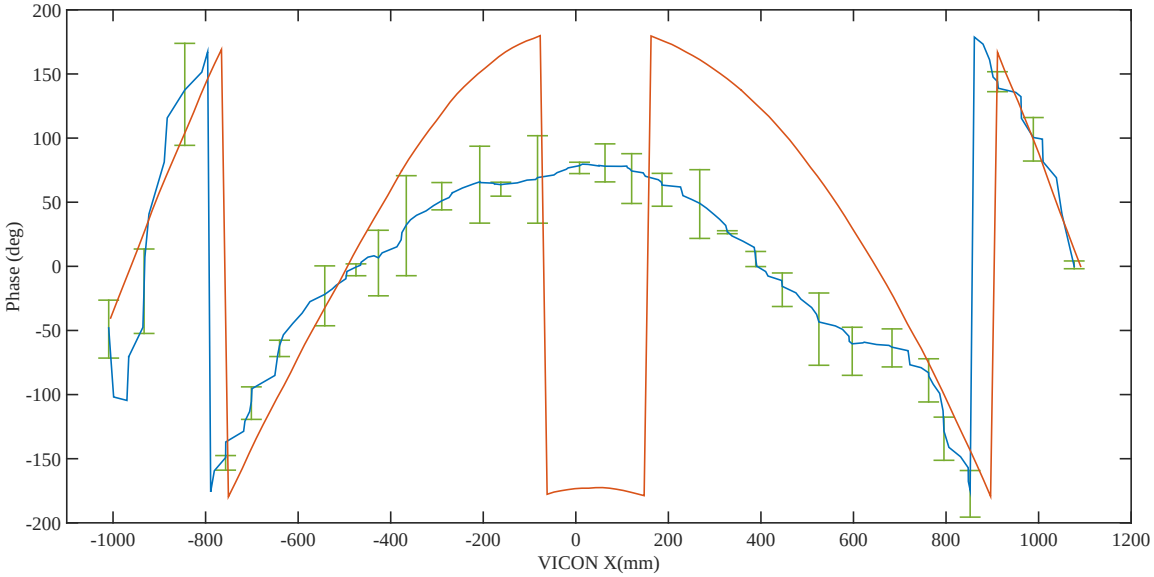

(c) $3.7GHz$ pp

Figure 63. Flight Phase Unwrap, Smooth, Wrap $2.6, 3.5, 3.7GHz$: Each data point was unwrapped in phase about -180° to 180°, smoothed through 81 points, then wrapped about -180° to 180°.

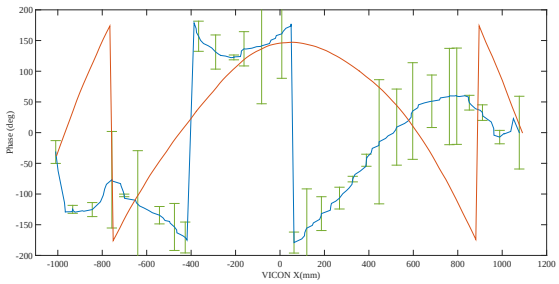

(a) $3.4GHz$ pp

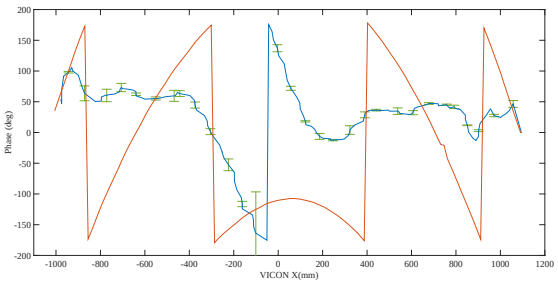

(b) $4.1GHz$ tt

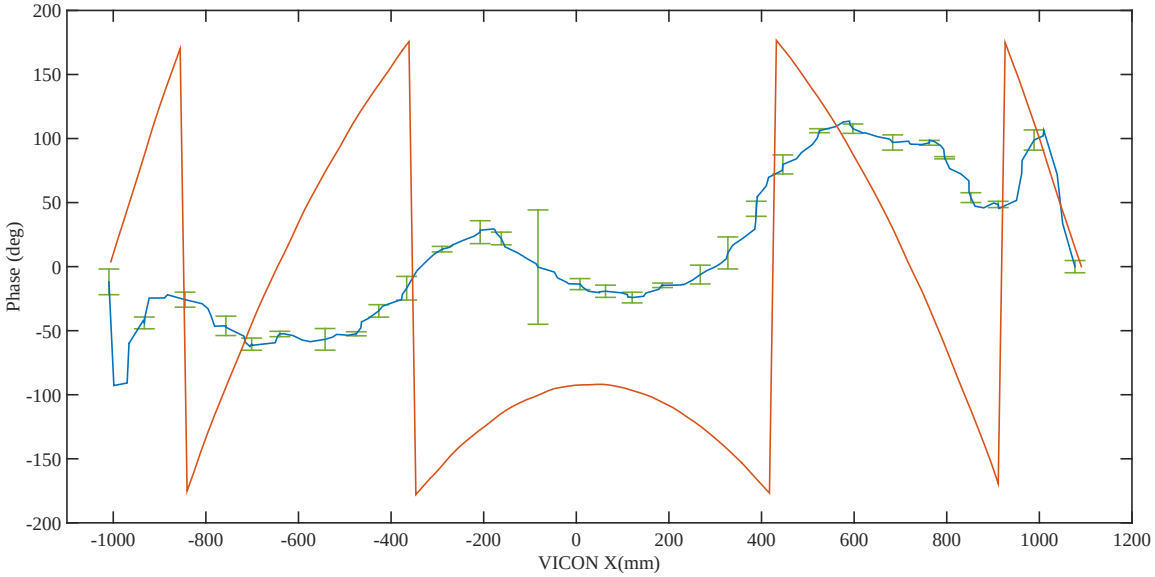

(c) $4.4GHz$ pp

Figure 64. Flight Phase Unwrap, Smooth, Wrap $3.4, 4.1, 4.4GHz$: Each data point was unwrapped in phase about -180° to 180°, smoothed through 81 points, then wrapped about -180° to 180°.

4.7 Uncertainty Analysis and Error Sources

During setup and execution of each measurement described in this chapter, multiple sources of error were introduced. Errors with known sources of origin were included in an uncertainty analysis. Remaining error sources will need to be determined by a more in depth investigation of the overall integrated system. The potential sources of the remaining errors will be discussed later in this section.

Because the primary focus of this research was to implement a geodesic sphere encased quadcopter as a two way probe, an uncertainty analysis was strictly performed on the quadcopter only measurement. The identified error sources in the uncertainty analysis were: errors in Vicon™ measured position affecting motion compensation, errors in Vicon™ measured pose affecting pose compensated phase subtraction, and the unknown affect of deviations in altitude. When first configuring objects in the Vicon™ Tracker software, fluctuations in an object's position and pose were discovered. A quadcopter with a defined Vicon™ object was placed in a stationary position in the test chamber. Position and pose of the quadcopter was recorded for 16 s at 1 ms intervals illustrated in Figure 65. The resultant standard deviations were provided in Table 5.

The measurement statistics used in the uncertainty analysis were the Vicon™ observed y and z position values, pitch orientation angle, and yaw orientation angles. Uncertainty in the x position will need to be investigated further as it applies to the integrated systems operational application. Roll uncertainties were not considered in the uncertainty analysis.

The uncertainties from the compensated phase subtraction calculation from Equation 17 were processed using a root-sum-square method from [16] as seen in Equation 18.

Table 5. Standard Deviations of Vicon™ Measurements

Position		$\sigma(mm)$	Pose		$\sigma(^\circ)$
σ_x	=	0.0549	σ_r	=	0.0380
σ_y	=	0.0392	σ_p	=	0.0365
σ_z	=	0.1681	σ_{yaw}	=	0.0040

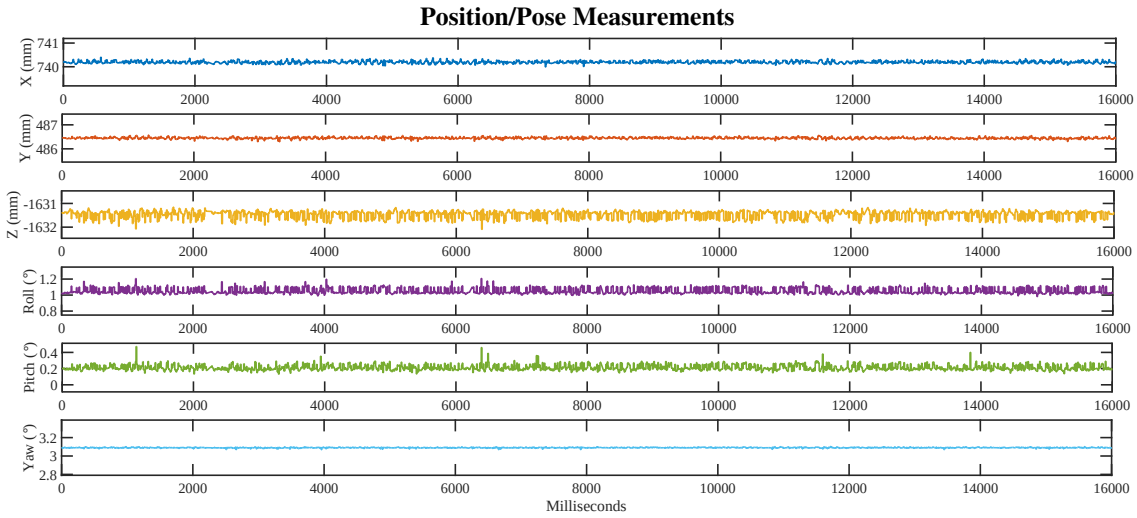

Figure 65. Stationary Quadcopter Position/Pose Measurements: Position and Pose measurements of a stationary Quad-Copter. Measured every ms for 16 s. Each position scale are $2mm$, pose scale are 1°

$$U_R = \pm t_{95}\left[\sum_i (\theta_i U_{A_i})^2\right]^{\frac{1}{2}} \tag{18}$$

Where t_{95} is the Student's t statistic coefficient for 95% confidence, U_{A_i} is the standard deviation of the i^{th} uncertainty source, θ_i is the sensitivity of the test measurement result of the i^{th} uncertainty source. Because Equation 17 was a simple sum and difference equation, each term of θ_i was 1. The motion compensation term was defined by simple substitution of σ_y for it's uncertainty source standard deviation.

To determine the uncertainty of the pose error source, the standard deviations, $\pm\sigma_p$ and $\pm\sigma_{yaw}$, were applied to the pitch and yaw value at each sample point. The phase difference value for the new pitch and yaw was determined using the lookup table described earlier. The difference from the new standard deviation phase from the originally measured phase difference was determined for each of the four combinations of $\pm\sigma_p$ and $\pm\sigma_{yaw}$. It was the standard deviation of these four difference from the difference that defined the standard deviation of the pose uncertainty source.

Finally, the altitude error source uncertainty was defined by applying the difference in phase measured at zero altitude difference and the phase difference value at the actual altitude was applied as the standard deviation. The phase error uncertainty due to altitude assumed uniformity in the field for vertical translation at each position in x.

It was assumed that all position and pose errors were independent from each other, meaning an error in one source did not impose an error on another. For simplicity, it was assumed that the degrees of freedom (v), or the potential number of error contributors, was high [16]. Therefore, the Student's t statistic for 95% confidence, t_{95}, was evaluated as $t_{95} = 2$; a table of t_{95} values for degrees of freedom was provided in [16]. As a result, an uncertainty value was defined for each data sample and applied to the figures in Section 4.6 referring to the captured quadcopter only flight data.

Although calibration errors were calculated with the 750 and 900 calibration cylinders, the uncertainty in calibration was not included. At the time of this writing it could not be determined how to apply a calibration measurement to the two-way probe when there was no clear process for calibrating the one-way measurements without accurate probe compensation data for the antenna. Additionally the

calibration error would be a constant applied phase error for each data sample in x with respect to frequency. All other deviations in the two-way quadcopter probe results can be attributed to: error in time stamp synchronization, uncertainty in the affects roll contributes to pose compensation, errors introduced when pitch and yaw calibration measurements were conducted, and a non-uniformity of the phase front in vertical translation across positions in x and y.

4.8 Summary

As a whole, the overarching results from this research show promise in application. A fundamental baseline of the test chamber's phase front was established in stage one. Stage Two confirmed the integrated systems capability to combine visualizations of radar measured phase path translation with physical translations. Finally, stage three indicated, though further investigation and analysis is required, a potential capability exists for using a quadcopter as a two-way field probe. The final fidelity of the capability must also be ascertained.

Again, the purpose for performing stage one was not for directly matching with a two-way probe, but for general confirmation of the radar, Vicon™, and two-way probe integrated system's phase front representation capability. Without having identified the results in section 4.2, stage three would have no basis for comparison.

Stage two provided the foundation for pose compensation of a non-uniform two-way probe. Additionally, it was determined that any gains in field detection fidelity lies first and foremost with the pose dependent phase compensation data. Without said pose information, reconstruction of the phase front's characteristics will be limited if possible at all. Furthermore stage two bridge the gap between phase front detection with a one-way probe to detection with a two-way probe.

The final stage identified many of the integrated system's shortcomings. Data from the first successful flights uncovered an under-sampling problem. Successive flights and crashes provided insight into the fragility of the sphere and affects of impact damage. Unfortunately, it was after catastrophic structural damage that the sampling issue was addressed. There were other major areas of improvement that will be discussed further in Chapter V.

V. Conclusions and Recommendations

This chapter discusses the conclusions drawn from the analyzed results outlined in Chapter IV and their significance. Recommendations for future action and considerations will be presented. Additional recommendations for future work will be provided.

5.1 Conclusions of Research

Chapter IV defined the build up process for validating the use of a quadcopter based two-way probe. A brief description of which measurements would be utilized in post processing were described. The general expectation of each stages research results were described. Each stage provided individual results and analysis. An uncertainty analysis was conducted and defined known error sources with impacts to the collected data. Unknown error sources and their potential impacts were identified. This section will summarize the conclusions made during each stage.

The phase front characteristics identified by measuring with a one-way probe established a baseline for the subsequent two-way probe measurements. The measurement also demonstrated the utility of integrating the Lintek 4000 phase measurements with the Vicon™ position measurements. As a result, it was determined that the phase front was not oriented as expected. In fact, the phase front was slanted -19 °. It was also concluded that the dimensions of the 22 ° quiet zone were not as large as expected. The average horizontal and vertical quiet zone dimensions were calculated to be 477 mm and 461 mm.

Utility of the system was expanded by capturing phase and position data of two way probes. Translations in physical space and phase space of a 350 calibration cylinder were compared and confirmed. Although not quantified, it was confirmed

that the path of a geodesic sphere could be recreated using the integrated phase and position measurements when pose compensated. The results from stage two, bridged the gap between stage one and the final stage.

Due to the unstable nature of the quadcopter and Geodesic sphere integration, an example of a flying geodesic sphere encased quadcopter was not analyzed. However, a quadcopter only measurement was collected and analyzed. Though not conclusive in their entirety, the analysis showed promise. There were some instances where the compensated quadcopter two-way probe measurement closely followed the one-way probe baseline. Insufficient data samples from the initial flight tests identified an immediate limitation in the system. Due to battery endurance and a finite flight time, to collect enough data samples, the number of altitude positions will need to be reduced. Sphere calibration measurements were collected before and after sustained impact damage. Because the differences between the two measurements were so great, > 100 °, it was concluded that great care is required when handling and collecting sphere calibration measurements.

5.2 Significance

The overarching significance of this research was that a quadcopter based two-way field probe proof of concept was demonstrated. An integrated RCS, Vicon™ motion capture of a Geodesic sphere encased quadcopter developed and demonstrated multiple flight path capabilities. Flight tests immediately identified the need for improved sampling of data points. Flaws in the sphere to quadcopter attachment design identified the importance of developing an interface that does not interfere with the quadcopter's flight characteristics.

Finally, an uncertainty analysis determined that errors in the y axis measurement were insignificant. Errors in pitch and roll had varying affects and were de-

pendent on the calibrated phase response at each frequency measurement. Further analysis must be conducted to understand uncertainties associated with deviations in roll and altitude.

5.3 Recommendations for Actions and Considerations

The first recommendation for action is to improve the motion control system. One element is to eliminate flight characteristic interference from the geodesic sphere to quadcopter attachment points. A general elimination of programming redundancies and overall simplification of the main flight control system would provide an easy and straight forward platform for future experiments. Two final flight system action recommendations are to choose a quadcopter with improved payload capacity and a more robust sphere, or continue to use the Parrot® Bebop with multiple replacement spheres.

Any future collection of flight data with phase measurements should be done with a position and pose measurement collected at the beginning and end of each frequency's pulse train. As described in Chapter IV, the current system takes a single position and pose measurement at the end of a frequency sweep. It is predicted that the greatest area for reducing unknown uncertainties will be recognized by improving position synchronization.

Due to uncontrollable circumstances, each flight profile was conducted once. To better understand the entire system's capabilities and limitations, each flight profile should be performed multiple times. A better statistical analysis would be critical to making system improvements. Furthermore, after establishing a fundamental statistical baseline, all changes made to sphere design and calibration techniques would be quantifiable.

A final recommendation is to develop a better understanding of Vicon™ configuration. Proper configuration and calibration of the Vicon™ system should reduce object jitter and eliminate dramatic changes in perceived pose. Both improvements would provide a stable feedback platform for the flight control system in addition to reduced uncertainty errors.

5.4 Recommendation for Future Research

There are many new avenues of research to recommend for future investigation. As stated in previous work [3], it will be reiterated that the influence of geodesic sphere design should be analyzed. A 2 ν frequency design was used in both research projects, more frequency designs are available. In conjunction with frequency design, the impact of nominal orientation of the sphere as it is attached to the quadcopter could identify a configuration with reduced roll, pitch, and yaw induced uncertainties.

Incorporating a rotational rate to the quad was intended for this research but was not realized. By including a rotation, a statistical smoothing would be applied to the final measurement. Associated in this future work, should be to determine what translational rate is required for any given flight profile to achieve an adequate sample space.

Furthermore, investigating the most effective/efficient way to probe the quiet zone with the quadcopter and geodesic sphere two-way probe would be beneficial. RCS test facilities have little spare time between measurements and flight time of the quadcopter is limited by battery endurance. Therefore a flight profile that minimizes range usage with maximum effectiveness needs to be determined.

5.5 Summary

The majority of effort required by this thesis was devoted to system engineering. Four independent systems required some form of integration with one another, each integration point having inherent problems. A Lintek 4000 RCS measurement system was integrated with a Vicon™ motion capture system. In turn the Vicon™ system integrated flight control with the Parrot® Bebop quadcopter. And finally the Parrot® Bebop was integrated with a geodesic sphere. With the incorporation of each system, unique problems arose. However, with every addition, a unique new capability was realized.

Utilization of a geodesic sphere encased quadcopter as a two-way field probe is becoming realizable. A geodesic sphere has been demonstrated as an effective static two-way field probe. And a quadcopter has arguably been demonstrated as a dynamic two-way field probe. By further integrating the two and establishing a statistical baseline, a new standard in field probing may have emerged.

Bibliography

[1] E. Knott, *Radar Cross Section Measurments.* SciTech Pub., 2006.

[2] E. Knott, J. Shaeffer, and M. Tuley, *Radar Cross Section, Second Edition*, ser. SciTech (New York, N.Y. Institution of Engineering and Techology, 2004.

[3] T. Albee, "Unique two-way field prove concept utilizing a geodesic sphere and quad-rotor," E. Eng. Thesis, The Air Force Institute of Technology, March 2015.

[4] R. J. Moffat, "Describing the uncertainties in experimental results," *Experimental Thermal and Fluid Science*, vol. 1, no. 1, pp. 3–17, 1 1988.

[5] J. Dossett, "Characterization of quad-rotor positioning systems and the effect of position uncertainties on field probe measurements," E. Eng. Thesis, The Air Force Institute of Technology, March 2016.

[6] H. Kenner, *Geodesic math and how to use it.* Univ of California Press, 1976.

[7] C. A. Balanis, *Advanced engineering electromagnetics.* Wiley Online Library, 2012, vol. 111.

[8] S. Wentworth, *Fundamentals of Electromagnetics with Engineering Applications.* Wiley, 2005. [Online]. Available: https://books.google.com/books?id=FIUrAQAAMAAJ

[9] M. I. Skolnik, *Radar Systems.* McGraw-Hill, NY, 2001.

[10] M. A. Richards, J. Scheer, W. A. Holm *et al.*, *Principles of modern radar: basic principles.* SciTech Pub., 2010.

[11] D. McNamara, C. Pistorius, and J. Malherbe, *Introduction to the Uniform Geometrical Theory of Diffraction*, ser. Antennas and Propagation Library. Artech House, 1990.

[12] R. G. Kouyoumjian and L. P. Jr., "Range requirements in radar cross-section measurements," *Proceedings of the IEEE*, vol. 53, no. 8, pp. 920–928, 1965, iD: 1.

[13] T. E. Tice, "An overview of radar cross section measurement techniques," *Instrumentation and Measurement, IEEE Transactions on*, vol. 39, no. 1, pp. 205–207, 1990, iD: 1.

[14] J. H. R, *Measurement, Sensors, and Instrumentation Handbook. Chapter 1: Characteristics of Instrumentation.* CRC Press, 02/26; 2015/07 1999.

[15] B. M. Kent, "Comparative measurements of precision radar cross section (rcs) calibration targets," in *Antennas and Propagation Society International Symposium, 2001. IEEE*, vol. 4, 2001, pp. 412–415 vol.4, iD: 1.

[16] R. H. Dieck, *Measurement, Sensors, and Instrumentation Handbook. Chapter 4: Measurement Accuracy.* CRC Press, 02/26; 2015/07 1999.

[17] G. M. Hoffmann, H. Huang, S. L. Waslander, and C. J. Tomlin, "Quadrotor helicopter flight dynamics and control: Theory and experiment," in *Proc. of the AIAA Guidance, Navigation, and Control Conference*, vol. 2, 2007.

[18] M. K. Habib, *Handbook of Research on Advancements in Robotics and Mechatronics.* IGI Global, 2014.

[19] T. Sobh, *Prototyping of Robotic Systems: Applications of Design and Implementation: Applications of Design and Implementation.* IGI Global, 2012.

[20] A. Menache, *Understanding Motion Capture for Computer Animation*. Elsevier, 2011.

[21] (2016, 27 January) Labview system design software. National Instruments. [Online]. Available: http://www.ni.com/labview/

[22] J. M. O'Kane, *A Gentle Introduction to ROS*. Jason M. O'Kane, 2014.

[23] (2016, 27 January) Ros for labview by tufts university: A ros client api solution for labview. National Instruments and Tuft University. [Online]. Available: http://sine.ni.com/nips/cds/view/p/lang/en/nid/213279

[24] E. Fernández, L. S. Crespo, A. Mahtani, and A. Martinez, *Learning ROS for Robotics Programming*. Packt Publishing Ltd, 2015.

[25] (2016, 27 January) Ar drone toolkit for labview - lvh: Labview vis for controlling the parrot ar drone, version 0.1.0.36. Nathional Instruments. [Online]. Available: http://sine.ni.com/nips/cds/view/p/lang/en/nid/211837

[26] CHRobotics. (2015, 03 February) Understanding euler angles. [Online]. Available: http://www.chrobotics.com/library/understanding-euler-angles

[27] G. Ducard and R. D'Andrea, "Autonomous quadrotor flight using a vision system and accommodating frames misalignment," in *Industrial Embedded Systems, 2009. SIES '09. IEEE International Symposium on*, 2009, pp. 261–264, iD: 1.

[28] L. Christian. Distributed timebase (dtb) example. National Instruments. [Online]. Available: https://decibel.ni.com/content/docs/DOC-44633

[29] (2015, 30 October) Introduction to distributed clock synchronization and the ieee 1588 precision time protocol. National Instruments. [Online]. Available: http://www.ni.com/tutorial/2822/en/

REPORT DOCUMENTATION PAGE

Form Approved
OMB No. 0704–0188

1. REPORT DATE *(DD–MM–YYYY)*	2. REPORT TYPE	3. DATES COVERED *(From — To)*
03–24–2016	Master's Thesis	Sept 2014 — Mar 2016

4. TITLE AND SUBTITLE

Utilization of a Geodesic Sphere and Quadcopter as Two-Way Field Probe for Electro-Magnetic Field Measurements in an Indoor Radar Cross Section Range

5a. CONTRACT NUMBER

5b. GRANT NUMBER

5c. PROGRAM ELEMENT NUMBER

6. AUTHOR(S)

Lett, Nathan, Capt, USAF

5d. PROJECT NUMBER

5e. TASK NUMBER

16G115

5f. WORK UNIT NUMBER

7. PERFORMING ORGANIZATION NAME(S) AND ADDRESS(ES)

Air Force Institute of Technology
Graduate School of Engineering and Management (AFIT/EN)
2950 Hobson Way
WPAFB OH 45433-7765

8. PERFORMING ORGANIZATION REPORT NUMBER

AFIT-ENG-MS-16-M-031

9. SPONSORING / MONITORING AGENCY NAME(S) AND ADDRESS(ES)

Mr. Timothy Conn, Chief Scientist
96th Test Group/National RCS Test Facility
WSMR Range Road 10, Bldg 7000
Holloman AFB, NM 88002
DSN 349-3324,
Email: timothy.conn.ctr@us.af.mil

10. SPONSOR/MONITOR'S ACRONYM(S)

NRTF

11. SPONSOR/MONITOR'S REPORT NUMBER(S)

12. DISTRIBUTION / AVAILABILITY STATEMENT

DISTRIBUTION STATEMENT A:
APPROVED FOR PUBLIC RELEASE; DISTRIBUTION UNLIMITED.

13. SUPPLEMENTARY NOTES

14. ABSTRACT

This thesis intends to provide a unique two-way field probe solution for measuring electromagnetic fluctuations in a test volume. In this thesis, the design, development, and demonstration of a geodesic sphere encased quadcopter two-way probe is explained. The Parrot® Bebop Drone quadcopter was used with a 2ν frequency divided geodesic sphere design. Position and pose data was accomplished with a Vicon™ motion capture system. A Lintek 4000 radar instrumentation system provided RCS measurements. RCS measurements with position and pose data synchronization is critical. Sample points captured must be sufficient to extract any conclusions. This research concluded that a geodesic sphere and quadcopter could be used as a two-way probe to measure general field characteristics of an indoor compact RCS range. In a quadcopter only flight test, using a 2 to 5 GHz frequency sweep at 0.1 GHz increments, there were three instances where a direct correlation in phase measurement to flight path was observed.

15. SUBJECT TERMS

Radar Cross Section (RCS), Two-way probe, Quadcopter, Geodesic Sphere, pose, Robot Operating System (ROS)

16. SECURITY CLASSIFICATION OF:			17. LIMITATION OF ABSTRACT	18. NUMBER OF PAGES	19a. NAME OF RESPONSIBLE PERSON
a. REPORT	b. ABSTRACT	c. THIS PAGE			Dr. Peter J. Collins, AFIT/ENG
U	U	U	UU	114	19b. TELEPHONE NUMBER *(include area code)* (937) 255-3636, x7256; peter.collins@afit.edu